Remotely evaluating the seasonality of gross primary production at high latitudes

Thesis by
Rui Cheng

In Partial Fulfillment of the Requirements for the
Degree of
Doctor of Philosophy

CALIFORNIA INSTITUTE OF TECHNOLOGY
Pasadena, California

2023
Defended August 10, 2022

Rui Cheng
ORCID: 0000-0002-3003-8339

To my parents
for raising me as an assertive explorer

ACKNOWLEDGEMENTS

First and foremost, I would like to thank my PhD advisor Christian Frankenberg. Christian has always been a supportive and resourceful advisor. Through his mentoring, I have been becoming a critical thinker and a scientist with curiosity. His encouragement and positive attitude led me through the hardships of doing science and will continue to inspire my academic career.

I acknowledge three additional members of my thesis advisory committee: Tapio Schneider, Paul Wennberg, and Anthony Bloom. Tapio and Paul have been encouraging figures throughout my entire PhD program, from my qualifying exam to this thesis. Tapio advised my second qualifying project on climate science. With his help, I can still proudly say I am a meteorologist and hope to apply this skill in future projects. I cannot thank Paul enough for frequently checking in with me when Christian was away. I feel lucky to have Anthony, whose guidance in my career planning was beneficial and cheerful, on my committee. I am really grateful for this fantastic team who supported me through the hardship of the COVID pandemic. I could not finish my thesis without their thoughtful suggestions and creative ideas. I hope one day I can become a good mentor like them.

I have been fortunate to work with the following research mentors: Troy Magney, Philipp Köhler, Debsunder Dutta, and Lenka Novak. I appreciate their patience and generous guidance. They are always my role models in academia.

In the context of this thesis, I thank my collaborators, David Bowling, Peter Blanken, Marion Syndonia Bret-Harte, Sean Burns, Eugénie Euskirchen, Katja Grossman, Martin Jung, Hideki Kobayashi, Barry Logan, Sophia Lopez, Erica Orcutt, Zoe Pierra, Adrian Rocha, Oliver Sonnentag, Jochen Stutz, Sophia Walther, Andrew Richardson, and Donatella Zona. The work presented in this thesis was supported by NASA Grants ABoVE (award 80NSSC19M0129), OCO Science (award 80NSSC18K0895), and CMS (award 80NSSC20K0010).

I would like to especially thank the GPS division for the opportunities to go to the Arctic and Hawaii, which ultimately have been and will be my research topics. I have found a sense of belonging in this remarkable community thanks to the following colleagues and friends:

<u>GPS staff</u>: Nora Oshima, Julie Lee, Leilani Rivera-Dotson, Bronagh Glaser, Julia Zuckerman, Mark Garcia.

Faculty: Paul Asimow, Simona Bordoni, Clair Bucholz, Jörn Callies, Bethany Elmann, Woody Fischer, Joe Kirschvink, Jared Leadbetter, John Seinfeld, Andy Thompson, Alan Barr, Soon-Jo Chung, Pietro Perona, and Jakob van Zyl.

The Fall 2017 student cohorts: Aida Behmard, Harriet Brettle, Guannan Dong, Madison Douglas, Jackie Dowling, Erin Hightower, Benjamin Idini, Jiazheng, Li, Dustin Morris, William Palfey, Olivia Pardo, Daniela Rodriguez, Eva Scheller, Emma Sosa, Shreyas Vissapragada, Renee Wang, Ethan Williams, Chachan Yayaati, and Qicheng Zhang;

Frankenberg Lab: Newton Nguyen, Russell Doughty, Vincent Humphrey, Ke Liu, Linyin He, Siraput Jongaramrungruang, Rupesh Jeyaram, Yi Yin, Yujie Wang, Yitong Yao, Renato Braghiere, and Brendan Byrne.

Awesome friends: Katrina Hui, Jina Lee, Sujung Lim, Stacy Larochelle, Ollie Stephenson, Vasilije Dobrosavljevic, Preston Kemeny, Celeste Labedz, Maddie Lewis, Joe Biasi, Dan Johnson, Elizabeth Bailey, Leah Sabbeth, Austin Chadwick, Alistair Hayden, Kyle Metcalfe, Peter Martin, Sarah Crucilla, Karen Pham, Lee Saper, Jack Muir, Jorge Castellanos, Sarah Zeichner, Kevin Roback, Robert Cass, Reina Buenconsejo, Sophia Charan, Oliver Dunbar, Josh Laughner, Ho-hsuan Wei, Xiyue Zhang, Yanzhe Zhu, Zhaoyi Shen, Junjie Liu, Ignacio Lopez-Gomez, Jing Li, Xunyi Wu, Yuanlong Huang, Jia He, Voon hui Lai, Anna Jaruga, Daniel Huang, Alan Gu, Dave Bonan, Costa Christopoulos, Heng Dong, Lily Dove, Yongzhao Guo, Polina Khapikova, Sara Murphy, Harrison Parker, Shirui Peng, Clare Singer, Ryan Ward, Jiani Yang, Yi Zhang, Akshay Sridhar, Ariana Tribby, Dien Wu, Danica Adams, Makayla Betts, Ryleigh Davis, Ruolin Deng, Eran Funaro, Tobias Koehne, Ren Marquez, Yuan kai Liu, Pond Sirorattanakul, Carl Swindle, Noah Tashbook, Rebecca Wipfler, Manni He, Harsha Narravula, Daniel Yoder, Rebecca Gallivan, Miggy Chuapoco, Sina Booeshaghi, Isabel Peng, Forte Shinko, Aidan Fenwick, Mary Arrastia, Eric Liaw, Hanwei Liu, and many more!

I need to thank my friends I met in the US, including Kexin Chen, Xin Li, Xueyin Zhang, and Peng Gao, who always take care of me like family members.

Finally, I extremely appreciate my family for their support and unconditional love. Thank you, Mama, Baba, Laolao, Laoye, Jiujiu, Jiuma, and Xiaoyu, for always believing in me. I cannot wait to see you all in person soon.

ABSTRACT

A warming trend larger than the global average is changing high-latitude terrestrial ecosystems. The impact of climate change at high latitudes is especially notable on the seasonality of vegetation photosynthesis, such as the Arctic greening, lengthened growing season, and increased peak production in the growing season. As a critical component of the global carbon cycle and land carbon sink, continuously monitoring the seasonal trajectory of ecosystem-level photosynthesis, Gross Primary Production (GPP), is much needed to better understand the climate change impacts and the sensitivity of high-latitude plant communities under global climate change. GPP has been estimated from both ground and space. However, sparsely distributed ground-level measurements are not representative of heterogeneous land cover and complex terrain in high latitudes. Remote sensing techniques provide extensive spatial coverage for comparing GPP at the regional scale. In this thesis, I carefully examine the advances in remote sensing for monitoring GPP at high latitudes, including using hyperspectral reflectance and Solar-Induced chlorophyll Fluorescence (SIF). We show that reflectance near 531 nm can track the seasonality of Light Use Efficiency (LUE), complementing conventional normalized difference vegetation index which is only a proxy of Absorbed Photosynthetic Active Radiation (APAR). Tracking both LUE and APAR is critical for improving GPP estimation, especially in evergreen forests with photosynthetic phenology but sustained canopy color — a typical land cover type at high latitudes. Satellite-measured SIF can also track both LUE and APAR. Here, it is shown that the empirical model predicting GPP using SIF is land cover dependent. The presence of snow and surface, heterogeneous land cover, and complex terrains in the high latitudes further complicate the interpretation of the SIF-GPP relationship. To improve the accuracy of interpreting SIF in complex terrain, a geometric model is developed to account for variations in APAR on tilted slopes. The results of this thesis enhance the use of both reflectance and SIF to help improve terrestrial biosphere models simulating GPP and cope with model-data uncertainties. The results are also a useful reference for future satellite missions designing instruments and correcting topographic impacts. Overall, this thesis contributes to better evaluating GPP and constraining climate projection uncertainties.

PUBLISHED CONTENT AND CONTRIBUTIONS

R. Cheng, T. S. Magney, D. Dutta, D. R. Bowling, B. A. Logan, S. P. Burns, P. D. Blanken, K. Grossmann, S. Lopez, A. D. Richardson, J. Stutz, and C. Frankenberg. "Decomposing reflectance spectra to track gross primary production in a subalpine evergreen forest". In: *Biogeosciences* 17(18):4523-4544, 2022. DOI: 10.5194/bg-17-4523-2020.
R.C. conceived the study, performed the data analysis, and wrote the paper.

R. Cheng, T. S. Magney, E. L. Orcutt, Bowling D. R., M. S. Bret-Harte, E. S. Euskirchen, M. Jung, H. Kobayashi, P. Köhler, Z. Pierrat, A. V. Rocha, O. Sonnentag, S. Walther, D. Zona, and C. Frankenberg. "Evaluating photosynthetic activity across Arctic-Boreal land cover types using Solar-Induced chlorophyll Fluorescence" (under review). In: *Environmental Research Letters*.
R.C. conceived the study, performed the data analysis, and wrote the paper.

R. Cheng, P. Köhler, and C. Frankenberg. "Impact of radiation variations on temporal upscaling of instantaneous solar-induced chlorophyll fluorescence" (under re-review). In: *Agricultural and Forest Meteorology*.
R.C. conceived the study, performed the data analysis, and wrote the paper.

TABLE OF CONTENTS

LIST OF ILLUSTRATIONS

LIST OF TABLES

Chapter 1

INTRODUCTION

1.1 Motivation

Terrestrial ecosystems are a critical part of the global carbon cycle. Plant carbon uptake via photosynthesis, as the largest carbon sink for atmospheric CO_2 (Ciais et al., 2014), contributes to vegetation-climate feedback through carbon, water, and energy exchange between the land and atmosphere (Peñuelas and Filella, 2009; Richardson et al., 2013). However, an amplified warming trend and more frequent warming events have occurred at high latitudes (Field, 2014; Ford et al., 2015; Post et al., 2019; Stocker et al., 2013; Walsh and Brettschneider, 2019), threatening current high-latitude plant communities (Box et al., 2019; Ernakovich et al., 2014). The impact of climate change at high latitudes is especially notable in the seasonality of vegetation photosynthesis, such as the Arctic greening (Berner et al., 2020), lengthened growing season (Park et al., 2016), and increased peak production in the growing season (Elmendorf et al., 2012). These changes create high uncertainties in the projection of the sign and magnitude of the land carbon sink (Loisel et al., 2021; McGuire et al., 2009; Zona et al., 2022). To better understand climate change impacts on plant communities, continuously monitoring the seasonal trajectory of ecosystem-level photosynthesis, Gross Primary Production (GPP) is much needed. While net carbon fluxes, i.e. Net Ecosystem Exchange (NEE), are ultimately governing atmospheric CO_2 abundances, my thesis will focus on the engine of biogeochemical cycles here, i.e. the uptake through photosynthesis. In the future, the thawing of permafrost could lead to the release of additional CO_2, which could counteract some of the arctic greening that we observe.

1.2 Overview of conventional GPP measurements

GPP has been estimated from both ground and space. On the ground, Eddy Covariance (EC) techniques can derive GPP from directly measured net land-atmosphere CO_2 flux at the ecosystem level (Pastorello et al., 2020). There are hundreds of flux towers around the world measuring GPP (Falge et al., 2017). Yet the EC towers at high latitudes are often sparsely located in easily accessible regions. Hence, a large portion of high latitudes has no GPP measurement. In addition, the temporal coverage of EC towers differs among towers. Therefore, GPP derived from EC towers is often inadequate to be representative at regional scales at high latitudes (Pallandt et al., 2022).

Remote sensing techniques enable global and almost continuous monitoring of GPP from space. The extensive spatial coverage and consistent time range allow for comparisons of GPP across heterogeneous land cover types (Funk et al., 2004) and complex terrain (Roland et al., 2019) in the high latitudes where EC towers have limited access. Although the temporal resolution of satellite products is often coarser than ground-based measurements, it is sufficient for extracting the seasonality of GPP.

Remotely sensed GPP is indirectly inferred from proxies of the plant photochemical processes. The simplest model for inferring GPP in remote sensing is as follows:

$$GPP = fPAR \times PAR \times LUE. \tag{1.1}$$

Here, PAR is the photosynthetically active radiation, and fPAR is the fraction of PAR absorbed by a canopy. Thus, Absorbed PAR (APAR) = fPAR×PAR. APAR is mostly partitioned between photosynthesis (Photochemical Quenching, PQ) and heat dissipation (Non-Photochemical Quenching, NPQ) (Björkman and Demmig-Adams, 1995; Schreiber et al., 1986). LUE describes the effective daily photosynthetic efficiency of APAR (Monteith, 1972; Monteith and Moss, 1977).

Conventional remote sensing tools are proxies of APAR, such as the Normalized Difference Vegetation Index (NDVI; Tucker 1979), kernel-based NDVI (kNDVI; Camps-Valls et al. 2021), and Near-Infrared Reflectance of Vegetation (NIRv; Badgley et al. 2017), which essentially calculate the difference in reflectance between red and far-red bands, also known as the red edge. The red edge is sensitive to the green leaf area and the total amount of chlorophyll in the canopy within the field of view (Goward et al., 1985; Justice et al., 1985; Tucker et al., 1985). However, the greenness of a canopy only represents the potential GPP without constraining LUE. The GPP products solely using conventional VIs needs to parameterize LUE from empirical relationships of LUE and meteorological conditions (Krinner et al., 2005; Running et al., 2004). Inevitably, the LUE model limits the accuracy of the derived GPP. This drawback is especially problematic in evergreen forests, a main land cover type at high latitudes, with seasonally changing photosynthetic efficiencies but sustained canopy color.

1.3 Advances in remote sensing techniques

Advances in remote sensing techniques have shown promise to track LUE in addition to APAR, such as evaluating NPQ and Solar-Induced chlorophyll Fluorescence (SIF).

Evaluating NPQ

The Photochemical Reflectance Index (PRI) and Chlorophyll/carotenoid Index (CCI) represent a genre of vegetation Indices (VIs) that can provide information on NPQ. PRI and CCI highlight the spectral regions sensitive to dynamic changes in leaf/needle photoprotective pigment composition (Gamon et al., 2016, 1997), showing promise for tracking seasonal changes in photosynthesis of evergreen forests (Adams and Demmig-Adams, 1994; Björkman and Demmig-Adams, 1995). However, these have mainly been investigated with intermittent field campaigns (Hall et al., 2008; Hilker et al., 2011) or with narrow-band spectrometers in these ecosystems (Gamon et al., 2016; Huemmrich et al., 2019). The evaluation of pigment-driven spectral changes in evergreen forests over the course of a season is necessary to determine where, when, and why certain wavelength regions could advance our mechanistic understanding of canopy photosynthetic and photoprotective pigments. However, using continuously measured canopy hyperspectral reflectance and in situ pigment samples has not been done with both empirical and process-based methods.

Evaluating SIF

SIF is another approach to infer GPP from space, which is defined by a small amount of photons (650-850 nm) re-emitted from chlorophyll at longer wavelength during the process of light harvesting in photosynthesis (Genty et al., 1989; Krause and Weis, 1991). Because spaceborne SIF is not only a proxy for APAR in deciduous canopies (Dechant et al., 2020), it also partially tracks the partitioning of APAR between PQ and NPQ, i.e. LUE (Magney et al., 2019). Magney et al. (2020) reviewed that satellite measured SIF linearly correlated with GPP in multiple biomes. These benefits make satellite-measured SIF a useful tool for estimating GPP on a large scale with various land cover types.

As more satellites measuring SIF globally have been launched in recent years (such as TROPOMI Köhler et al. (2018) and OCO-2 Frankenberg et al. (2014); Sun et al. (2017)), the regions of interest using SIF to infer GPP are expanding to higher latitudes in recent studies (Jeong et al., 2017; Luus et al., 2017; Walther et al., 2016, 2018). Turner et al. (2021) and Liu et al. (2022) reported the scale factor of SIF-GPP relationships as a function of land cover. However, the resulting scale factor from previous studies in lower latitudes (Liu et al., 2022; Turner et al., 2021) cannot represent the heterogeneous land cover with unique vegetation composition at high latitudes (Bliss et al., 1992). The studies at high latitudes are either limited to the area with EC towers for validation purposes (Luus et al., 2017) or focus only on very few land cover types at high latitudes Luus et al. (2017); Walther et al. (2016). Due to these limitations, the SIF-GPP relationship across land cover types at high latitudes is not well understood.

Another limitation of SIF is that the satellite measured SIF is an instantaneous value driven by PAR at the overpass time. For studies focusing on seasonal variations, the SIF measurement needs to be corrected to the daily averaged value. The current correction strategy assumes the surface is flat so that the Solar Zenith Angle (SZA) is sufficient to approximate the solar irradiance (Köhler et al., 2018). However, this assumption breaks down in complex terrains because the solar irradiance depends on the angle between the direction of the Sun and the surface normal (Solar Incidence Angle, SIA), which does not equal SZA. The simple SZA strategy also assumes an ideal clear-sky condition, ignoring weather that changes the actual PAR. On a large scale, the impact of topography and weather on solar irradiance is non-negligible.

1.4 Thesis outline

My thesis focuses on evaluating remote sensing advances in tracking the seasonality of GPP at high latitudes, including mechanistically explaining hyperspectral reflectance tracking LUE (Chapter 2), assessing the SIF-GPP relationship across high-latitude land cover types (Chapter 3), and the topographic correction on SIF (Chapter 4).

In Chapter 2 (Cheng et al., 2020), we focused on tracking LUE seasonality using spectrally resolved reflectance. We continuously measured daily-averaged vegetation reflectance (400–900 nm) using a canopy spectrometer system, PhotoSpec (Grossmann et al., 2018), mounted on top of an eddy-covariance flux tower in a subalpine evergreen forest at Niwot Ridge, Colorado, USA. We analyzed driving spectral components in the measured canopy reflectance using both statistical and process-based approaches. The decomposed spectral components around 531 nm co-varied with needle-scale carotenoid content, chlorophyll to carotenoid ratios, and GPP (Figure 2.7), supporting the interpretation of the PRI and CCI, while little seasonal variation in both NDVI and NIRv in this ecosystem. Reconstructing GPP from vegetation reflectance using Partial Least Squares Regression (PLSR) explained approximately 87% of the variability in observed GPP. Our results link the seasonal variation of reflectance to the pool size of photoprotective pigments, highlighting all spectral locations within 400–900 nm associated with LUE seasonality in evergreen forests.

In Chapter 3, we made breakthroughs in evaluating the SIF-GPP relationship with extensive spatial coverage across heterogeneous high-latitude land cover types with unique vegetation compositions. We evaluated the correlation and the goodness of the fit between TROPOMI SIF (Köhler et al., 2018) and Fluxcom GPP, a state-of-the-art GPP product upscaled from EC GPP and remotely sensed surface conditions (Jung et al., 2020; Tramontana et al., 2016). We found a large variance in the scale factor between SIF and GPP within the Arctic-Boreal region. Meanwhile, we found the following uncertainties in the resulting SIF-GPP relationship: 1) high bias in reflectance-based GPP products due to snow and water, 2) topographic dependence of the SIF-GPP relationship, and 3) heterogeneous sub-pixel land cover compositions across spatial scales. Taken together, our reported scale factor, statistic metrics (Pearson's r^2 and reduced χ^2), and uncertainty evaluations can help improve terrestrial biosphere models and cope with model-data uncertainties.

In Chapter 4, we reduce uncertainties in satellite-measured SIF due to weather and topography. To account for the weather impact, we compared the length-of-day correction using the idealized diurnal PAR cycle, i.e. SZA, versus the actual diurnal PAR cycle. We found that the original approach using SZA is a reliable approximation for flat surfaces under a clear sky. At longer time-scales, a sampling (clear sky) bias might exist due to cloud-filtering of satellite data. In the Amazon, the true monthly mean PAR can be 25% lower than the one for cloud-filtered days, potentially inducing seasonal SIF biases on the same order. To account for the topographic impact, we proposed a new length-of-day correction factor with a geometric correction on direct PAR with SIA to replace the original correcting strategy (Köhler et al., 2018) using SZA. In the San Gabriel Mountains, California, USA, the modified DC is changed by as much as 500% for strongly tilted surfaces. This modification is especially important for satellite instruments with fine spatial resolutions, where surface slopes are not averaged out and can have a substantial impact on reflectance and SIF. Overall, our refined length-of-day correction factor and averaging strategy can help both satellite SIF and vegetation indices interpretation. In addition, it will facilitate intercomparisons over a wide range of spatio-temporal scales and overpass times.

In summary, my thesis showcases the ability to track the seasonality of GPP from the ground level to regional scales at high latitudes using advanced remote sensing tools. My results not only mechanistically explain these tools but also provide references for future satellite missions for better evaluating GPP by selecting spectral bands, correcting topographic parameters, and coping with model-data uncertainties. Although not all study regions in my thesis are from high latitudes, they were chosen to be best suitable for addressing the scientific question in each project. Thus, the methodology and results of these projects are applicable to global-scale studies. Overall, my thesis will help better constrain the uncertainties of global GPP estimation and the global carbon cycle.

Bibliography

W. Adams and B. Demmig-Adams. Carotenoid composition and down regulation of photosystem II in three conifer species during the winter. *Physiologia Plantarum*, 92(3):451–458, November 1994. ISSN 0031-9317. doi: 10.1111/j.1399-3054.1994.tb08835.x. URL `http://doi.wiley.com/10.1111/j.1399-3054.1994.tb08835.x`. Publisher: John Wiley & Sons, Ltd (10.1111).

G. Badgley, C. B. Field, and J. A. Berry. Canopy near-infrared reflectance and terrestrial photosynthesis. *Science Advances*, 3(3):e1602244, 2017. Publisher: American Association for the Advancement of Science.

L. T. Berner, R. Massey, P. Jantz, B. C. Forbes, M. Macias-Fauria, I. Myers-Smith, T. Kumpula, G. Gauthier, L. Andreu-Hayles, B. V. Gaglioti, and others. Summer warming explains widespread but not uniform greening in the Arctic tundra biome. *Nature communications*, 11(1):1–12, 2020. Publisher: Nature Publishing Group.

O. Björkman and B. Demmig-Adams. Regulation of photosynthetic light energy capture, conversion, and dissipation in leaves of higher plants. In *Ecophysiology of photosynthesis*, pages 17–47. Springer, 1995.

L. C. Bliss, N. V. Matveyeva, and others. Circumpolar arctic vegetation. *Arctic ecosystems in a changing climate: an ecophysiological perspective*, pages 59–89, 1992. Publisher: Academic Press San Diego.

J. E. Box, W. T. Colgan, T. R. Christensen, N. M. Schmidt, M. Lund, F.-J. W. Parmentier, R. Brown, U. S. Bhatt, E. S. Euskirchen, V. E. Romanovsky, and others. Key indicators of Arctic climate change: 1971–2017. *Environmental Research Letters*, 14(4):045010, 2019. Publisher: IOP Publishing.

G. Camps-Valls, M. Campos-Taberner, A. Moreno-Martinez, S. Walther, G. Duveiller, A. Cescatti, M. D. Mahecha, J. Muñoz-Marí, F. J. García-Haro, L. Guanter, M. Jung, J. A. Gamon, M. Reichstein, and S. W. Running. A unified vegetation index for quantifying the terrestrial biosphere. *Science Advances*, 7(9):eabc7447, February 2021. ISSN 2375-2548. doi: 10.1126/sciadv.abc7447. URL `https://advances.sciencemag.org/lookup/doi/10.1126/sciadv.abc7447`.

R. Cheng, T. S. Magney, D. Dutta, D. R. Bowling, B. A. Logan, S. P. Burns, P. D. Blanken, K. Grossmann, S. Lopez, A. D. Richardson, and others. Decomposing reflectance spectra to track gross primary production in a subalpine evergreen forest. *Biogeosciences*, 17(18):4523–4544, 2020. Publisher: Copernicus GmbH.

P. Ciais, C. Sabine, G. Bala, L. Bopp, V. Brovkin, J. Canadell, A. Chhabra, R. DeFries, J. Galloway, M. Heimann, and others. *Carbon and other biogeochemical cycles*. Cambridge University Press, 2014. Publication Title: Climate change 2013: the physical science basis. Contribution of Working Group I to the Fifth Assessment Report of the Intergovernmental Panel on Climate Change.

B. Dechant, Y. Ryu, G. Badgley, Y. Zeng, J. A. Berry, Y. Zhang, Y. Goulas, Z. Li, Q. Zhang, M. Kang, and others. Canopy structure explains the relationship between photosynthesis and sun-induced chlorophyll fluorescence in crops. *Remote Sensing of Environment*, 241:111733, 2020. Publisher: Elsevier.

S. C. Elmendorf, G. H. R. Henry, R. D. Hollister, R. G. Björk, N. Boulanger-Lapointe, E. J. Cooper, J. H. C. Cornelissen, T. A. Day, E. Dorrepaal, T. G. Elumeeva, and others. Plot-scale evidence of tundra vegetation change and links to recent summer warming. *Nature Climate Change*, 2(6):453–457, 2012. Publisher: Nature Publishing Group.

J. G. Ernakovich, K. A. Hopping, A. B. Berdanier, R. T. Simpson, E. J. Kachergis, H. Steltzer, and M. D. Wallenstein. Predicted responses of arctic and alpine ecosystems to altered seasonality under climate change. *Global Change Biology*, 20(10):3256–3269, 2014. Publisher: Wiley Online Library.

E. Falge, M. Aubinet, P. S. Bakwin, D. Baldocchi, P. Berbigier, C. Bernhofer, T. A. Black, R. Ceulemans, K. J. Davis, A. J. Dolman, and others. FLUXNET research network site characteristics, investigators, and bibliography, 2016. *ORNL DAAC*, 2017.

C. B. Field. *Climate change 2014–Impacts, adaptation and vulnerability: Regional aspects*. Cambridge University Press, 2014.

J. D. Ford, G. McDowell, and T. Pearce. The adaptation challenge in the Arctic. *Nature Climate Change*, 5(12):1046–1053, 2015. Publisher: Nature Publishing Group.

C. Frankenberg, C. O'Dell, J. Berry, L. Guanter, J. Joiner, P. Köhler, R. Pollock, and T. E. Taylor. Prospects for chlorophyll fluorescence remote sensing from the Orbiting Carbon Observatory-2. *Remote Sensing of Environment*, 147:1–12, 2014. Publisher: Elsevier.

D. W. Funk, L. E. Noel, and A. H Freedman. Environmental gradients, plant distribution, and species richness in arctic salt marsh near Prudhoe Bay, Alaska. *Wetlands Ecology and Management*, 12(3):215–233, June 2004. ISSN 0923-4861. doi: 10.1023/B:WETL.0000034074.81373.65. URL http://link.springer.com/10.1023/B:WETL.0000034074.81373.65.

J. Gamon, K. F. Huemmrich, C. Y. S. Wong, I. Ensminger, S. Garrity, D. Y. Hollinger, A. Noormets, and J. Peñuelas. A remotely sensed pigment index reveals photosynthetic phenology in evergreen conifers. *Proceedings of the National Academy of Sciences*, 113(46):13087–13092, 2016. Publisher: National Acad Sciences.

J. A. Gamon, L. Serrano, and J. S. Surfus. The photochemical reflectance index: an optical indicator of photosynthetic radiation use efficiency across species, functional types, and nutrient levels. *Oecologia*, 112(4):492–501, November 1997. ISSN 1432-1939. doi: 10.1007/s004420050337. URL https://doi.org/10.1007/s004420050337.

B. Genty, J.-M. Briantais, and N. R. Baker. The relationship between the quantum yield of photosynthetic electron transport and quenching of chlorophyll fluorescence. *Biochimica et Biophysica Acta (BBA)-General Subjects*, 990(1):87–92, 1989. Publisher: Elsevier.

S. Goward, C. J. Tucker, and D. G. Dye. North American vegetation patterns observed with the NOAA-7 advanced very high resolution radiometer. *Vegetatio*, 64(1):3–14, 1985. Publisher: Springer.

K. Grossmann, C. Frankenberg, T. S. Magney, S. C. Hurlock, U. Seibt, and J. Stutz. PhotoSpec: A new instrument to measure spatially distributed red and far-red Solar-Induced Chlorophyll Fluorescence. *Remote Sensing of Environment*, 216:311–327, October 2018. ISSN 0034-4257. doi: 10.1016/j.rse.2018.07.002. URL http://www.sciencedirect.com/science/article/pii/S0034425718303298.

F. G. Hall, T. Hilker, N. C. Coops, A. Lyapustin, K. F. Huemmrich, E. Middleton, H. Margolis, G. Drolet, and T. A. Black. Multi-angle remote sensing of forest light use efficiency by observing PRI variation with canopy shadow fraction. *Remote Sensing of Environment*, 112(7):3201–3211, 2008. Publisher: Elsevier.

T. Hilker, N. C. Coops, F. G. Hall, C. J. Nichol, A. Lyapustin, T. A. Black, M. A. Wulder, R. Leuning, A. Barr, D. Y. Hollinger, and others. Inferring terrestrial photosynthetic light use efficiency of temperate ecosystems from space. *Journal of Geophysical Research: Biogeosciences*, 116(G3), 2011. Publisher: Wiley Online Library.

K. F. Huemmrich, P. Campbell, D. Landis, and E. Middleton. Developing a common globally applicable method for optical remote sensing of ecosystem light use efficiency. *Remote Sensing of Environment*, 230:111190, 2019. Publisher: Elsevier.

S. Jeong, D. Schimel, C. Frankenberg, D. T. Drewry, J. B. Fisher, M. Verma, J. A. Berry, J.-E. Lee, and J. Joiner. Application of satellite solar-induced chlorophyll fluorescence to understanding large-scale variations in vegetation phenology and function over northern high latitude forests. *Remote sensing of Environment*, 190: 178–187, 2017. Publisher: Elsevier.

M. Jung, C. Schwalm, M. Migliavacca, S. Walther, G. Camps-Valls, S. Koirala, P. Anthoni, S. Besnard, P. Bodesheim, N. Carvalhais, and others. Scaling carbon fluxes from eddy covariance sites to globe: synthesis and evaluation of the FLUXCOM approach. *Biogeosciences*, 17(5):1343–1365, 2020. Publisher: Copernicus GmbH on behalf of the European Geosciences Union.

C. Justice, J. R. G. Townshend, B. N. Holben, and et C. J. Tucker. Analysis of the phenology of global vegetation using meteorological satellite data. *International Journal of Remote Sensing*, 6(8):1271–1318, 1985. Publisher: Taylor & Francis.

G. H. Krause and E. Weis. Chlorophyll fluorescence and photosynthesis: the basics. *Annual review of plant biology*, 42(1):313–349, 1991. Publisher: Annual Reviews 4139 El Camino Way, PO Box 10139, Palo Alto, CA 94303-0139, USA.

G. Krinner, N. Viovy, N. de Noblet-Ducoudré, J. Ogée, J. Polcher, P. Friedlingstein, P. Ciais, S. Sitch, and I. C. Prentice. A dynamic global vegetation model for studies of the coupled atmosphere-biosphere system. *Global Biogeochemical Cycles*, 19(1), 2005. Publisher: Wiley Online Library.

P. Köhler, C. Frankenberg, T. S. Magney, L. Guanter, J. Joiner, and J. Landgraf. Global Retrievals of Solar-Induced Chlorophyll Fluorescence With TROPOMI: First Results and Intersensor Comparison to OCO-2. *Geophysical Research Letters*, 45(19):10,456–10,463, October 2018. ISSN 0094-8276, 1944-8007. doi: 10.1029/2018GL079031. URL `https://onlinelibrary.wiley.com/doi/abs/10.1029/2018GL079031`.

Y. Liu, J. M. Chen, L. He, Z. Zhang, R. Wang, C. Rogers, W. Fan, G. de Oliveira, and X. Xie. Non-linearity between gross primary productivity and far-red solar-induced chlorophyll fluorescence emitted from canopies of major biomes. *Remote Sensing of Environment*, 271:112896, March 2022. ISSN 00344257. doi: 10.1016/j.rse.2022.112896. URL `https://linkinghub.elsevier.com/retrieve/pii/S0034425722000104`.

J. Loisel, A. V. Gallego-Sala, M. J. Amesbury, G. Magnan, G. Anshari, D. W. Beilman, J. C. Benavides, J. Blewett, P. Camill, D. J. Charman, S. Chawchai, A. Hedgpeth, T. Kleinen, A. Korhola, D. Large, C. A. Mansilla, J. Müller, S. van Bellen, J. B. West, Z. Yu, J. L. Bubier, M. Garneau, T. Moore, A. B. K. Sannel, S. Page, M. Väliranta, M. Bechtold, V. Brovkin, L. E. S. Cole, J. P. Chanton, T. R. Christensen, M. A. Davies, F. De Vleeschouwer, S. A. Finkelstein, S. Frolking,

M. Gałka, L. Gandois, N. Girkin, L. I. Harris, A. Heinemeyer, A. M. Hoyt, M. C. Jones, F. Joos, S. Juutinen, K. Kaiser, T. Lacourse, M. Lamentowicz, T. Larmola, J. Leifeld, A. Lohila, A. M. Milner, K. Minkkinen, P. Moss, B. D. A. Naafs, J. Nichols, J. O'Donnell, R. Payne, M. Philben, S. Piilo, A. Quillet, A. S. Ratnayake, T. P. Roland, S. Sjögersten, O. Sonnentag, G. T. Swindles, W. Swinnen, J. Talbot, C. Treat, A. C. Valach, and J. Wu. Expert assessment of future vulnerability of the global peatland carbon sink. *Nature Climate Change*, 11 (1):70–77, January 2021. ISSN 1758-6798. doi: 10.1038/s41558-020-00944-0. URL `https://www.nature.com/articles/s41558-020-00944-0`.

K. A. Luus, R. Commane, N. C. Parazoo, J. Benmergui, E. S. Euskirchen, C. Frankenberg, J. Joiner, J. Lindaas, C. E. Miller, W. C. Oechel, and others. Tundra photosynthesis captured by satellite-observed solar-induced chlorophyll fluorescence. *Geophysical Research Letters*, 44(3):1564–1573, 2017. Publisher: Wiley Online Library.

T. S. Magney, D. R. Bowling, B. A. Logan, K. Grossmann, J. Stutz, P. D. Blanken, S. P. Burns, R. Cheng, M. A. Garcia, P. Khler, and others. Mechanistic evidence for tracking the seasonality of photosynthesis with solar-induced fluorescence. *Proceedings of the National Academy of Sciences*, 116(24):11640–11645, 2019. Publisher: National Acad Sciences.

T. S. Magney, M. L. Barnes, and X. Yang. On the covariation of chlorophyll fluorescence and photosynthesis across scales. *Geophysical Research Letters*, 47 (23):e2020GL091098, 2020. Publisher: Wiley Online Library.

A. D. McGuire, L. G. Anderson, T. R. Christensen, S. Dallimore, L. Guo, D. J. Hayes, M. Heimann, T. D. Lorenson, R. W. Macdonald, and N. Roulet. Sensitivity of the carbon cycle in the Arctic to climate change. *Ecological Monographs*, 79 (4):523–555, November 2009. ISSN 0012-9615. doi: 10.1890/08-2025.1. URL `http://doi.wiley.com/10.1890/08-2025.1`.

J. L. Monteith. Solar Radiation and Productivity in Tropical Ecosystems. *Journal of Applied Ecology*, 9(3):747–766, 1972. URL `https://www.jstor.org/stable/2401901`.

J. L. Monteith and C. J. Moss. Climate and the Efficiency of Crop Production in Britain and Discussion. *Philosophical Transactions of the Royal Society B Biological Sciences*, 281(980):277–294, 1977.

M. T. A. Pallandt, J. Kumar, M. Mauritz, E. A. G. Schuur, A.-M. Virkkala, G. Celis, F. M. Hoffman, and M. Göckede. Representativeness assessment of the pan-Arctic eddy covariance site network and optimized future enhancements. *Biogeosciences*, 19(3):559–583, February 2022. ISSN 1726-4189. doi: 10.5194/bg-19-559-2022. URL `https://bg.copernicus.org/articles/19/559/2022/`.

T. Park, S. Ganguly, H. Tømmervik, E. S. Euskirchen, K.-A. Høgda, S. R. Karlsen, V. Brovkin, R. R. Nemani, and R. B. Myneni. Changes in growing season duration and productivity of northern vegetation inferred from long-term remote sensing data. *Environmental Research Letters*, 11(8):084001, 2016. Publisher: IOP Publishing.

G. Pastorello, C. Trotta, E. Canfora, H. Chu, D. Christianson, Y.-W. Cheah, C. Poindexter, J. Chen, A. Elbashandy, M. Humphrey, and others. The FLUXNET2015 dataset and the ONEFlux processing pipeline for eddy covariance data. *Scientific data*, 7(1):1–27, 2020. Publisher: Nature Publishing Group.

J. Peñuelas and I. Filella. Phenology feedbacks on climate change. *Science*, 324 (5929):887–888, 2009. Publisher: American Association for the Advancement of Science.

E. Post, R. B. Alley, T. R. Christensen, M. Macias-Fauria, B. C. Forbes, M. N. Gooseff, A. Iler, J. T. Kerby, K. L. Laidre, M. E. Mann, J. Olofsson, J. C. Stroeve, F. Ulmer, R. A. Virginia, and M. Wang. The polar regions in a 2°C warmer world. *Science Advances*, 5(12):eaaw9883, December 2019. ISSN 2375-2548. doi: 10.1126/sciadv.aaw9883. URL `https://www.science.org/doi/10.1126/sciadv.aaw9883`.

A. D. Richardson, T. F. Keenan, M. Migliavacca, Y. Ryu, O. Sonnentag, and M. Toomey. Climate change, phenology, and phenological control of vegetation feedbacks to the climate system. *Agricultural and Forest Meteorology*, 169: 156–173, 2013. Publisher: Elsevier.

C. A. Roland, J. H. Schmidt, S .G. Winder, S. E. Stehn, and E. F. Nicklen. Regional variation in interior Alaskan boreal forests is driven by fire disturbance, topography, and climate. *Ecological Monographs*, 89(3), August 2019. ISSN 0012-9615, 1557-7015. doi: 10.1002/ecm.1369. URL `https://onlinelibrary.wiley.com/doi/10.1002/ecm.1369`.

S. W. Running, R. R. Nemani, F. A. Heinsch, M. Zhao, M. Reeves, and H. Hashimoto. A continuous satellite-derived measure of global terrestrial primary production. *Bioscience*, 54(6):547–560, 2004. Publisher: American Institute of Biological Sciences.

U. Schreiber, U. Schliwa, and W. Bilger. Continuous recording of photochemical and non-photochemical chlorophyll fluorescence quenching with a new type of modulation fluorometer. *Photosynthesis research*, 10(1-2):51–62, 1986. Publisher: Springer.

T. F. Stocker, D. Qin, G.-K. Plattner, M. Tignor, S. K. Allen, J. Boschung, A. Nauels, Y. Xia, V. Bex, P. M Midgley, and others. Climate Change 2013. The Physical Science Basis. Working Group I Contribution to the Fifth Assessment Report of the Intergovernmental Panel on Climate Change-Abstract for decision-makers; Changements climatiques 2013. Les elements scientifiques. Contribution du groupe de travail I au cinquieme rapport d'evaluation du groupe d'experts intergouvernemental sur l'evolution du CLIMAT-Resume a l'intention des decideurs. 2013.

Y. Sun, C. Frankenberg, J. D. Wood, D. S. Schimel, M. Jung, L. Guanter, D. T. Drewry, M. Verma, A. Porcar-Castell, T. J. Griffis, and others. OCO-2 advances photosynthesis observation from space via solar-induced chlorophyll fluorescence. *Science*, 358(6360), 2017. Publisher: American Association for the Advancement of Science.

G. Tramontana, M. Jung, C. R. Schwalm, K. Ichii, G. Camps-Valls, B. Ráduly, M. Reichstein, M. A. Arain, A. Cescatti, G. Kiely, L. Merbold, P. Serrano-Ortiz, S. Sickert, S. Wolf, and D. Papale. Predicting carbon dioxide and energy fluxes across global FLUXNET sites with regression algorithms. *Biogeosciences*, 13 (14):4291–4313, July 2016. ISSN 1726-4189. doi: 10.5194/bg-13-4291-2016. URL `https://bg.copernicus.org/articles/13/4291/2016/`.

C. J. Tucker. Red and photographic infrared linear combinations for monitoring vegetation. *Remote sensing of Environment*, 8(2):127–150, 1979. Publisher: Elsevier.

C. J. Tucker, J. R. G. Townshend, and Thomas E Goff. African land-cover classification using satellite data. *Science*, 227(4685):369–375, 1985. Publisher: American Association for the Advancement of Science.

A. J. Turner, P. Köhler, T. S. Magney, C. Frankenberg, I. Fung, and R. C. Cohen. Extreme events driving year-to-year differences in gross primary productivity across the US. *Biogeosciences*, 18(24):6579–6588, December 2021. ISSN 1726-4189. doi: 10.5194/bg-18-6579-2021. URL `https://bg.copernicus.org/articles/18/6579/2021/`.

J. E. Walsh and B. Brettschneider. Attribution of recent warming in Alaska. *Polar Science*, 21:101–109, September 2019. ISSN 18739652. doi: 10.1016/j.polar.2018.09.002. URL `https://linkinghub.elsevier.com/retrieve/pii/S1873965218300872`.

S. Walther, M. Voigt, T. Thum, A. Gonsamo, Y Zhang, P. Köhler, M. Jung, A. Varlagin, and Luis Guanter. Satellite chlorophyll fluorescence measurements reveal large-scale decoupling of photosynthesis and greenness dynamics in boreal evergreen forests. *Global Change Biology*, 22(9):2979–2996, September 2016. ISSN 13541013. doi: 10.1111/gcb.13200. URL `https://onlinelibrary.wiley.com/doi/10.1111/gcb.13200`.

S. Walther, L. Guanter, B. Heim, M. Jung, G. Duveiller, A. Wolanin, and T. Sachs. Assessing the dynamics of vegetation productivity in circumpolar regions with different satellite indicators of greenness and photosynthesis. *Biogeosciences*, 15 (20):6221–6256, 2018. Publisher: Copernicus GmbH on behalf of the European Geosciences Union.

D. Zona, P. M. Lafleur, K. Hufkens, B. Bailey, B. Gioli, G. Burba, J. P. Goodrich, A. K. Liljedahl, E. S. Euskirchen, J. D. Watts, M. Farina, J. S. Kimball, M. Heimann, M. Göckede, M. Pallandt, T. R. Christensen, M. Mastepanov, E. López-Blanco, M. Jackowicz-Korczynski, A. J. Dolman, L. B. Marchesini, R. Commane, S. C. Wofsy, C. E. Miller, D. A. Lipson, J. Hashemi, K. A. Arndt, L. Kutzbach, D. Holl, J. Boike, C. Wille, T. Sachs, A. Kalhori, X. Song, X. Xu, E. R. Humphreys, C. D. Koven, O. Sonnentag, G. Meyer, G. H. Gosselin, P. Marsh, and W. C. Oechel. Earlier snowmelt may lead to late season declines in plant productivity and carbon sequestration in Arctic tundra ecosystems. *Scientific Reports*, 12(1):3986, December 2022. ISSN 2045-2322. doi: 10.1038/s41598-022-07561-1. URL https://www.nature.com/articles/s41598-022-07561-1.

Chapter 2

DECOMPOSING REFLECTANCE SPECTRA TO TRACK GROSS PRIMARY PRODUCTION IN A SUBALPINE EVERGREEN FOREST

R. Cheng, T. S. Magney, D. Dutta, D. R. Bowling, B. A. Logan, S. P. Burns, P. D. Blanken, K. Grossmann, S. Lopez, A. D. Richardson, J. Stutz, and C. Frankenberg. "Decomposing reflectance spectra to track gross primary production in a subalpine evergreen forest". In: *Biogeosciences* 17(18):4523-4544, 2022. DOI: 10.5194/bg-17-4523-2020.

2.1 Abstract

Photosynthesis by terrestrial plants represents the majority of CO_2 uptake on Earth, yet it is difficult to measure directly from space. Estimation of Gross Primary Production (GPP) from remote sensing indices represents a primary source of uncertainty, in particular for observing seasonal variations in evergreen forests. Recent vegetation remote sensing techniques have highlighted spectral regions sensitive to dynamic changes in leaf/needle carotenoid composition, showing promise for tracking seasonal changes in photosynthesis of evergreen forests. However, these have mostly been investigated with intermittent field campaigns, or with narrow-band spectrometers in these ecosystems. To investigate this potential, we continuously measured vegetation reflectance (400–900 nm) using a canopy spectrometer system, PhotoSpec, mounted on top of an eddy-covariance flux tower in a subalpine evergreen forest at Niwot Ridge, Colorado, USA. We analyzed driving spectral components in the measured canopy reflectance using both statistical and process-based approaches. The decomposed spectral components co-varied with carotenoid content and GPP, supporting the interpretation of the Photochemical Reflectance Index (PRI) and the Chlorophyll/Carotenoid Index (CCI). Although the entire 400-900 nm range showed additional spectral changes near the red-edge, it did not provide significant improvements in GPP predictions. We found little seasonal variation in both Normalized Difference Vegetation Index (NDVI) and the Near Infrared Vegetation Index (NIRv) in this ecosystem. In addition, we quantitatively determined needle-scale chlorophyll to carotenoid ratios as well as anthocyanin contents using full spectrum inversions, both of which were tightly correlated with seasonal GPP changes. Reconstructing GPP from vegetation reflectance using Partial Least Squares Regression (PLSR) explained approximately 87% of the variability in observed GPP. Our results linked the seasonal variation of reflectance to the pool size of photoprotective pigments, highlighting all spectral locations within 400–900 nm associated with GPP seasonality in evergreen forests.

2.2 Introduction

Terrestrial Gross Primary Production (GPP), the gross CO_2 uptake through photosynthesis, is the largest uptake of atmospheric CO_2 (Ciais et al., 2013), yet the uncertainties are large, hampering our ability to monitor and predict the response of the terrestrial biosphere to climate change (Ahlström et al., 2012). Hence, accurately mapping GPP globally is critical. In contrast to unevenly distributed ground-level measurements such as Fluxnet (Baldocchi et al., 2001), satellites can infer GPP globally and uniformly. Remote sensing techniques are based on the optical response of vegetation to incoming sunlight, which can track photosynthesis via the absorption features of photosynthetic and photoprotective pigments (Gamon et al., 1992, 2016; Liu and Huete, 1995; Rouse Jr et al., 1974). Progress is particularly important for evergreen forests, which can have large seasonal dynamics in photosynthesis but low variability in canopy structure and color. However, these promising techniques still lack a comprehensive evaluation/validation using both continuous in-situ measurements as well as process-based simulations.

GPP can be expressed as a function of photosynthetically active radiation (PAR), the fraction of PAR absorbed by the canopy (fPAR) and Light-Use Efficiency (LUE):

$$\mathrm{GPP} = \mathrm{PAR} \cdot \mathrm{fPAR} \cdot \mathrm{LUE}, \tag{2.1}$$

with LUE representing the efficiency of plants to fix carbon using absorbed light (Monteith, 1972; Monteith and Moss, 1977). The accuracy of remote sensing derived GPP is limited by the estimation of LUE, which is more dynamic and difficult to measure remotely than PAR and fPAR, particularly in evergreen ecosystems. There have been many studies inferring the light absorbed by canopies (i.e. fPAR) from Vegetation Indices (VIs) that estimate the 'greenness' of canopies (Glenn et al., 2008; Robinson et al., 2018; Running et al., 2004; Zhao et al., 2005), such as the Normalized Difference Vegetation Index (NDVI; Rouse Jr et al., 1974; Tucker, 1979), the Enhanced Vegetation Index (EVI; Huete et al., 1997; Liu and Huete, 1995) and the Near Infrared Vegetation Index (NIRv; Badgley et al., 2017). Current GPP data products derived from Equation (2.1) rely on the modulation of abiotic conditions to estimate LUE (Xiao et al., 2004). LUE is derived empirically by defining a general timing of dormancy for all evergreen forests with the same plant functional type (e.g. Krinner et al., 2005) or the same meteorological thresholds (e.g. Running et al., 2004). However, within the same climate region or plant functional type, forests are not identical — leading to uncertainties in estimated LUE (Gamon et al., 2016; Stylinski et al., 2002; Zuromski et al., 2018), which propagate to the estimation of GPP.

Because evergreen trees retain most of their needles and chlorophyll throughout the entire year (Bowling et al., 2018), LUE in evergreens is regulated by needle biochemistry. As LUE falls with the onset of winter due to unfavorable environmental conditions and seasonal downregulation of photosynthetic capacity, evergreen needles quench excess absorbed light via thermal energy dissipation that involves xanthophyll cycle and other pigments (Adams and Demmig-Adams, 1994; Demmig-Adams and Adams, 1996; Verhoeven et al., 1996; Zarter et al., 2006). Thermal energy dissipation is a primary de-excitation pathway measured by pulse-amplitude fluorescence as non-photochemical quenching (NPQ; Schreiber et al. (1986)). At the same time, a small amount of radiation, Solar-Induced Fluorescence (SIF), via the de-excitation of absorbed photons is emitted by photosystem II (Genty et al., 1989; Krause and Weis, 1991).

Some vegetation indices are sensitive to photoprotective pigments (e.g. carotenoids) and can characterize the seasonality of evergreen LUE with some success. For instance, the Photochemical Reflectance Index (PRI; Gamon et al., 1992, 1997) and Chlorophyll/Carotenoid Index (CCI; Gamon et al., 2016) both use wavelength regions that represent carotenoid absorption features around 531 nm at the leaf level (Wong and Gamon, 2015a,b; Wong et al., 2019) and show great promise for estimating photosynthetic seasonality (Hall et al., 2008; Hilker et al., 2011a). Due to the relatively invariant canopy structure in evergreen forests, CCI and PRI have been applied at the canopy level as well (Gamon et al., 2016; Garbulsky et al., 2011; Middleton et al., 2016). In addition, the Green Chromatic Coordinate (GCC; Richardson et al., 2009, 2018; Sonnentag et al., 2012), an index derived from the brightness levels of RGB canopy images, is also capable of tracking the seasonality of evergreen GPP (Bowling et al., 2018). However, the full potential of spectrally resolved reflectance measurements to explore the photosynthetic phenology of evergreens has not been comprehensively explored at the canopy scale. The evaluation of pigment-driven spectral changes in evergreen forests over the course of a season is necessary to determine where, when, and why certain wavelength regions could advance our mechanistic understanding of canopy photosynthetic and photoprotective pigments. However, this has not been done with both empirical and process-based methods using continuously measured canopy hyperspectral reflectance and in situ pigment samples.

Here, we used continuous measurements in both spectral space (full spectrum between 400–900 nm) and time (daily over an entire year) to evaluate the potential of hyperspectral canopy reflectance for better understanding the sensitivity of VIs to pigment changes that regulate GPP in evergreen forests. Continuous measurements of spectrally resolved reflectance at the canopy scale have so far been sparse at evergreen forest sites (Gamon et al., 2006; Hilker et al., 2011b; Porcar-Castell et al., 2015; Rautiainen et al., 2018; Wong et al., 2020). There are only a few empirical studies on hyperspectral canopy reflectance in evergreen forests (Singh et al., 2015;

Smith et al., 2002). Yet, empirically decomposed canopy spectral reflectance has been used as a predictor of maximum photosynthetic capacity (Barnes et al., 2017; Dechant et al., 2017; Meacham-Hensold et al., 2019; Serbin et al., 2012; Silva-Perez et al., 2018), GPP (Dechant et al., 2019; DuBois et al., 2018; Huemmrich et al., 2017, 2019; Matthes et al., 2015), and other physiological properties (Asner et al., 2011; Serbin et al., 2014; Ustin et al., 2004, 2009).

In contrast to empirical methods, process-based approaches, such as canopy Radiative Transfer Models (RTMs) can help to quantitatively link canopy photosynthesis with leaf-level contents of photosynthetic/photoprotective pigments (Feret et al., 2008; Jacquemoud et al., 2009). With RTMs, we can use spectrally resolved reflectance to directly derive leaf pigment contents (Féret et al., 2017; Jacquemoud et al., 1995) and plant traits (Féret et al., 2019) .

In addition to seasonal changes in pigment concentrations, canopy SIF was found to correlate significantly with the seasonality of photoprotective pigment content in a subalpine coniferous forest (Magney et al., 2019). Steady state SIF is regulated by NPQ and photochemistry (Porcar-Castell et al., 2014), and it provides complementary information on canopy GPP. Yang and van der Tol (2018) justified that the relative SIF, SIF normalized by the reflected near-infrared radiation, is more representative of the physiological variations of SIF as it is comparable to a SIF yield (Genty et al., 1989; Guanter et al., 2014). Our continuous optical measurements make it possible to differentiate mechanisms undergoing seasonal changes by comparing the decomposed reflectance spectrum against relative far-red SIF. Additionally, using relative SIF can effectively correct for incoming irradiance and account for the sunlit/shade fraction within the observation Field of View (FOV) of PhotoSpec (Magney et al., 2019).

In the present study, we analyzed continuous canopy reflectance data from PhotoSpec at a subalpine evergreen forest at the Niwot Ridge AmeriFlux site (US-NR1) in Colorado, US, and sought to understand the mechanisms controlling the seasonality of photosynthesis using continuous hyperspectral remote sensing. We first explored empirical techniques to study all seasonal variations in reflectance spectra, identified specific spectral regions that best explained the seasonal changes in GPP, and then linked these spectral features to pigment absorption features that impacted both biochemical and biophysical traits. We also used full spectral inversions using a canopy RTM to infer quantitative estimates of leaf pigment pool sizes. Finally, we compared the spring onset of photosynthesis captured by different methods, VIs, and relative SIF to determine the underlying mechanisms that contributed to photosynthetic phenology.

2.3 Material and methods

Study site

The high-altitude (3050 m above sea level) subalpine evergreen forest near Niwot Ridge, Colorado, US, is an active AmeriFlux site (US-NR1, Lat: 40.0329 °N, Lon: 105.5464 °W; tower height: 26 m; Blanken et al., 2019; Burns et al., 2015, 2016; Monson et al., 2002). Three species dominate: subalpine fir (*Abies lasiocarpa var. bifolia*), Englemann spruce (*Picea engelmannii*), and lodgepole pine (*Pinus contorta*) with an average height of 11.5 m, a leaf area index of 4.2 (Burns et al., 2016), and minimal understory. The annual mean precipitation and air temperature are 800 mm and 1.5 °C, respectively (Monson et al., 2002). The high elevation creates an environment with cold winters (with snow present more than half the year), while the relatively low latitude (40°N) allows for year-round high solar irradiation (Monson et al., 2002). Thus, trees have to dissipate a considerable amount of excess sunlight during winter dormancy, which makes this forest an ideal site for studying seasonal variation of NPQ including the sustained component of it during dormancy (Bowling et al., 2018; Magney et al., 2019).

Continuous tower-based measurements of canopy reflectance

PhotoSpec (Grossmann et al., 2018) is a 2D scanning telescope spectrometer unit originally designed to measure SIF. It also features a broad-band Flame-S spectrometer (Ocean Optics, Inc., Florida, USA), used to measure reflectance from 400 to 900 nm at a moderate (full-width-at-half-maximum = 1.2 nm) spectral resolution with a FOV of 0.7° (more details in Grossmann et al. (2018); Magney et al. (2019)). In the summer of 2017, we installed a PhotoSpec system on the top of the US-NR1 eddy-covariance tower, from where we can scan the canopy by changing both viewing azimuth angle and zenith angles. On every other summer day and every winter day, PhotoSpec scans the canopy by changing view zenith angle with small increments at fixed view azimuth angles, i.e. elevation scans. Only one azimuth position is kept after Oct 18, 2017 to protect the mechanism from potentially damaging winter conditions at the site. Spectrally resolved reflectance was calculated using direct solar irradiance measurements via a cosine diffuser mounted in the upward nadir direction (Grossmann et al., 2018) as well as reflected radiance from the canopy. The reflectance data used in this study are from Jun 16, 2017, to Jun 15, 2018.

Here, we integrated all elevation scans to daily-averaged reflectance (every other day before Oct 18, 2017) by using all scanning viewing directions with vegetation in the field of view over the course of a day, filtering for both low light conditions and thick clouds by requiring PAR to be both at least 100 μmol $m^{-2}s^{-1}$ and 60% of theoretical clear-sky PAR. A detailed description of data processing can be found in appendix B. To further test whether bi-directional reflectance effects impacted our daily averages, we compared the NDVI and NIRv at various canopy positions given a range of solar zenith and azimuth angles (Figure 2.10-2.12). Neither of the daily averaged VIs was substantially impacted by the solar geometry supporting the robustness of daily averaged canopy reflectance. An additional analysis (Figure 2.13) has also shown the variation in phase angle at a daily time step is not a critical factor for the change in reflectance.

About 49 winter days exhibited significantly higher reflectances, attributable to snow within the field of view, which we corroborated with canopy RGB imagery from the tower. After removing data strongly affected by snow and excluding the days of instrument outages, 211 valid sample days remained, among which 96 valid sample days were between DOY 100-300. The daily-averaged reflectance was computed as the median reflectance from all selected scans for a single day, which was then smoothed by a 10-point (3.7 nm) box-car filter over the spectral dimension (400 - 900 nm) to remove the noise in the spectra. Figure 2.1(a) shows the seasonally averaged and spectrally resolved canopy reflectances measured by PhotoSpec.

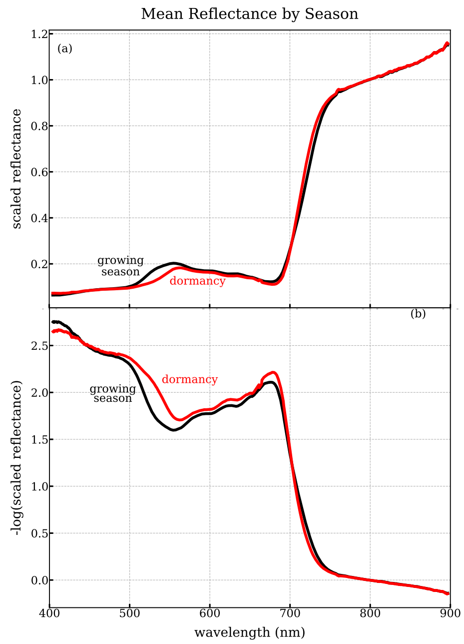

Figure 2.1: (a) Seasonally averaged canopy reflectance in winter dormancy (red) and the growing season (black) from PhotoSpec. (b) Seasonally averaged negative logarithm transformation of reflectance (400 - 900 nm). For comparison, we normalized the reflectance by the value at 800 nm on each day. Here, we referred to Nov 13 - Apr 18 as dormancy, and Jun 2 - Aug 21 as the main growing season. The seasonal averaged canopy reflectance is composed of 39 daily-average reflectance in the growing season and 113 daily-averaged reflectance in the dormancy.

To further emphasize the change in reflectance as a result of changes in pigment contents, we transformed the reflectance (shown as R_λ) using the negative logarithm (Equation (2.2)), as light intensity diminishes exponentially with pigment contents (Horler et al., 1983).

$$R_\lambda \propto exp(-C \cdot \sigma(\lambda)) \tag{2.2a}$$

$$C \cdot \sigma(\lambda) \propto -log(R_\lambda) \tag{2.2b}$$

with σ = absorption cross section of pigments.

Therefore, the log-transformed reflectance (Figure 2.1(b)) should correlate more linearly with pigment contents (shown as C). We also considered a variety of typical VIs using the reflectance data from PhotoSpec, such as:

$$\mathrm{NDVI} = \frac{R_{800} - R_{670}}{R_{800} + R_{670}} \text{ (Rouse Jr et al., 1974)} \tag{2.3a}$$

$$\mathrm{NIRv} = \mathrm{NDVI} * R_{800} \text{ (Badgley et al., 2017)} \tag{2.3b}$$

$$\mathrm{PRI} = \frac{R_{531} - R_{570}}{R_{531} + R_{570}} \text{ (Gamon et al., 1992)} \tag{2.3c}$$

$$\mathrm{CCI} = \frac{R_{526-536} - R_{620-670}}{R_{526-536} + R_{620-670}} \text{ (Gamon et al., 2016)} \tag{2.3d}$$

$$\mathrm{GCC} = \frac{R_{Green}}{R_{Red} + R_{Green} + R_{Blue}} \text{ (Richardson et al., 2009).} \tag{2.3e}$$

In order to calculate GCC, we convolved the reflectance using the instrumental spectral response function (Figure 2.17; Wingate et al., 2015) of the StarDot NetCam SC 5 MP IR (StarDot Technologies, Buena Park, CA, USA), which is the standard camera model used by the PhenoCam Network protocol (Sonnentag et al., 2012).

In addition to the reflectance measurments, we also included relative SIF, far-red SIF normalized by the reflected near-infrared radiance at 755 nm. The far-red SIF (745–758 nm, Grossmann et al., 2018) was measured simultaneously with reflectance with a QEPro spectrometer (Ocean Optics, Inc., Florida, USA). The daily relative SIF was processed in the same fashion as the reflectance.

Eddy covariance measurements and LUE

Observations of Net Ecosystem Exchange (net flux of CO_2, NEE), PAR, and meteorological variables made at the US-NR1 tower are part of the official AmeriFlux Network data (Burns et al., 2016). GPP was estimated in half-hourly intervals (Reichstein et al., 2005) using the REddyProc package (Wutzler et al., 2018), allowing us to compute LUE (Gamon et al., 2016; Goulden et al., 1996) at half-hourly intervals.

According to the light response curves, GPP is a nonlinear function of PAR (Figure 2.2; Harbinson, 2012). Magney et al. (2019) showed that fPAR does not significantly vary with seasons. We started to observe a photosynthetic saturation between 500-1000 μmol $m^{-2}s^{-1}$ of PAR (Figure 2.2), when the carboxylation rate, driven by maximum carboxylation rate (V_{cmax}), became the limiting factor (Farquhar et al., 1980). Thus, we defined the light-saturated GPP (GPP_{max}), as the mean half-hourly GPP at PAR levels between 1000 and 1500 μmol $m^{-2}s^{-1}$, a range which was covered throughout the year (Figure 2.2), even in winter. Therefore, GPP_{max} was less susceptible to short term changes in PAR. Yet due to the lower light intensity during storms, GPP_{max} was not always available. As suggested by the low PAR value at which light saturation happened, plants remained in a light saturated condition for most of the daytime. A higher GPP_{max} indicates a greater V_{cmax} and maximum electron transport rate (J_{max}) when the variation of GPP_{max} is independent from stomatal conductance and intercellular CO_2 concentration (Leuning, 1995). Therefore, GPP_{max} was closely correlated with daily LUE driven by physiology (see section 2.4 in the supplementary material).

We refrained from normalizing GPP_{max} by APAR due to some of APAR measurements (see section 2.1 in the supplementary material) not available in the beginning of growing season. GPP_{max} was significantly linearly correlated with normalized GPP_{max} by APAR (Figure 2.20).

We also included Air Temperature (T_{air}) and Vapor Pressure Deficit (VPD) provided from the AmeriFlux network data. Daytime daily mean T_{air} and VPD were computed from averaging the half-hourly T_{air} and VPD when PAR was greater than 100 μmol $m^{-2}s^{-1}$.

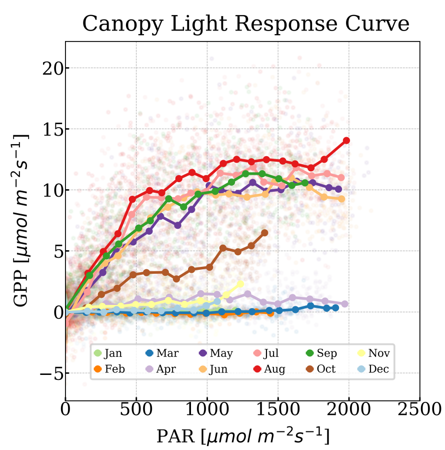

Figure 2.2: Half-hourly GPP as a function of PAR during the measurement period. Points were colored by month. Bold points were the median GPP when PAR was binned every 100 μmol $m^{-2}s^{-1}$ approximately. The solid lines represent the canopy light response curve.

Pigment measurements

To link canopy reflectance with variations in pigment contents, we used pigment data (Bowling and Logan, 2019; Bowling et al., 2018; Magney et al., 2019) at monthly intervals over the course of the sampling period. Here, we focused on the xanthophyll cycle pool size (Violaxanthin + Antheraxanthin + Zeaxanthin, V+A+Z), total carotenoid content (car) and total chlorophyll content (chl) measured on *Pinus* *contorta* and *Picea engelmannii* needles with units of moles per unit fresh mass. car includes V+A+Z, lutein, neoxanthin, and beta-carotene. We also computed the ratio of chlorophyll to carotenoid contents (chl:car), because CCI derived from Moderate Resolution Imaging Spectroradiometer (MODIS) can track chl:car (Gamon et al., 2016). Overall, we can match 10 individual leaf-level sampling days for both pine and spruce samples with reflectance measured within ± 2 days. Among these 10 valid sample days, 6 sample days are between DOY 100-300.

Data-driven spectral decomposition

We assumed that the spectrally resolved reflectance is a result of mixed absorption processes by different pigments. This allowed us to apply an Independent Component Analysis (ICA; Hyvärinen and Oja, 2000) to decompose the log-transformed reflectance matrix (day of the year in rows and spectral dimension in columns) into its independent components. An advantage of the ICA is that it can separate a multivariate signal into additive subcomponents that are maximally independent, without the condition of orthogonality (Comon, 1994). We extracted three independent components, which explained more than 99.99% of the variance, using the ICA algorithm (fastICA, python package scikit-learn v0.21.0; section 4 in the supplementary material), such as:

$$-log(R_{\lambda,\mathrm{DOY}}) = \sum_{i=1,2,3} (\text{spectral component}_{\lambda}^{i} \cdot \text{temporal loading}_{\mathrm{DOY}}^{i}), \qquad (2.4)$$

where i is the i'th component in spectral space.

The decomposed spectral components revealed characteristic features that explain most of the variance in the reflectance matrix, which dictated the time-independent spectral shapes of pigment absorption features based on Equation (2.2). The corresponding temporal loadings showed temporal variations of these spectral features, i.e. the variations of pigment contents. We will introduce the method of extracting pigment absorption features in a quantitative model-driven approach in section 2.3.

In addition to analyzing the transformed reflectance alone, we empirically correlated the reflectance with GPP_{max} using Partial Least Squares Regression (PLSR, python package scikit-learn v0.21.0). PLSR is a predictive regression model which solves for a coefficient that can maximally explain the linear covariance of the predictor with multiple variables (Geladi and Kowalski, 1986; Wold et al., 1984). PLSR has been used to successfully predict photosynthetic properties using reflectance matrices in previous studies from the leaf to canopy scales (e.g. Barnes et al., 2017; Serbin et al., 2012, 2015; Silva-Perez et al., 2018; Woodgate et al., 2019). Applying the PLSR to the hyperspectral canopy reflectance and GPP_{max} resulted in a time-independent coefficient that emphasizes the key wavelength regions which contribute to the covariation of reflectance and GPP_{max}, such as:

$$\text{GPP}_{\text{max,DOY}} = -log(R_{\lambda,\text{DOY}}) \times \text{PLSR coefficient}_{\lambda}^{\text{GPP}_{\text{max}}}. \tag{2.5}$$

We implemented another set of PLSR analyses on the reflectance with individual pigment measurement as the target variable, such as the mean values of V+A+Z, car, and chl:car, such as:

$$\text{pigment measurement} = -log(R_{\lambda,\text{DOY}}) \times \text{PLSR coefficient}_{\lambda}^{\text{pigment measurement}}. \tag{2.6}$$

We did not include chl as one of the target variables in this PLSR analysis since Bowling et al. (2018) and Magney et al. (2019) have already shown chl did not vary seasonally in our study site. Fitting the minimal variance in chl will lead to over fitting the PLSR model.

Comparing the PLSR coefficient of pigment measurements at the leaf level with the PLSR coefficient of GPP_{max} connected the changes in GPP_{max} to the pool size of photoprotective pigments, because the reflectance is regulated by the absorption of pigments.

Process-based methods

PROSPECT+SAIL (PROSAIL, Jacquemoud et al., 2009) is a process-based 1-D canopy RTM that models canopy reflectance, given canopy structure information (SAIL) as well as leaf pigment contents (PROSPECT) (Jacquemoud and Baret, 1990; Vilfan et al., 2018).

We used PROSAIL (with PROSPECT-D, Féret et al., 2017) to compute the derivative of the daily-averaged negative logarithm transformed reflectance with respect to individual pigment contents, namely chlorophyll content (chlorophyll Jacobian, $\frac{\partial -log(R)}{\partial C_{chl}}$) and carotenoid content (carotenoid Jacobian, $\frac{\partial -log(R)}{\partial C_{car}}$) (Dutta et al., 2019). This helped explain the decomposed spectral components from the empirical analysis.

We also used PROSAIL to infer pigment contents (i.e. C_{chl}, C_{car}, C_{ant}) by optimizing the agreement between PROSAIL-modeled reflectance and measured canopy daily-mean reflectance from PhotoSpec. We fixed canopy structural parameters (e.g. the LAI to 4.2, as reported in Burns et al. (2015)) and fitted leaf pigment compositions as well as a low order polynomial for soil reflectance (appendix C), similar to Vilfan et al. (2018) and Féret et al. (2017). The cost function J in Equation (2.7) represents a least-squares approach, where $\hat{R}$ is the modeled reflectance.

$$\mathrm{J} = \sum_{\lambda=450nm}^{800nm} (R_\lambda - \hat{R}_\lambda)^2. \tag{2.7}$$

We used the spectral range between 450 and 800 nm, which encompasses most pigment absorption features.

2.4 Results and discussion

Seasonal cycle of $\mathbf{GPP_{max}}$ and environmental conditions

As can be seen in Figure 2.3, the subalpine evergreen forest at Niwot Ridge exhibits strong seasonal variation in GPP, T_{air}, VPD, GPP_{max}, and PAR. GPP and GPP_{max} dropped to zero while sufficient PAR, required for photosynthesis, was still available in the dormancy, which suggests that the abiotic environmental factors impact photosynthesis seasonality nonlinearly and jointly.

Abiotic factors played a strong role in regulating GPP_{max} in this subalpine evergreen forest over the course of the season. For instance, there was a strong dependence of GPP_{max} with T_{air}. However, photosynthesis completely shut down during dormancy, even when the T_{air} exceeded 5°C (Figure 2.3). During the onset and cessation periods of photosynthesis, GPP_{max} rapidly increased with temperature (Figure 2.22 left panel), potentially because needle temperature co-varied with T_{air}, and needle temperature controls the activity of photosynthetic enzymes which affect V_{cmax}. Spring warming approaches the optimal temperature for photosynthetic enzymes, leading to activation of photosynthesis, while cooling in the early winter inhibits these enzymes (Rook, 1969). Warming in spring melted frozen boles and made them available for water uptake (Bowling et al., 2018), and thus caused the recovery of GPP_{max} (Monson et al., 2005). Once the temperature was around the optimum (in the growing season), T_{air} was no longer the determining factor for photosynthesis. Higher VPD caused by rising T_{air} can stress the plants such that stomata closed, intercellular CO_2 reduced and photosynthesis decreased (Figure 2.22 right panel). When intercellular CO_2 concentration was not a limiting factor, GPP_{max} was more representative of V_{cmax} and did not vary T significantly.

Seasonal cycle of reflectance

In Figure 2.4, the Jacobians show the maximum sensitivity of the reflectance spectral shape to carotenoid content at 524 nm, and near 566 nm and 700 nm for chlorophyll.

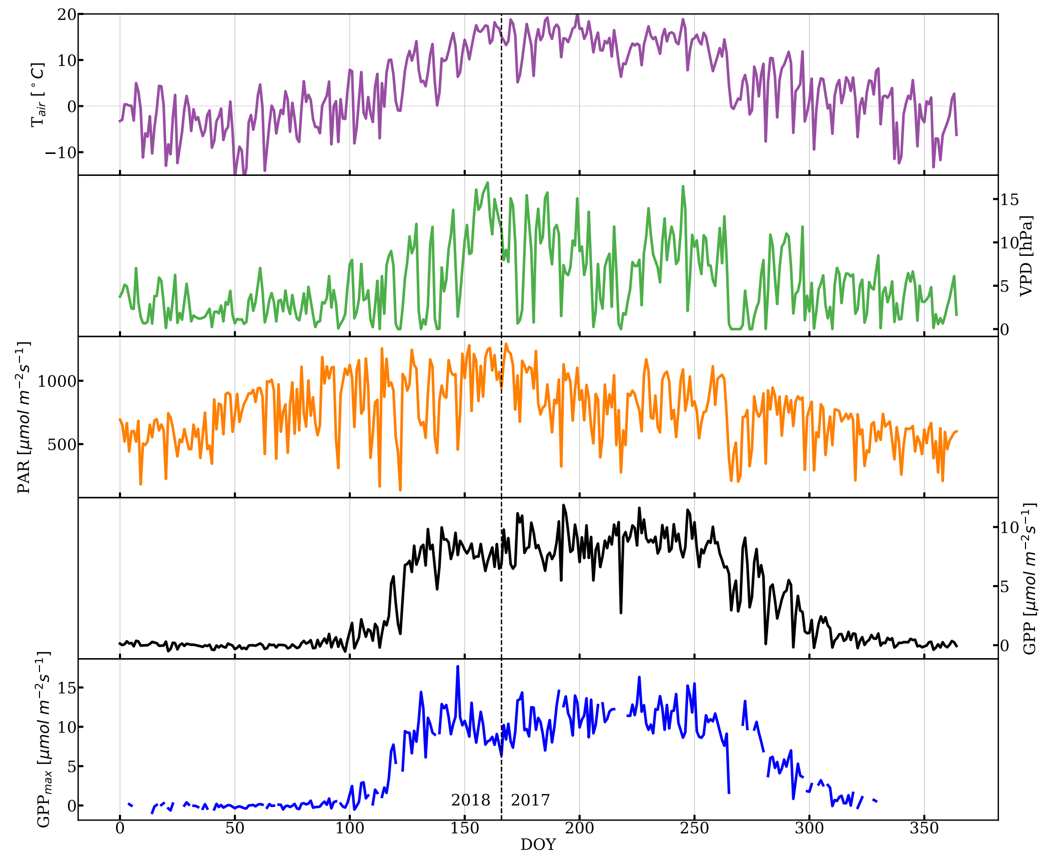

Figure 2.3: Daily-averaged time series of Air Temperature (T_{air}), Vapor Pressure Deficit (VPD), Photosynthetically Active Radiation (PAR), Gross Primary Production (GPP) from half-hourly data when PAR was greater than 100 μmol $m^{-2}s^{-1}$, and time series of GPP_{max}. DOY 166 (2017) was the first day of observation. The vertical dashed line divides the observations from Day of Year (DOY) for year 2017 and 2018.

The first peak of the chlorophyll Jacobian covers a wide spectral range in the visible, while the second peak around the red edge is narrower.

It can be seen that the first spectral ICA component has a similar shape as the chlorophyll Jacobian. The corresponding temporal loading has a range between -0.2 to 0.2 without any obvious seasonal variation, consistent with a negligible seasonal cycle in chlorophyll content as shown in the pigment analysis. However, there is a gradual increase before DOY 50 in the first temporal loading, which appears to be anti-correlated with the temporal loading of the second ICA structure.

Two major features in the second spectral component can be observed. One is a negative peak centered around 530 nm, which aligns with the carotenoid Jacobian. At the negative logarithm scale, the negative values resulting from the negative

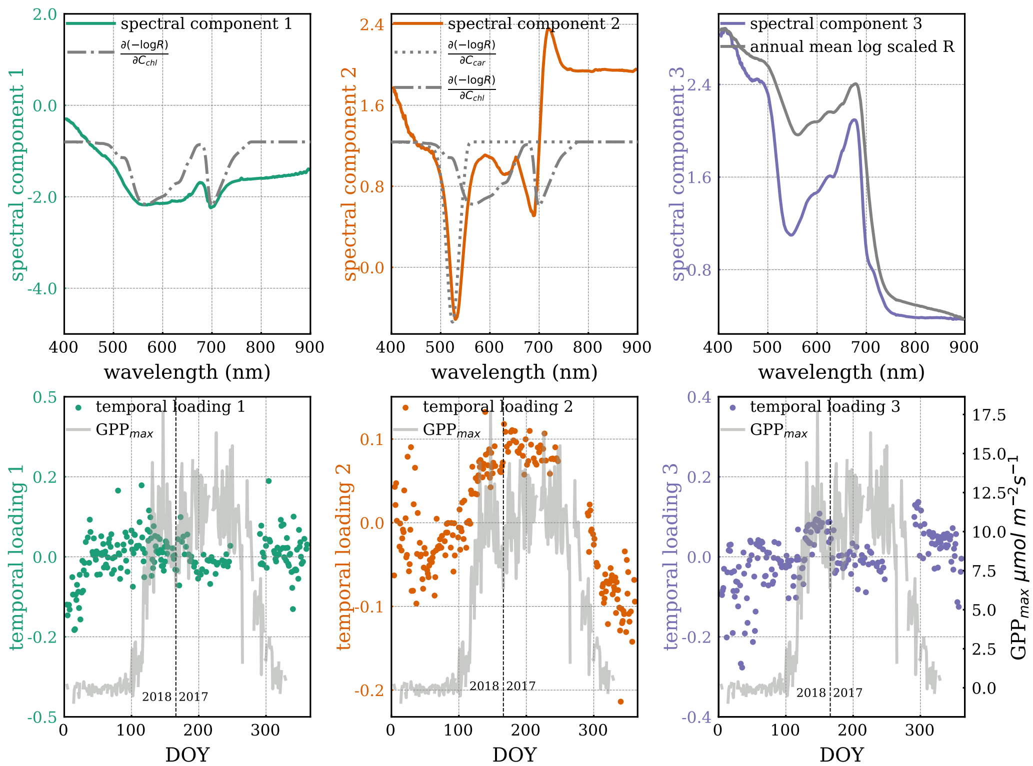

Figure 2.4: A set of three spectral components (top, colored) and corresponding temporal loadings (bottom, colored) from ICA decomposition. The first spectral component is overlaid with the chlorophyll Jacobian ($\frac{\partial{-log(R)}}{\partial C_{chl}}$, dash-dotted), and the second spectral component is overlaid with the carotenoid Jacobian ($\frac{\partial{-log(R)}}{\partial C_{car}}$, dotted). The third spectral component is overlaid on the annual mean shape of transformed reflectance spectra. Temporal loadings are overlaid with $\mathrm{GPP}_{\mathrm{max}}$ (grey line). The axis of Jacobians is not shown because its magnitude is arbitrary here. The vertical dashed line divides the observations from DOY for year 2017 and 2018.

ICA spectral peak multiplied by the positive ICA temporal loadings (growing season in Figure 2.4 middle plots) indicate there were fewer carotenoids during the growing season (Equation (2.2) and Equation (2.4)). Conversely, positive values resulting from a negative spectral peak multiplied by the negative temporal loadings (dormancy in Figure 2.4 middle plots) indicate there were more carotenoids during dormancy (i.e. sustained photoprotection via the xanthophyll pigments; Bowling et al., 2018). Another feature is the valley-trough shape, which is co-located with the chlorophyll Jacobian center at the longer wavelength in the red-edge region. The center of this feature occurs at the shorter-wavelength edge of the chlorophyll Jacobian but does not easily explain changes in total chlorophyll content, which should show equal changes around 600 nm. The corresponding temporal loading apparently varied seasonally with GPP_{max}.

The second temporal loading transitioned more gradually from dormancy to the peak growing season than GPP_{max}. Unfortunately, we were missing data to evaluate the relative timing of GPP_{max} cessation.

The third spectral component is similar to the mean shape of reflectance spectra. Its temporal loading held around zero throughout the year.

Overall, the second ICA spectral component is more representative of the seasonal variation in the magnitude of total canopy reflectance than the other spectral components. The spectral changes around the red-edge in the second component is interesting and might be related to structural needle changes in chlorophyll-a and chlorophyll-b contributions (de Tomás Marín et al., 2016; Rautiainen et al., 2018), which are not separated in PROSPECT.

CCI and PRI(Figure 2.5(a-b)) followed the seasonal cycle of GPP_{max} closely. CCI and PRI use reflectance near the center of the 530 nm valley feature (Equation (2.3)c-d), the spectral range that is most sensitive to the change of carotenoid content, so that they matched changes in GPP_{max} very well. PRI was the smoothest throughout the year, without any significant fluctuations within the growing season, as opposite to what was observed in GPP_{max}, which co-varied with T_{air} and VPD (Figure 2.22 and 2.23). This performance is intriguing given that PRI was originally developed to track short term variations in LUE (Gamon et al., 1992), such as day-to-day and sub-seasonal scales.

GCC (Figure 2.5(c)) also correlated well with GPP_{max}, but less than CCI and PRI. As can be seen in Figure 2.17, the peak of the green channel used for GCC is close to the carotenoid Jacobian peak, while the red channel feature covers a part of chlorophyll Jacobian feature. This explained the sensitivity of the GCC to changes in both carotenoid content as well as chlorophyll. The bands used in GCC are broader than the ones used by PRI and CCI, however it still captured these variations and can be computed using RGB imagery. Gentine and Alemohammad (2018) found that the green band helps to reconstruct variations in SIF using reflectances from MODIS. While they speculated that most variations in SIF are related to variations in $PAR \cdot fPAR$ (Gentine and Alemohammad, 2018), we suggest here that the green band indeed captures variations in LUE as well.

NDVI (Figure 2.5(e)) and NIRv (Figure 2.5(f)) did not show an obvious seasonal variability.

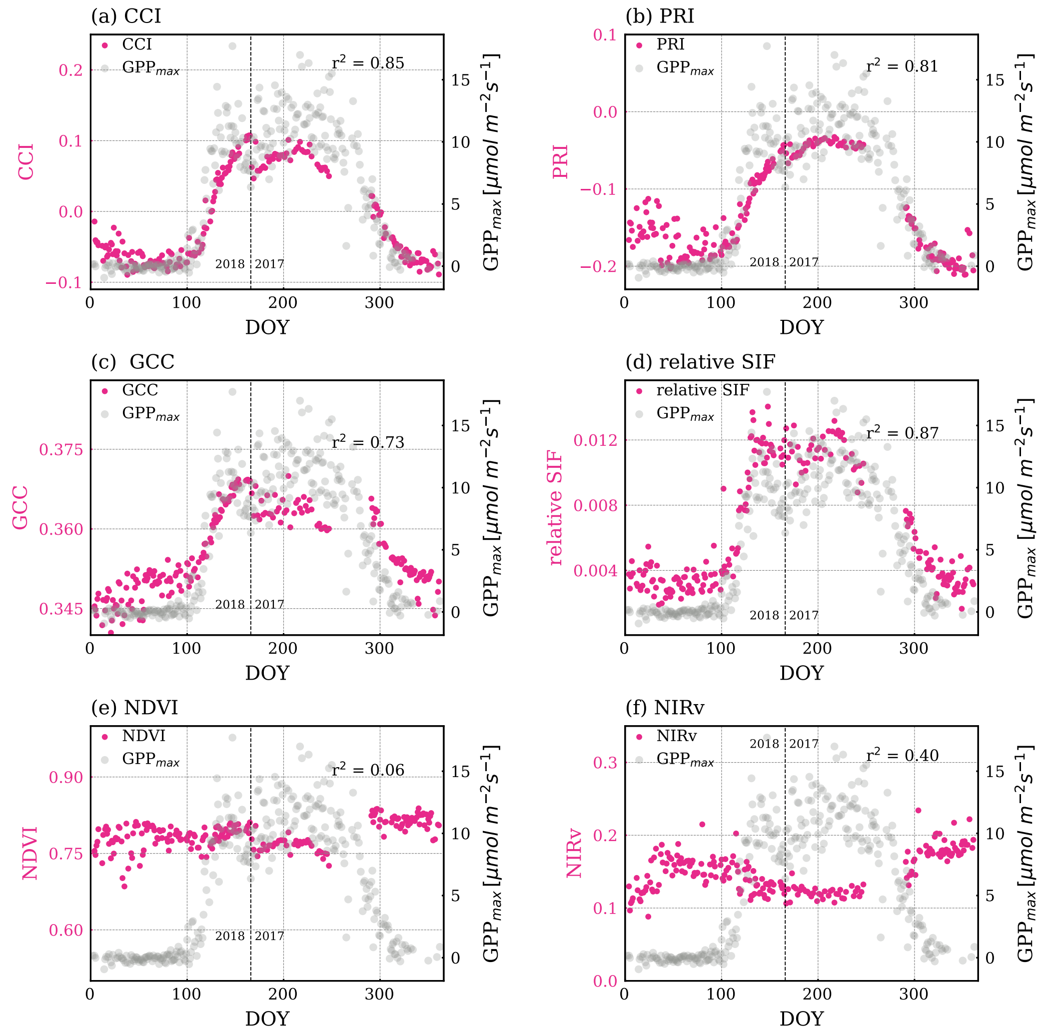

Figure 2.5: Magenta points are time series of VIs: (a) CCI, (b) PRI, (c) GCC, (d) relative SIF (e) NDVI (f) NIRv.The grey points in the background show GPP_{max}. The Pearson-r^2 values of regressing VIs and GPP_{max} are noted in each plot. The p values of all correlations in this figure are less than 0.005. The vertical dashed line divides the observations from DOY for year 2017 and 2018.

Similar to the ICA components, all VIs were quite noisy during dormancy, especially prior to DOY 50. This noise may be due to snow because we only removed the reflectance when the canopy was snow covered. Scattered photons possibly still reached the telescope when there was snow on the ground, which is true for our study site as snowpack exists in winter (Bowling et al., 2018).

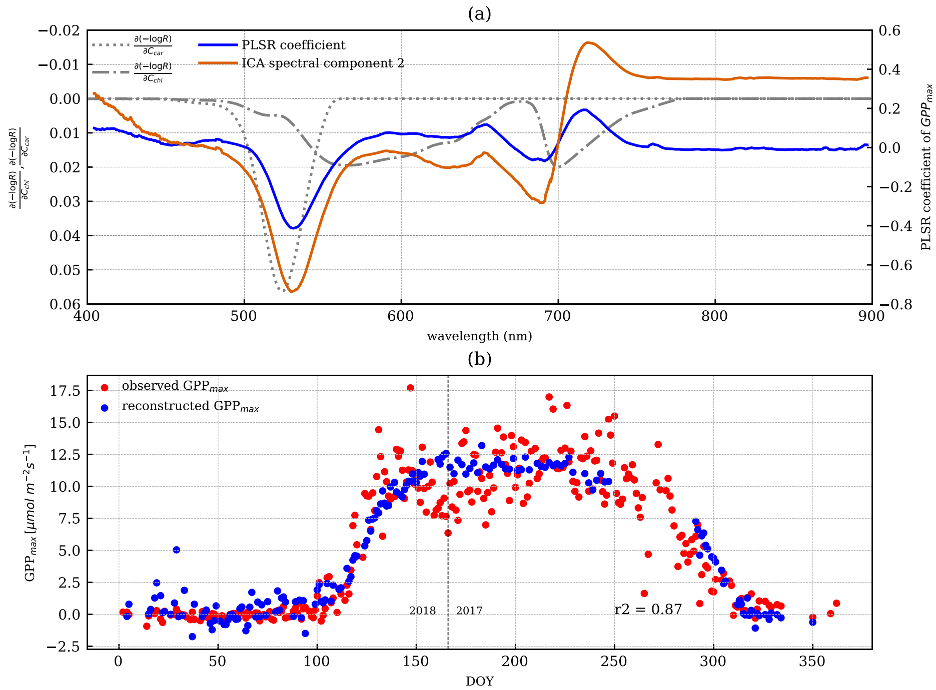

Figure 2.6: (a) The PLSR coefficient of reflectance with GPP_{max} is the blue line. The overlaid dash-dotted and dotted lines are chlorophyll and carotenoid Jacobians, respectively. The overlaid orange solid line is the second ICA spectral component, which was scaled to fit to the plot without a y-axis. (b) The reconstructed GPP_{max} (blue) by PLSR is overlaid with the observed GPP_{max} (red). The vertical dashed line divides the observations from DOY for year 2017 and 2018.

PLSR coefficients of reflectance with GPP_{max} and pigment measurements

The spectral shape of the PLSR coefficient with GPP_{max} highlighted a peak (centering at 532 nm) near that of the carotenoid Jacobian with the same valley-trough feature observed near the second peak of the chlorophyll Jacobian (Figure 2.6(a)).

The reconstructed GPP_{max} captured the onset and cessation of growth, while the day-to-day noise in reflectance during dormancy propagated to the reconstructed GPP_{max} (-2 to 5 μmol $m^{-2}s^{-1}$). During the growing season, the day-to-day variations in GPP_{max} were not captured by any of the methods using pigment absorption features (Figure 2.5(a-c) and Figure 2.6(b)), which indicates those variations were not related to pigment content, but rather changes in environmental conditions that lead to day-to-day changes in photosynthesis (Figure 2.22). Overall, the observed GPP_{max} was significantly correlated with the PLSR reconstruction (Pearson-r^2=0.87), but very similar compared to CCI and PRI. A similar PLSR model of reflectance but with pigment measurements (Figure 2.7) showed a direct link between pigment contents

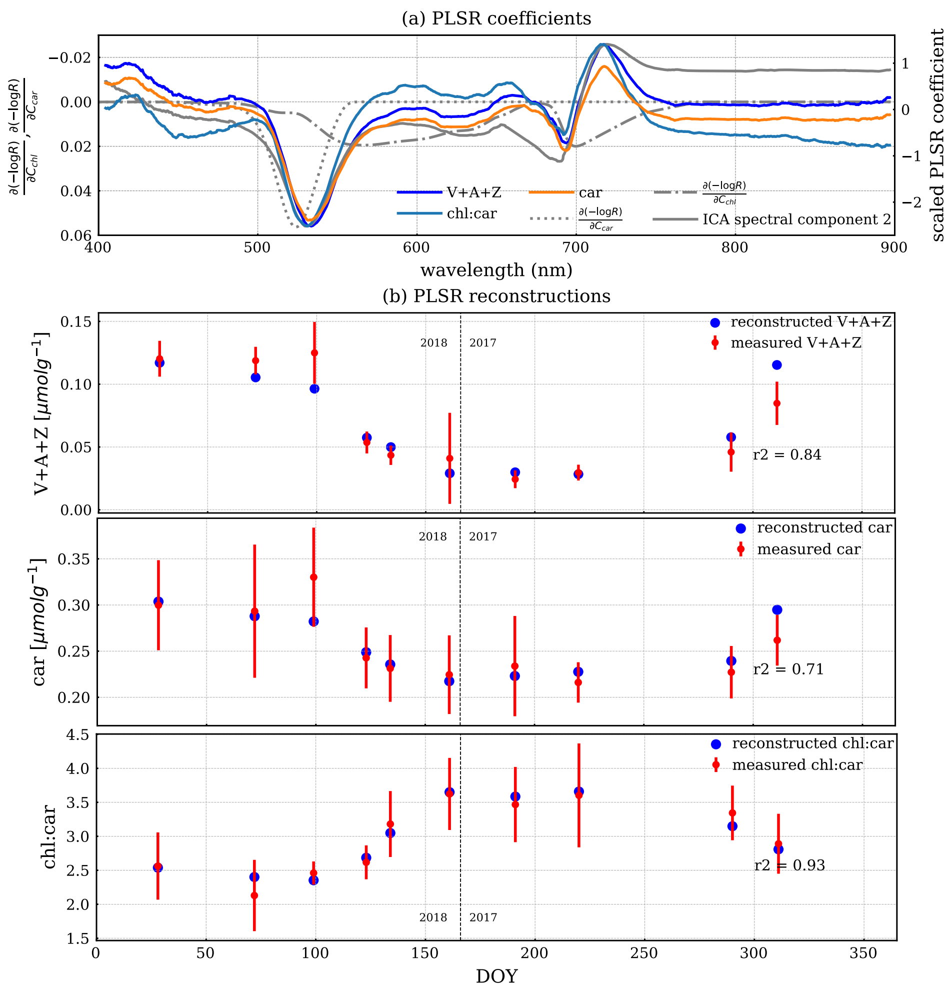

Figure 2.7: (a) PLSR coefficients of reflectance and three pigment measurements. The overlaid dash-dotted and dotted lines are chlorophyll and carotenoid Jacobians, respectively. The overlaid solid grey line is the second ICA spectral component, which is scaled to fit to the plot without a y-axis. (b) The reconstructed pigment measurements (blue) by PLSR is overlaid with the measured mean pigment measurements (red). The error bar is one standard deviation of the measurements. The vertical dashed line divides the observations from DOY for year 2017 and 2018.

and reflectance. It can be seen that the PLSR coefficients of reflectance are very similar, irrespective of the target variable. They feature a valley near the peak of the carotenoid Jacobian and a valley-trough feature near the peak at the longer wavelength of chlorophyll Jacobian. This spectral shape is also very similar to the second ICA spectral component and PLSR coefficients of GPP_{max}. V+A+Z, chl:car, and car were all nicely reconstructed by using the PLSR coefficients and reflectance (Figure 2.7(b)). The reconstructed V+A+Z, car, and chl:car are correlated with the measured ones with Pearson-r^2 values of 0.84, 0.71 and 0.93, respectively.

The second ICA component and PLSR empirically showed the seasonality of reflectance using two different empirical frameworks. ICA only used the reflectance, while the PLSR model accounts for variations in both reflectance and GPP_{max} or pigment content. Yet both ICA and PLSR agreed on similar spectral features that co-varied seasonally with GPP_{max}. This indicates that the resulting spectral features were primarily responsible for representing this seasonal cycle. The overlap of these features with the chlorophyll/carotenoid absorption features showed that the seasonality of GPP_{max} was related to variation in pigment content at the canopy scale, which was directly validated with similar PLSR coefficient of reflectance and pigment contents. These results are consistent with leaf-level measurements of a higher ratio of chlorophyll to carotenoid content during the growing season in this forest (Figure 2.7).

The highlighted spectral feature around 530 nm from ICA and PLSR closely overlaps with one of the bands used in CCI, PRI, and GCC (Equation (2.3)) which provides a justification that these VIs can remarkably capture the LUE seasonality. The comparable Pearson r^2 values of PLSR, CCI, and PRI with GPP_{max} suggest the pigment-driven seasonal cycle of GPP_{max} is sufficiently represented by CCI and PRI. The spectral feature around the red-edge does not make PLSR significantly more correlated with GPP_{max} than CCI or PRI, which implies the feature is not driven by total chlorophyll or carotenoid contents.

Process-based estimation of pigment content

PROSAIL inversion results further supported the link between canopy reflectance, pigment contents and GPP_{max}. Figure 2.8 shows a continuous time-series of C_{chl}, C_{car}, Anthocyanin content (C_{ant}), and $\frac{C_{chl}}{C_{car}}$ derived from the PROSAIL canopy RTM inversion model. Examples of simulated and measured reflectance spectra shown are in Figure 2.15. Anthocyanins are another type of photoprotective pigment (Gould, 2004; Lee and Gould, 2002; Pietrini et al., 2002) that protects the plants from high light intensity (Hughes, 2011). The pigment inversions closely matched the seasonality of GPP_{max}. $\frac{C_{chl}}{C_{car}}$ showed the greatest sensitivity in capturing the seasonal cycle, with the strongest correlation to leaf level measurements (Figure 2.8 (c)). The inverted C_{chl} had the weakest empirical relationship with the measured one (Figure 2.8(a) right panel). Apparently, some of the inversion errors of individual C_{car} and C_{chl} contents canceled out in the ratio, making the ratio more stable. C_{ant} performed similarly as C_{car}, since they both are photoprotective, and the anthocyanins absorb at 550 nm (Sims and Gamon, 2002), which is close to the

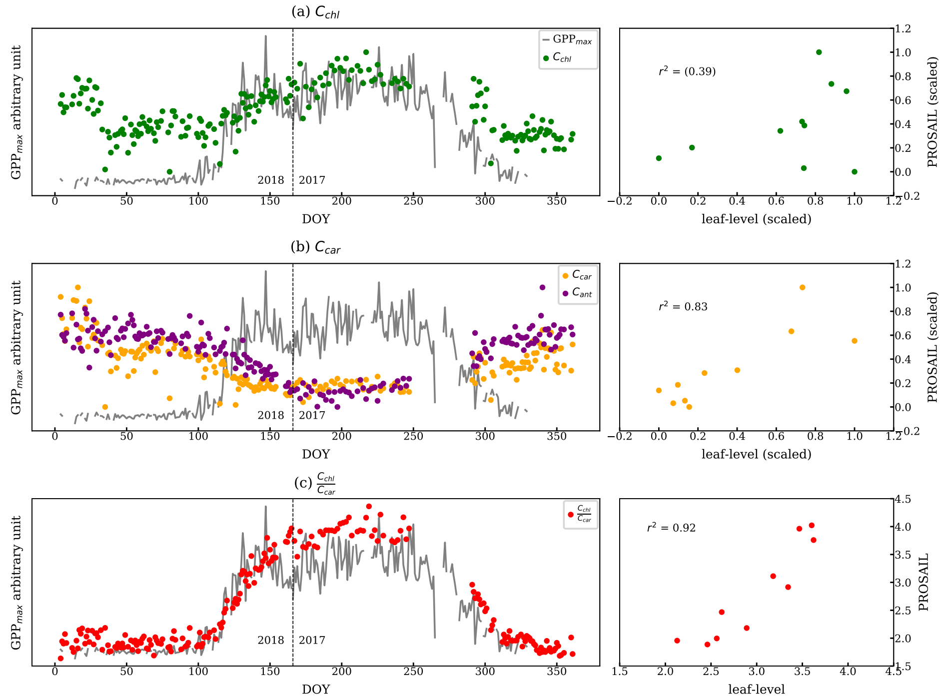

Figure 2.8: The left panels are the estimations of (a) C_{chl}, (b) C_{car}, C_{ant} and (c) $\frac{C_{chl}}{C_{car}}$ from the PROSAIL overlaid with the GPP$_{\mathrm{max}}$. We normalized two metrics because they report the pigment contents in different units. The vertical dashed line divides the observations from DOY for year 2017 and 2018. The plots on the right compare the pigment contents from leaf-level measurements and using PROSAIL: (a) chl vs. C_{chl}, (b) car vs. C_{car}, and (c) chl:car vs. $\frac{C_{chl}}{C_{car}}$. The correlations are statistically significant except C_{chl}.

center of carotenoid absorption feature. Even though we lacked field measurements of anthocyanins to validate anthocyanins retrievals, the inversions showed that more than just carotenoid content can be obtained from full-spectral inversions.

Strictly speaking, the complex canopy structure of evergreens makes the application of 1D canopy RTMs such as PROSAIL difficult (Jacquemoud et al., 2009; Zarco-Tejada et al., 2019). Yet, Ali et al. (2016); Moorthy et al. (2008); Zarco-Tejada et al. (2019) reasonably discussed the pigment retrieval in conifer forests with careful applications. In our study, the reflectance was collected from needles with a very small FOV, and our study site has a very stable canopy structure throughout a year (Burns et al., 2016). Thus, the inversion results are meaningful for discussing the seasonality of pigment contents. In the future, radiative transfer models that properly describe conifer forests, such as LIBERTY (Dawson et al., 1998), could be used.

Comparison across methods

Although decomposing the hyperspectral canopy reflectance and using relative SIF (Figure 2.5(d)) both successfully tracked the seasonal cycle of evergreen LUE, they underlie different de-excitation processes. During the growing season, environmental conditions primarily drove the day-to-day variations in GPP_{max}. Relative SIF responded to such environmental stresses (vander Tol et al., 2014) so that it appeared to track sub-seasonal variations better than reflectance, particularly during the growing season (Figure 2.25f). Yet reflectance decompositions and VIs were less sensitive to such day-to-day variations (Figure 2.6, Figure 2.23).

There was also some variability between reflectance-based methods and relative SIF during the transition periods between the growing season and dormancy. We focused on the growing season onset since the reflectance measurements were not available during the cessation period. The onset (DOY 60 to 166) described by all the methods mentioned above as well as the relative SIF are compared in Figure 2.9, using a sigmoid fit to available data (Figure 2.16). The observed GPP_{max} had the most rapid yet latest growing onset. The methods and VIs derived from or related to the pigment contents increased earlier than GPP_{max} — such as the ICA component, PLSR coefficient, PROSAIL $\frac{C_{chl}}{C_{car}}$, and CCI. However, they built up slowly to reach the maximum, which suggests that reduction of the carotenoid content is a slower process than the recovery of LUE. Reflectance-based VIs (Figure 2.5) and decomposing methods (Figure 2.4 and 2.8(b,c)) had a slower growing season onset than GPP_{max}, as found in Bowling et al. (2018) as well. On the other hand, relative SIF started the onset at almost the same time as the GPP_{max}, and it quickly reached the maximum. Therefore, using both SIF and reflectance to constrain the LUE prediction (vander Tol et al., 2014) can further improve the prediction accuracy.

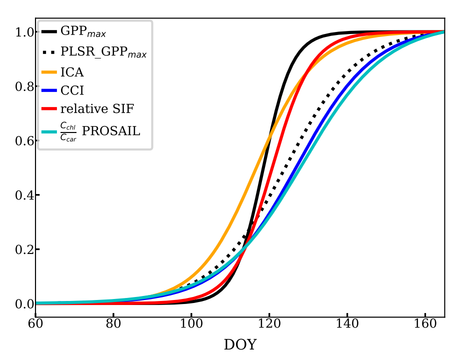

Figure 2.9: Temporal evolution of the growing season onset using sigmoid fits (scaled) of PLSR, ICA, CCI, chlorophyll to carotenoid ratio and relative SIF.

2.5 Conclusion and future work

In this study, we analyzed seasonal co-variation of GPP and the spectrally resolved visible and near infrared reflectance signal, as well as several commonly used VIs. The main spectral feature centered around 530 nm is most important for inferring the seasonal cycle of reflectance (400 – 900 nm) and LUE, which corresponds to changes in carotenoid content. This explains why CCI, PRI, and GCC track GPP seasonality so well, as most variations are driven by carotenoid pool changes. Our analysis included RTM simulation and in-situ pigment measurements throughout the season, confirming the link between reflectance/VIs and pigment contents. The comparison of reflectance/VIs and relative SIF reveals differences in the timing of the growing season onset, pigment changes and SIF, indicating the potential of using both reflectance and SIF to track the seasonality of photosynthesis. However, the close correspondence between both SIF and reflectance suggest that hyperspectral reflectance alone provides mechanistic evidence for a robust approach to track photosynthetic phenology of evergreen systems. Because seasonal variation in pigment concentration plays a strong role in regulating the seasonality of photosynthesis in evergreen systems, our work will help to inform future studies using hyperspectral reflectance to achieve accurate monitoring of these ecosystems. While indices like PRI and CCI are performing sufficiently as our methods which uses the full spectrum analysis at the canopy scale, the application of the full spectrum might be more robust for space-based measurements. In addition, we found seasonal changes of canopy reflectance near the red-edge region, which could be related to leaf structural changes or chlorophyll-a and b changes. Our PLSR coefficients are good references for customizing VIs to infer the photosynthetic seasonality in evergreen forest when there are restrictions to use the specific bands from currently existing VIs (such as PRI and CCI). While our current study is limited to a subalpine evergreen forest and canopy-scale measurements, applications to other regions, vegetation types, and observational platforms will be a focus for future research.

2.6 Appendix

Appendix A. Bi-directional reflectance effect

Appendix A1. NDVI and NIRv

The impact of geometry and small FOV are relatively negligible. First, our method only used the scans when FOV is on the needles by setting a NDVI threshold. Second, we plotted the NDVI and NIRv against the solar geometry at each individual tree targets throughout a year. NDVI/NIRv are quite homogeneous regardless of various solar geometries as shown in the following figures.

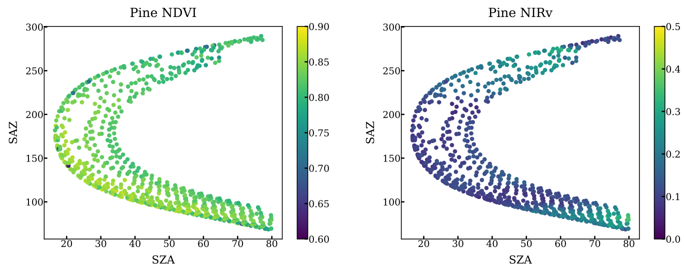

Figure 2.10: NDVI and NIRv of all scans targeting on a pine at different solar azimuth angles and solar zenith angles throughout a year.

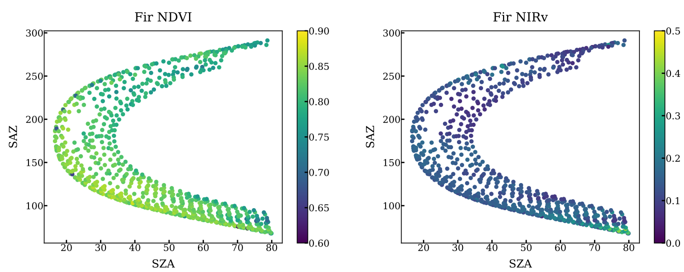

Figure 2.11: NDVI and NIRv of all scans targeting on a fir at different solar azimuth angles and solar zenith angles throughout a year.

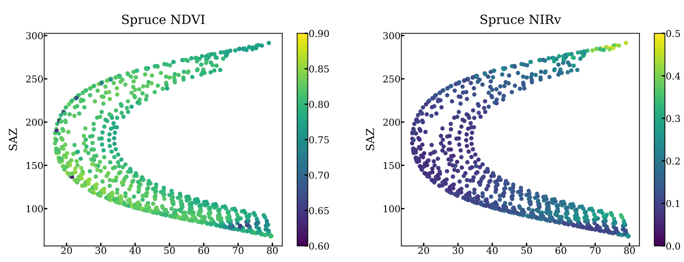

Figure 2.12: NDVI and NIRv of all scans targeting on a spruce at different solar azimuth angles and solar zenith angles throughout a year.

Appendix A2. PLSR on phase angle and reflectance

We did a PLSR analysis on individual measurements of phase angle and reflectance for 3 summer days (2017-7-1 to 2017-7-3). The results are the same from other sample days. Indeed, the reflectance has different sensitivities to the phase angle. However, the poor correlation of PLSR reconstructed phase angle and the measured one suggests the variations in phase angle should not be the critical factor for the change in reflectance. In our study, we primarily removed the bi-directional impact by averaging all the individual reflectance that was measured at different solar geometry and viewing geometry.

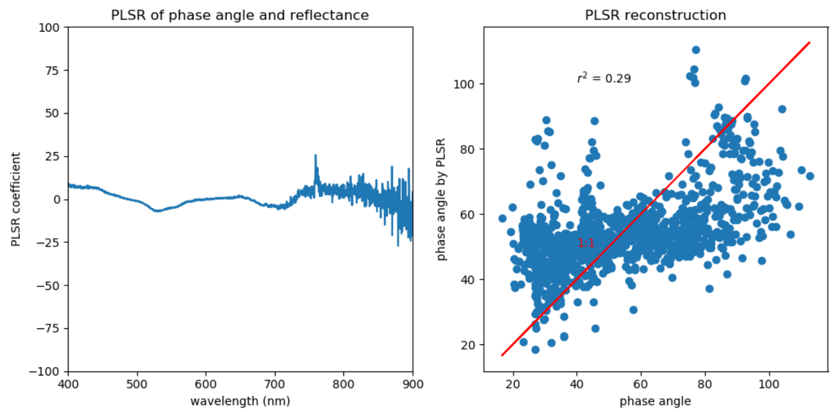

Figure 2.13: PLSR analysis on phase angle and reflectance.

Appendix B. Detailed processes on integrating daily-averaged canopy reflectance

First, we chose scans targeting vegetation only by requiring an NDVI greater than 0.6. Second, it is important to ensure that the solar irradiation did not change between the acquisition of the solar irradiance and the reflected radiance measurement. To achieve this, we matched the timestamps of a PAR sensor (LI-COR LI-190SA, LI-COR Environmental, Lincoln, Nebraska, US) to the timestamps of PhotoSpec, and compared the PAR value from the PAR sensor during the PhotoSpec irradiance acquisition with PAR during the actual target scan of the reflected radiance from vegetation. We only used the scans when the ratio of the two was 1.0±0.1, ensuring stable PAR conditions. Third, in order to avoid unstable PAR because of clouds (Dye, 2004), we also removed cloudy scenes by requiring PAR to be at least 60% of a theoretical maximum driven by solar geometry (Figure 2.14). Further, only data when PAR was greater than 100 μmol $m^{-2}s^{-1}$ were considered to eliminate the impact of low solar angles on reflectance data. The VIs shown in Figure 2.5 were extracted in the same fashion as above.

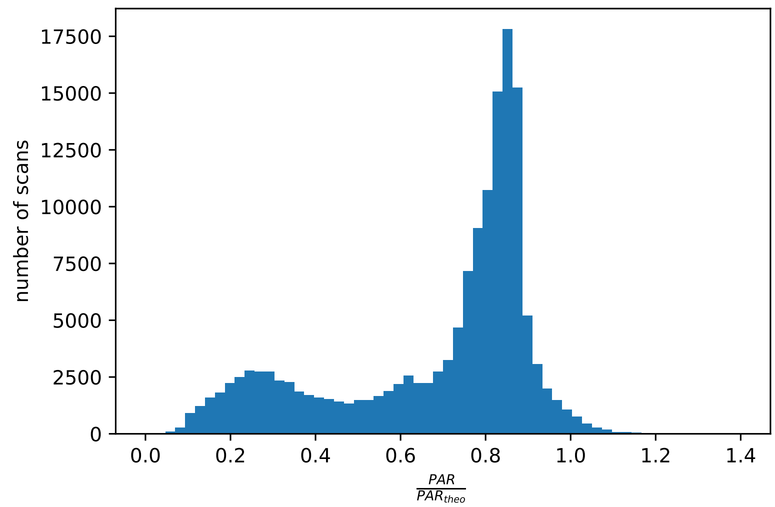

Figure 2.14: The distribution of ratio the measured PAR to the PAR at theoretical maximum from all individual scans.

Appendix C. PROSAIL fits

We used the following range constraints for variables included in the state vector of PROSAIL inversion:

- Leaf mesophyll structure (N): 0.9–1.1
- Chlorophyll content (C_{chl}): 0–120 μmol cm^{-2}
- Carotenoid content(C_{car}): 0–70 μmol cm^{-2}
- Anthocyanin content(C_{ant}): 0–10 μmol cm^{-2}
- Brown pigments(C_{brown}): 0–0.6
- Water content (C_w): 0–0.2 cm
- Dry matter content (C_m): 0–0.2 g cm^{-2}
- Xanthophyll cycle status (C_x) 0–1
- Leaf area index (LAI): fixed to 4.2

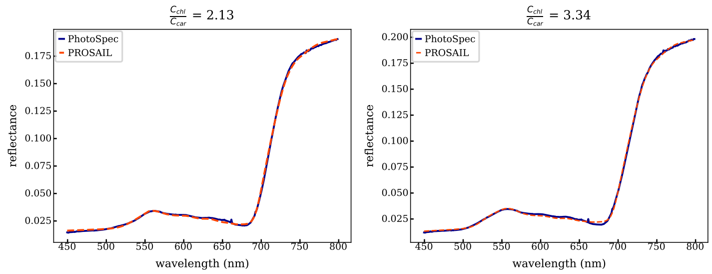

Figure 2.15: The observed and fitted reflectance spectra at low (left) and high (right) $\frac{C_{chl}}{C_{car}}$

Appendix D. Sigmoid fit

The sigmoid equation is:

$$y = b + \frac{a-b}{1+exp(\frac{d-x}{c})}$$

In this form, a and b represent the maximum and minimum values of the sigmoid fit. And d is the half maximum of the fit. We obtained the optimal values of these parameters.

Proof:

If $x \longrightarrow +\infty$, $exp(\frac{d-x}{c}) \longrightarrow 0$. So,

$$\lim_{x \longrightarrow +\infty} y = a$$

If $x \longrightarrow -\infty$, $exp(\frac{d-x}{c}) \longrightarrow +\infty$. So,

$$\lim_{x \longrightarrow -\infty} y = b$$

The first derivative of y is

$$\frac{dy}{dx} = \frac{a-b}{(1+exp(\frac{d-x}{c}))^2} exp(\frac{d-x}{c}) \frac{1}{c}$$

At the half maximum point (x = x_{half}), $y = \frac{a+b}{2}$. Therefore, we need to solve:

$$\frac{a+b}{2} = b + \frac{a-b}{1+exp(\frac{d-x_{half}}{c})}$$

Hence, x_{half} = d.

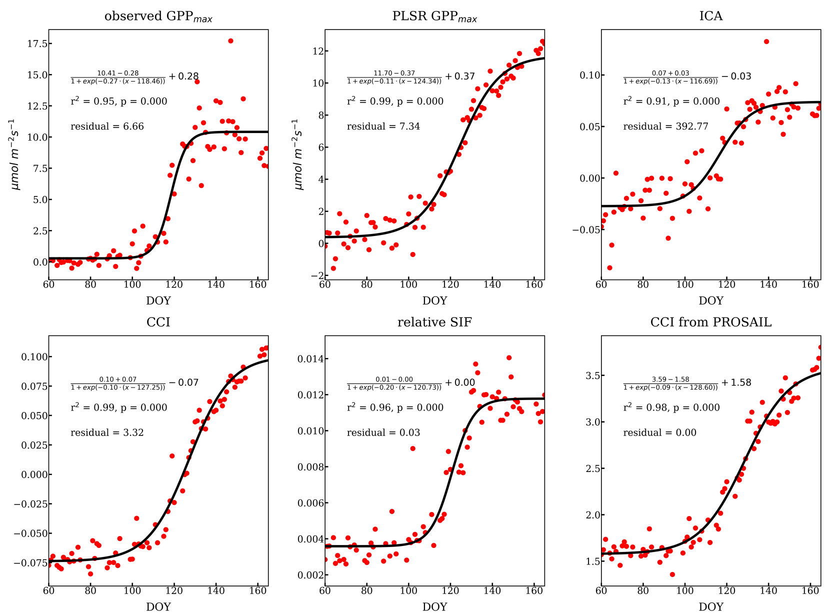

Figure 2.16: Individual sigmoid fits of the onset of growth from different methods and more VIs. The fitted curve has been expressed as the derivation as above. The pearson-r^2 and p values listed in each subplot were calculated from the correlation of observed and fitted variables. The residual was calculated as the average L2 norm of the difference between observed (y) and fitted variables ($\hat{y}$) normalized by the observation, i.e. $\frac{1}{n}\sum_i(\frac{y-\hat{y}}{y})^2$. The fittings are overall good. Because the ICA loading lacks a clear sigmoid shape, ICA has a larger residual.

2.7 Supplement

S1. GCC convolution functions

S2. Three regimes of LUE

S2.1. APAR measurement

Seven pairs of up and down-looking PAR sensors (SQ-500-SS; Apogee Instruments, Utah, US) above and below the canopy was used to calculate fPAR in half-hourly intervals. One pair of sensors was installed above the canopy on the same tower where PhotoSpec is located (measuring incoming PAR and reflected PAR). The other six pairs of sensors were installed below the canopy (measuring reflected and transmitted par). The derivation of APAR is shown in the following graph. fPAR was smoothed with an 8-point (4 hour) running mean and 20-day running mean to remove the noise in the measurements. The first fPAR measurement started on 8 Aug 2017 (DOY 220).

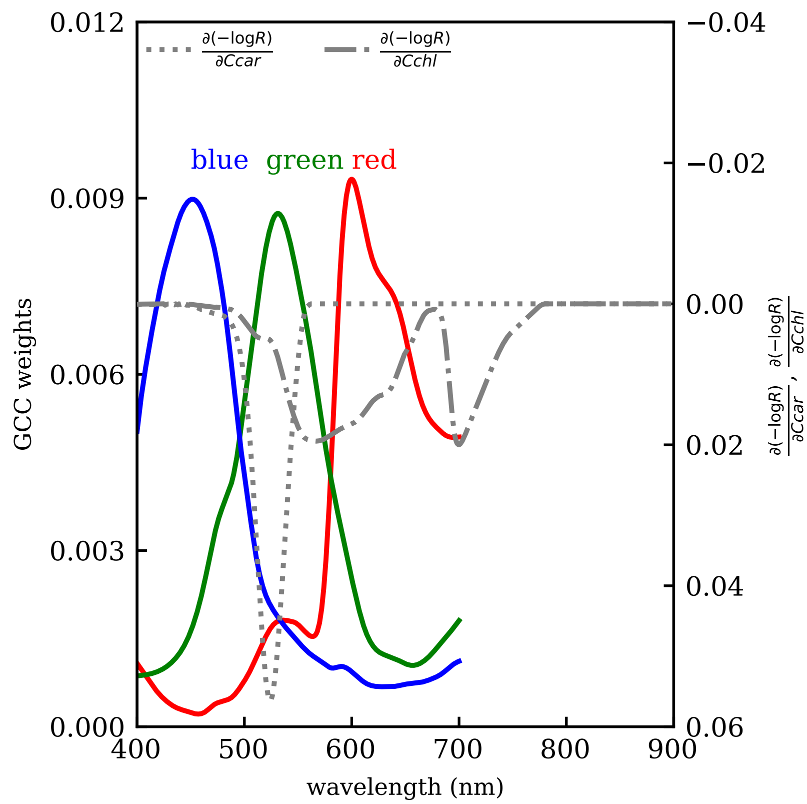

Figure 2.17: The convolution function of RGB channels used in GCC (Sonnentag et al., 2012) is overlaid with the chlorophyll Jacobian ($\frac{\partial - log(R)}{\partial Cchl}$, dash-dotted) and the carotenoid Jacobian ($\frac{\partial - log(R)}{\partial Ccar}$, dotted

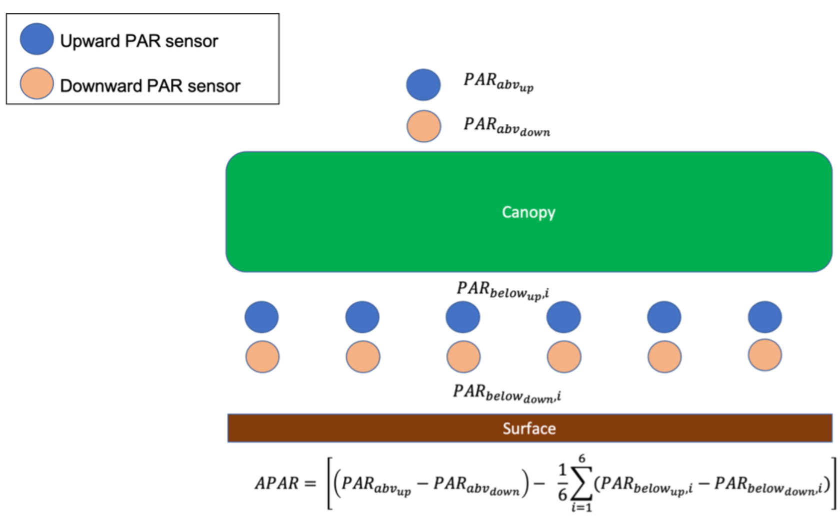

Figure 2.18: A demonstration for APAR calculation.

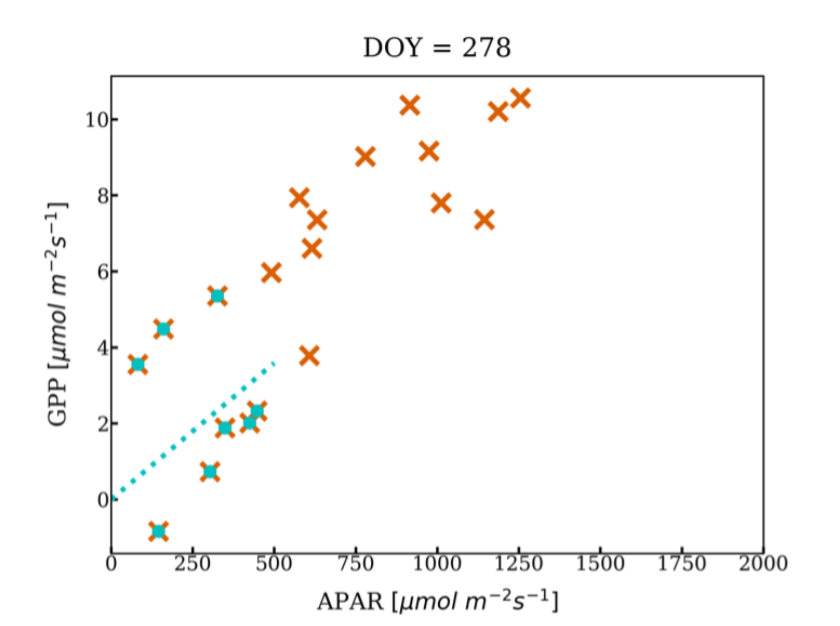

Figure 2.19: A demonstration of calculating $\mathrm{LUE}_{\mathrm{lightL}}$ and $\mathrm{LUE}_{\mathrm{total}}$.

S2.2. Light limited and daily averaged LUE

At low light intensity, photosynthesis is light limited. We followed the format of Equation (1) to define light-limited LUE ($\mathrm{LUE}_{\mathrm{lightL}}$) as the fitted slope of APAR against GPP at PAR between 100 and 500 μmol $m^{-2}s^{-1}$. We calculated $\mathrm{LUE}_{\mathrm{lightL}}$ from half-hourly GPP and APAR for each day. We also defined a more generalized effective daily LUE ($\mathrm{LUE}_{\mathrm{total}}$) as the daily averaged ratio of GPP to APAR during the day. This effective daily LUE would be most applicable for empirical LUE models that work on daily time-steps.

$\mathrm{LUE}_{\mathrm{lightL}}$ is the fitted slope of GPP and APAR when PAR is between 100-500 μmol $m^{-2}s^{-1}$. The fit was forced to go through the origin as the equation has no intercept.

$\mathrm{LUE}_{\mathrm{total}}$ is the daily average of $\frac{\mathrm{GPP}}{\mathrm{APAR}}$ during the day.

Here is a demonstration of how $\mathrm{LUE}_{\mathrm{lightL}}$ and $\mathrm{LUE}_{\mathrm{total}}$ were calculated. Given a day (DOY =278 as an example), we selected the GPP measurements when the PAR level is between 100-500 μmol $m^{-2}s^{-1}$. Then, we did a linear regression of those GPP measurements with their APAR levels (the cyan dots and dashed line). The slope of this regression is $\mathrm{LUE}_{\mathrm{lightL}}$. On the same day, all the GPP measurements that happened when the PAR level is above 100 μmol $m^{-2}s^{-1}$ are the orange crosses in the plot. We calculated the ratio of GPP and APAR of those orange points, and the daily mean of the ratio is the $\mathrm{LUE}_{\mathrm{total}}$.

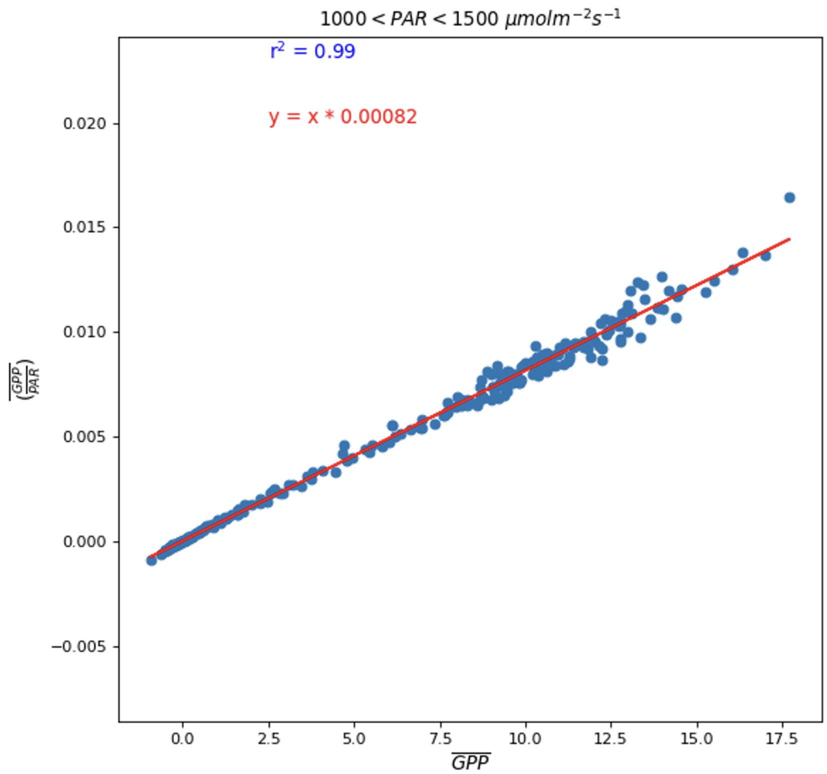

Figure 2.20: Normalized GPP_{max} and Unnormalized GPP_{max}.

S2.3. Two ways calculating GPP_{max}

There were only a few days when PAR is so low that LUE did not reach light saturation for most of the day when LUE_{total} is more comparable to LUE_{lightL}. Also, there is a 26-day gap in APAR measurement at the beginning period of our study. Therefore, we only showed the results of GPP_{max} in the main text as it is more representative than LUE_{lightL} and more physiology-driven than LUE_{total}. Because of the missing APAR, we did not normalize GPP_{max} with APAR. However, the normalized GPP_{max} and unnormalized GPP_{max} are significantly linearly correlated (Figure 2.19). Although GPP normalized by PAR results in the correct unit of LUE, it is easily mistaken as fPAR has been considered. To avoid this confusion, we chose to use mean GPP at PAR between 1000 and 1500 μmol $m^{-2}s^{-1}$.

S2.4. Comparing the three regimes of LUE

Needles use light most efficiently at low light levels (LUE_{lightL}) for a fraction of the day. We started to observe a photosynthetic saturation at low PAR values ($\sim$ 500 μ mol $m^{-2}s^{-1}$; Figure 2), which is represented by GPP_{max}, resulting in low efficiencies under high light conditions. LUE_{total} represents the mean light use

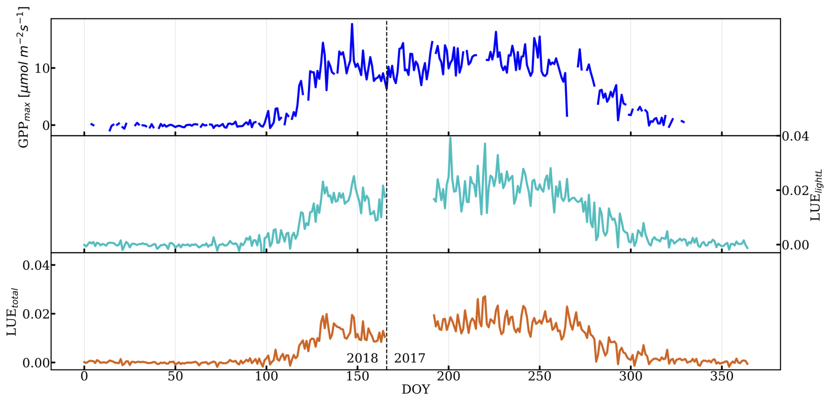

Figure 2.21: Time series of GPP_{max}, LUE_{lightL} and LUE_{total}. DOY 166 (2017) is the first day of observation. The vertical dashed line divides the observations from Day of Year (DOY) for year 2017 and 2018.

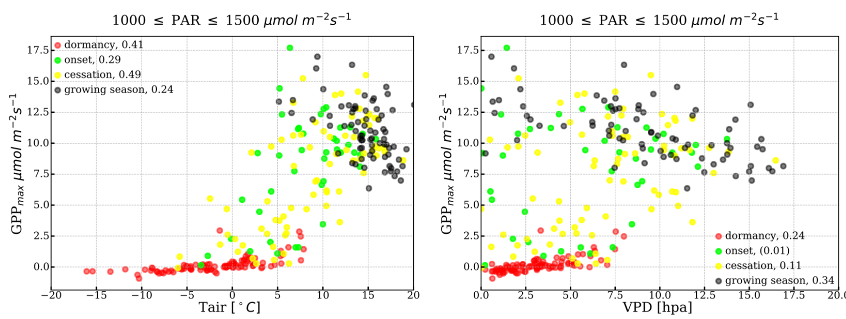

Figure 2.22: Scatter plots of GPP_{max} against Tair (top left) and VPD (top right). The definition of seasons follows the same convention as in Figure 1. The onset is the transitioning period from dormancy to the growing season. The cessation is the transitioning period from the growing season to the dormancy. The Pearson-r^2 values are shown in the legend. The statistically insignificant value is in parentheses if the p-value is greater than 0.005.

scheme throughout the day. Hence, LUE_{lightL} was slightly higher than LUE_{total} during most of the growing season (Figure 2.20).

S3. GPP_{max} and PRI as a function of Tair and VPD in different seasons

The correlations with Tair and VPD are similar because Tair and VPD are significantly correlated.

S4. ICA algorithm

We used the fastICA algorithm from scikit-learn v0.21.0 (`https://scikit-learn.org/stable/modules/generated/sklearn.decomposition.FastICA.html`). Because ICA minimizes the dependencies of the second-order moment (variance)

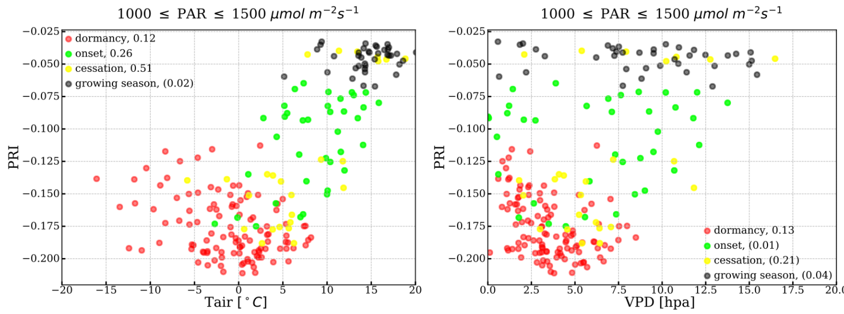

Figure 2.23: Scatter plots of PRI against Tair (left) and VPD (right). The definition of seasons follows the same convention as in Figure (1) and S3a. The onset is the transitioning period from dormancy to the growing season. The cessation is the transitioning period from the growing season to the dormancy. The Pearson-r^2 values are shown in the legend. The statistically insignificant value is in parentheses if the p-value is greater than 0.005.

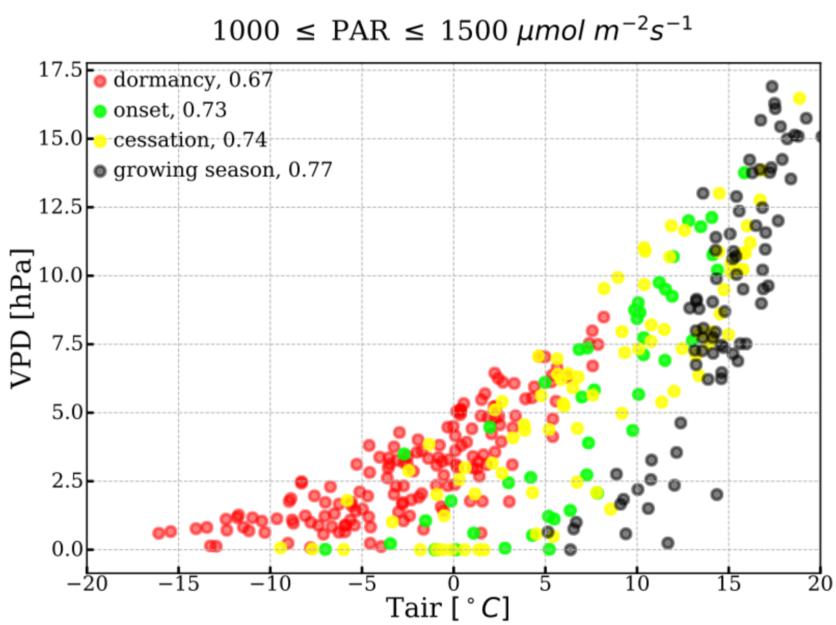

Figure 2.24: Scatter plot of VPD and Tair. The definition of seasons follows the same convention as in Figure (1) and 2.22. The Pearson-r^2 values are shown in the legend. The statistically insignificant values are in parentheses if the p-value is greater than 0.005.

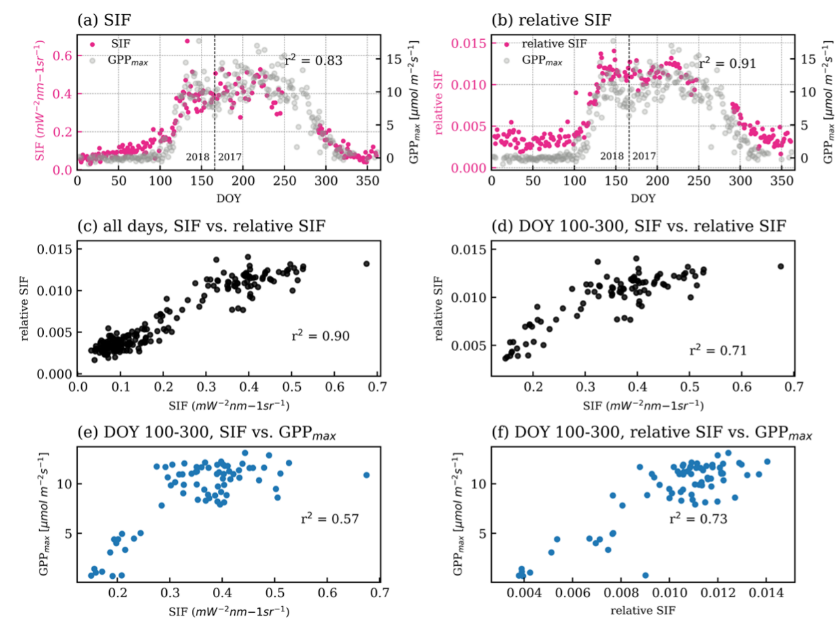

Figure 2.25: Comparison between SIF and relative SIF, and the correlation of them with GPP_{max} during the growing season.

and higher, the randomness during the minimization makes the explained variance and order of individual components unclear. In our calculation, the ICA algorithm reduced the dimension of the input matrix by eigenvalue decomposition first, from which the first three second-order independent/orthogonal components yielded 99.99% of the variance. Then, the algorithm extracted the independent components of high-order moments from these orthogonal components.

S5. SIF vs relative SIF

Relative SIF is SIF normalized by the reflected near-infrared radiance at 755nm. This normalization will make SIF more comparable to a 'SIF yield', as it is a ratio effectively correcting for incoming irradiance, and sunlit/shaded fraction. The attached plot is similar as we did in Figure 5d but with SIF and relative SIF. The seasonal cycles of relative SIF and SIF are well correlated. Relative SIF is more correlated with the GPP_{max} in seasonal variations. However, the sub-seasonal change in the growing season is captured more by relative SIF.

S6. PLSR analysis

Based on four-fold cross-validations, we set n_components = 4 in the analysis of GPP_{max} and 2 in the analysis of pigment measurements. All the PLSR coefficients are similar (Figure 4) because LUE_{lightL}, LUE_{total}, and GPP_{max} are similar in terms

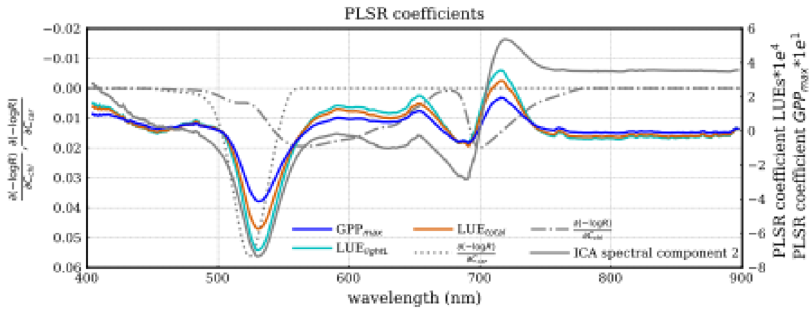

Figure 2.26: PLSR coefficients of reflectance with GPP_{max}, LUE_{lightL}, and LUE_{total}. The overlaid dash-dotted and dotted lines are chlorophyll and carotenoid Jacobians, respectively. The overlaid solid grey line is the second ICA spectral component. The vertical dashed line divides the observations from DOY for year 2017 and 2018.

of the seasonal trend.

2.8 Code and data availability

Our data presented in this paper are provided at `https://data.caltech.edu/records/1597` and `https://data.caltech.edu/records/1231`. The PROSAIL model in the Julia programming language used in our study can be obtained from `https://github.com/climate-machine/LSM-SPAM`.

2.9 Acknowledgements

We thank the sponsors from the Caltech Graduate First-year Fellowship, NASA Carbon Monitoring Systems program (Award NNX16AP33G) to D. R. Bowling. The US-NR1 AmeriFlux site has been supported by the U.S. DOE, Office of Science through the AmeriFlux Management Project (AMP) at Lawrence Berkeley National Laboratory under Award Number 7094866. The National Center for Atmospheric Research (NCAR) is sponsored by NSF.

Bibliography

W. W. Adams and B. Demmig-Adams. Carotenoid composition and down regulation of photosystem II in three conifer species during the winter. *Physiologia Plantarum*, 92(3):451–458, nov 1994. ISSN 0031-9317. doi: 10.1111/j.1399-3054.1994.tb08835.x. URL `http://doi.wiley.com/10.1111/j.1399-3054.1994.tb08835.x`.

A. Ahlström, G. Schurgers, A. Arneth, and B. Smith. Robustness and uncertainty in terrestrial ecosystem carbon response to CMIP5 climate change projections. *Environmental Research Letters*, 7(4):044008, dec 2012. ISSN 1748-9326. doi: 10.

1088/1748-9326/7/4/044008. URL http://stacks.iop.org/1748-9326/7/i=4/a=044008?key=crossref.c334ef142bc600447b618d3813e5e3ce.

A. M. Ali, R. Darvishzadeh, A. K. Skidmore, I. van Duren, U. Heiden, and M. Heurich. Estimating leaf functional traits by inversion of prospect: Assessing leaf dry matter content and specific leaf area in mixed mountainous forest. *International journal of applied earth observation and geoinformation*, 45:66–76, 2016.

G. P. Asner, R. E. Martin, D. E. Knapp, R. Tupayachi, C. Anderson, L. Carranza, P. Martinez, M. Houcheime, F. Sinca, and P. Weiss. Spectroscopy of canopy chemicals in humid tropical forests. *Remote Sensing of Environment*, 115(12):3587–3598, dec 2011. ISSN 0034-4257. doi: 10.1016/J.RSE.2011.08.020. URL https://www.sciencedirect.com/science/article/pii/S0034425711003245?via{\%}3Dihub.

G. Badgley, C. B. Field, and J. A. Berry. Canopy near-infrared reflectance and terrestrial photosynthesis. *Science Advances*, 3(3):e1602244, mar 2017. ISSN 2375-2548. doi: 10.1126/sciadv.1602244. URL http://advances.sciencemag.org/lookup/doi/10.1126/sciadv.1602244.

D. Baldocchi, E. Falge, L. Gu, R. Olson, D. Hollinger, S. Running, P. Anthoni, C. Bernhofer, K. Davis, R. Evans, et al. Fluxnet: A new tool to study the temporal and spatial variability of ecosystem-scale carbon dioxide, water vapor, and energy flux densities. *Bulletin of the American Meteorological Society*, 82 (11):2415–2434, 2001.

M. L. Barnes, D. D. Breshears, D. J. Law, W. J. D. van Leeuwen, R. K. Monson, A. C. Fojtik, G. A. Barron-Gafford, and D. J. P. Moore. Beyond greenness: Detecting temporal changes in photosynthetic capacity with hyperspectral reflectance data. *PLOS ONE*, 12(12):e0189539, dec 2017. ISSN 1932-6203. doi: 10.1371/journal.pone.0189539. URL https://dx.plos.org/10.1371/journal.pone.0189539.

P. D. Blanken, R. K. Monson, S. P. Burns, D. R. Bowling, and A. A. Turnipseed. Data and information for the AmeriFlux US-NR1 Niwot Ridge Subalpine Forest (LTER NWT1) Site. *AmeriFlux Management Project, Berkeley, CA: Lawrence Berkeley National Laboratory.*, 2019. doi: r/10.17190/AMF/1246088.

D. R. Bowling and B. A. Logan. Carbon Monitoring System (CMS)Conifer Needle Pigment Composition, Niwot Ridge, Colorado, USA, 2017-2018. page 0.021358 MB, 2019. doi: 10.3334/ORNLDAAC/1723. URL https://daac.ornl.gov/cgi-bin/dsviewer.pl?ds_id=1723.

D. R. Bowling, B. A. Logan, K. Hufkens, D. M. Aubrecht, A. D. Richardson, S. P. Burns, W. R.L. Anderegg, P. D. Blanken, and D. P. Eiriksson. Limitations to winter and spring photosynthesis of a Rocky Mountain subalpine forest. *Agricultural and Forest Meteorology*, 252:241–255, apr 2018. ISSN 0168-1923. doi:

10.1016/J.AGRFORMET.2018.01.025. URL https://www.sciencedirect.com/science/article/pii/S016819231830025X?via{\%}3Dihub.

S. P. Burns, P. D. Blanken, A. A. Turnipseed, J. Hu, and R. K. Monson. The influence of warm-season precipitation on the diel cycle of the surface energy balance and carbon dioxide at a Colorado subalpine forest site. *Biogeosciences*, 12:7349–7377, 2015. doi: 10.5194/bg-12-7349-2015. URL www.biogeosciences.net/12/7349/2015/.

S. P. Burns, G. D. Maclean, P. D. Blanken, S. P. Oncley, S. R. Semmer, and R. K. Monson. The Niwot Ridge Subalpine Forest US-NR1 AmeriFlux site - Part 1: Data acquisition and site record-keeping. *Geoscientific Instrumentation, Methods and Data Systems*, 5(2):451–471, sep 2016. ISSN 2193-0864. doi: 10.5194/gi-5-451-2016. URL https://www.geosci-instrum-method-data-syst.net/5/451/2016/.

P. Ciais, C. Sabine, G. Bala, L. Bopp, V. Brovkin, J. Canadell, R. Chhabra, R. DeFries, J. Galloway, M. Heimann, C. Jones, C. Le Quéré, R. B. Myneni, S. Piao, and P. Thornton. Carbon and Other Biogeochemical Cycles. In T. F. Stock, D. Qin, G.-K. Plattner, M. Tignor, S. K. Allen, J. Boschung, A. Nauels, Y. Xia, V. Bex, and P. M. Midgley, editors, *Climate Change 2013: The Physical Science Basis. Contribution of Working Group I to the Fifth Assessment Report of the Intergovernmental Panel on Climate Change*, chapter 6, pages 465–570. Cambridge University Press, Cambridge, United Kingdom and New York, NY, USA, 2013. doi: 10.1017/CBO9781107415324.015.

P. Comon. Independent component analysis, a new concept? *Signal processing*, 36 (3):287–314, 1994.

T. P. Dawson, P. J. Curran, and S. E. Plummer. Liberty—modeling the effects of leaf biochemical concentration on reflectance spectra. *Remote sensing of environment*, 65(1):50–60, 1998.

S. de Tomás Marín, M. Novák, K. Klančnik, and A. Gaberščik. Spectral signatures of conifer needles mainly depend on their physical traits. *Polish Journal of Ecology*, 64(1):1–14, 2016.

B. Dechant, M. Cuntz, M. Vohland, E. Schulz, and D. Doktor. Estimation of photosynthesis traits from leaf reflectance spectra: correlation to nitrogen content as the dominant mechanism. *Remote sensing of environment*, 196:279–292, 2017.

B. Dechant, Y. Ryu, and M. Kang. Making full use of hyperspectral data for gross primary productivity estimation with multivariate regression: Mechanistic insights from observations and process-based simulations. *Remote Sensing of Environment*, 234:111435, 2019.

B. Demmig-Adams and W. W. Adams. The role of xanthophyll cycle carotenoids in the protection of photosynthesis. *Trends in Plant Science*, 1(1):21–26, jan 1996. ISSN 1360-1385. doi: 10.1016/S1360-1385(96)80019-7. URL https://www.sciencedirect.com/science/article/pii/S1360138596800197?via{\%}3Dihub.

S. DuBois, A. R. Desai, A. Singh, S. P. Serbin, M. L. Goulden, D. D. Baldocchi, S. Ma, W. C. Oechel, S. Wharton, E. L. Kruger, et al. Using imaging spectroscopy to detect variation in terrestrial ecosystem productivity across a water-stressed landscape. *Ecological applications*, 28(5):1313–1324, 2018.

D. Dutta, D. S. Schimel, Y. Sun, C. van der Tol, and C. Frankenberg. Optimal inverse estimation of ecosystem parameters from observations of carbon and energy fluxes. *Biogeosciences*, 16(1):77–103, 2019. doi: 10.5194/bg-16-77-2019. URL https://www.biogeosciences.net/16/77/2019/.

D. G. Dye. Spectral composition and quanta-to-energy ratio of diffuse photosynthetically active radiation under diverse cloud conditions. *Journal of Geophysical Research*, 109(D10):D10203, may 2004. ISSN 0148-0227. doi: 10.1029/2003JD004251. URL http://doi.wiley.com/10.1029/2003JD004251.

G. D. Farquhar, S. von Caemmerer, and J. A. Berry. A biochemical model of photosynthetic CO2 assimilation in leaves of C3 species. *Planta*, 149(1):78–90, jun 1980. ISSN 0032-0935. doi: 10.1007/BF00386231. URL http://www.ncbi.nlm.nih.gov/pubmed/24306196http://link.springer.com/10.1007/BF00386231.

J. B. Feret, C. François, G. P. Asner, A. A. Gitelson, R. E. Martin, L. P. R. Bidel, S. L. Ustin, G. le Maire, and S. Jacquemoud. PROSPECT-4 and 5: Advances in the leaf optical properties model separating photosynthetic pigments. *Remote Sensing of Environment*, 112(6):3030–3043, jun 2008. ISSN 0034-4257. doi: 10.1016/J.RSE.2008.02.012. URL https://www.sciencedirect.com/science/article/pii/S0034425708000813?via{\%}3Dihub.

J. B. Féret, A. A. Gitelson, S. D. Noble, and S. Jacquemoud. PROSPECT-D: Towards modeling leaf optical properties through a complete lifecycle. *Remote Sensing of Environment*, 193:204–215, 2017. ISSN 00344257. doi: 10.1016/j.rse.2017.03.004. URL http://dx.doi.org/10.1016/j.rse.2017.03.004.

J. B. Féret, G. Le Maire, S. Jay, D. Berveiller, R. Bendoula, G. Hmimina, A. Cheraiet, J. C. Oliveira, F. J. Ponzoni, T. Solanki, et al. Estimating leaf mass per area and equivalent water thickness based on leaf optical properties: Potential and limitations of physical modeling and machine learning. *Remote Sensing of Environment*, 231:110959, 2019.

J. A. Gamon, J. Peñuelas, and C. B. Field. A narrow-waveband spectral index that tracks diurnal changes in photosynthetic efficiency. *Remote Sensing of Environment*, 41(1):35–44, jul 1992. ISSN 0034-4257. doi: 10.1016/0034-4257(92)90059-S. URL https://www.sciencedirect.com/science/article/pii/003442579290059S.

J. A. Gamon, L. Serrano, and J. S. Surfus. The photochemical reflectance index: an optical indicator of photosynthetic radiation use efficiency across species, functional types, and nutrient levels. *Oecologia*, 112(4):492–501, nov 1997. ISSN 0029-8549. doi: 10.1007/s004420050337. URL `http://link.springer.com/10.1007/s004420050337`.

J. A. Gamon, A. F. Rahman, J. L. Dungan, M. Schildhauer, and K. F. Huemmrich. Spectral Network (SpecNet)—What is it and why do we need it? *Remote Sensing of Environment*, 103(3):227–235, aug 2006. ISSN 0034-4257. doi: 10.1016/J.RSE.2006.04.003. URL `https://www.sciencedirect.com/science/article/pii/S0034425706001301`.

J. A. Gamon, K. F. Huemmrich, C. Y. S. Wong, I. Ensminger, S. Garrity, D. Y. Hollinger, A. Noormets, and J. Peñuelas. A remotely sensed pigment index reveals photosynthetic phenology in evergreen conifers. *Proceedings of the National Academy of Sciences of the United States of America*, 113(46): 13087–13092, nov 2016. ISSN 1091-6490. doi: 10.1073/pnas.1606162113. URL `http://www.ncbi.nlm.nih.gov/pubmed/27803333http://www.pubmedcentral.nih.gov/articlerender.fcgi?artid=PMC5135292`.

M. F. Garbulsky, J. Peñuelas, J. Gamon, Y. Inoue, and I. Filella. The photochemical reflectance index (pri) and the remote sensing of leaf, canopy and ecosystem radiation use efficiencies: A review and meta-analysis. *Remote sensing of environment*, 115(2):281–297, 2011.

P. Geladi and B. R. Kowalski. Partial least-squares regression: a tutorial. *Analytica Chimica Acta*, 185:1–17, jan 1986. ISSN 0003-2670. doi: 10.1016/0003-2670(86)80028-9. URL `https://www.sciencedirect.com/science/article/pii/0003267086800289?via{\%}3Dihub`.

P. Gentine and S. H. Alemohammad. Reconstructed Solar-Induced Fluorescence: A Machine Learning Vegetation Product Based on MODIS Surface Reflectance to Reproduce GOME-2 Solar-Induced Fluorescence. *Geophysical Research Letters*, 45(7):3136–3146, 2018. ISSN 19448007. doi: 10.1002/2017GL076294.

B. Genty, J. M. Briantais, and N. R. Baker. The relationship between the quantum yield of photosynthetic electron transport and quenching of chlorophyll fluorescence. *Biochimica et Biophysica Acta (BBA)-General Subjects*, 990(1):87–92, 1989.

E. Glenn, A. Huete, P. Nagler, and S. Nelson. Relationship Between Remotely-sensed Vegetation Indices, Canopy Attributes and Plant Physiological Processes: What Vegetation Indices Can and Cannot Tell Us About the Landscape. *Sensors*, 8(4):2136–2160, mar 2008. ISSN 1424-8220. doi: 10.3390/s8042136. URL `http://www.mdpi.com/1424-8220/8/4/2136`.

K. S. Gould. Nature's swiss army knife: the diverse protective roles of anthocyanins in leaves. *BioMed Research International*, 2004(5):314–320, 2004.

M. L. Goulden, J. W. Munger, S. Fan, B. C. Daube, and C. S. Wofsy. Measurements of carbon sequestration by long-term eddy covariance: methods and a critical evaluation of accuracy. *Global Change Biology*, 2(3):169–182, jun 1996. ISSN 1354-1013. doi: 10.1111/j.1365-2486.1996.tb00070.x. URL `http://doi.wiley.com/10.1111/j.1365-2486.1996.tb00070.x`.

K. Grossmann, C. Frankenberg, T. S. Magney, S. C. Hurlock, U. Seibt, and J. Stutz. PhotoSpec: A new instrument to measure spatially distributed red and far-red Solar-Induced Chlorophyll Fluorescence. *Remote Sensing of Environment*, 216:311–327, oct 2018. ISSN 0034-4257. doi: 10.1016/J.RSE.2018.07.002. URL `https://www.sciencedirect.com/science/article/pii/S0034425718303298?via{\%}3Dihub`.

L. Guanter, Y. Zhang, M. Jung, J. Joiner, M. Voigt, J. A. Berry, C. Frankenberg, A. R. Huete, P. Zarco-Tejada, J. Lee, et al. Global and time-resolved monitoring of crop photosynthesis with chlorophyll fluorescence. *Proceedings of the National Academy of Sciences*, 111(14):E1327–E1333, 2014.

F. G. Hall, T. Hilker, N. C. Coops, A. Lyapustin, K. F. Huemmrich, E. Middleton, H. Margolis, G. Drolet, and T. A. Black. Multi-angle remote sensing of forest light use efficiency by observing PRI variation with canopy shadow fraction. *Remote Sensing of Environment*, 112(7):3201–3211, jul 2008. ISSN 0034-4257. doi: 10.1016/J.RSE.2008.03.015. URL `https://www.sciencedirect.com/science/article/pii/S0034425708001144`.

J. Harbinson. Modeling the protection of photosynthesis. *Proceedings of the National Academy of Sciences of the United States of America*, 109(39):15533–4, sep 2012. ISSN 1091-6490. doi: 10.1073/pnas.1213195109. URL `http://www.ncbi.nlm.nih.gov/pubmed/22991475http://www.pubmedcentral.nih.gov/articlerender.fcgi?artid=PMC3465449`.

T. Hilker, N. C. Coops, F. G. Hall, C. J. Nichol, A. Lyapustin, T. A. Black, M. A. Wulder, R. Leuning, A. Barr, D. Y. Hollinger, B. Munger, and C. J. Tucker. Inferring terrestrial photosynthetic light use efficiency of temperate ecosystems from space. *Journal of Geophysical Research*, 116(G3):G03014, jul 2011a. ISSN 0148-0227. doi: 10.1029/2011JG001692. URL `http://doi.wiley.com/10.1029/2011JG001692`.

T. Hilker, A. Gitelson, N. C. Coops, F. G. Hall, and T. A. Black. Tracking plant physiological properties from multi-angular tower-based remote sensing. *Oecologia*, 165(4):865–876, apr 2011b. ISSN 0029-8549. doi: 10.1007/s00442-010-1901-0. URL `http://link.springer.com/10.1007/s00442-010-1901-0`.

D. N. H. Horler, M. Dockray, and J. Barber. The red edge of plant leaf reflectance. *International Journal of Remote Sensing*, 4(2):273–288, jan 1983. ISSN 0143-1161. doi: 10.1080/01431168308948546. URL `https://www.tandfonline.com/doi/full/10.1080/01431168308948546`.

K. F. Huemmrich, P. K. E. Campbell, B. Gao, L. B. Flanagan, and M. Goulden. ISS as a Platform for Optical Remote Sensing of Ecosystem Carbon Fluxes: A Case Study Using HICO. *IEEE Journal of Selected Topics in Applied Earth Observations and Remote Sensing*, 10(10):4360–4375, oct 2017. ISSN 1939-1404. doi: 10.1109/JSTARS.2017.2725825. URL `http://ieeexplore.ieee.org/document/8051041/`.

K. F Huemmrich, P. Campbell, D. Landis, and E. Middleton. Developing a common globally applicable method for optical remote sensing of ecosystem light use efficiency. *Remote Sensing of Environment*, 230:111190, 2019.

A. R. Huete, H. Q. Liu, K. V. Batchily, and W. J. D. A Van Leeuwen. A comparison of vegetation indices over a global set of tm images for eos-modis. *Remote sensing of environment*, 59(3):440–451, 1997.

N. M. Hughes. Winter leaf reddening in 'evergreen'species. *New Phytologist*, 190 (3):573–581, 2011.

A. Hyvärinen and E. Oja. Independent component analysis: algorithms and applications. *Neural Networks*, 13(4-5):411–430, jun 2000. ISSN 0893-6080. doi: 10.1016/S0893-6080(00)00026-5. URL `https://www.sciencedirect.com/science/article/pii/S0893608000000265`.

S. Jacquemoud and F. Baret. Prospect: A model of leaf optical properties spectra. *Remote sensing of environment*, 34(2):75–91, 1990.

S. Jacquemoud, F. Baret, B. Andrieu, F. M. Danson, and K. Jaggard. Extraction of vegetation biophysical parameters by inversion of the PROSPECT + SAIL models on sugar beet canopy reflectance data. Application to TM and AVIRIS sensors. *Remote Sensing of Environment*, 52(3):163–172, jun 1995. ISSN 0034-4257. doi: 10.1016/0034-4257(95)00018-V. URL `https://www.sciencedirect.com/science/article/pii/003442579500018V`.

S. Jacquemoud, W. Verhoef, F. Baret, C. Bacour, P. J. Zarco-Tejada, G. P. Asner, C. François, and S. L. Ustin. Prospect+ sail models: A review of use for vegetation characterization. *Remote sensing of environment*, 113:S56–S66, 2009.

G. H. Krause and E. Weis. Chlorophyll fluorescence and photosynthesis: The basics. Technical report, 1991. URL `www.annualreviews.org`.

G. Krinner, N. Viovy, N. de Noblet-Ducoudré, J. Ogée, J. Polcher, P. Friedlingstein, P. Ciais, S. Sitch, and I. C. Prentice. A dynamic global vegetation model for studies of the coupled atmosphere-biosphere system. *Global Biogeochemical Cycles*, 19(1), mar 2005. ISSN 08866236. doi: 10.1029/2003GB002199. URL `http://doi.wiley.com/10.1029/2003GB002199`.

D. W. Lee and K. S. Gould. Why leaves turn red: pigments called anthocyanins probably protect leaves from light damage by direct shielding and by scavenging free radicals. *American Scientist*, 90(6):524–531, 2002.

R. Leuning. A critical appraisal of a combined stomatal-photosynthesis model for c3 plants. *Plant, Cell & Environment*, 18(4):339–355, 1995.

H. Q. Liu and A. Huete. A feedback based modification of the ndvi to minimize canopy background and atmospheric noise. *IEEE transactions on geoscience and remote sensing*, 33(2):457–465, 1995.

T. S. Magney, D. R. Bowling, B. A. Logan, K. Grossman, J. Stutz, P. Blanken, S. P. Burns, R. Cheng, M. A. Garcia, P. Köhler, S. Lopez, N. Parazoo, B. Raczka, D. Schimel, and C. Frankenberg. Mechanistic evidence for tracking the seasonality of photosynthesis with solar induced fluorescence. *Proceedings of the National Academy of Sciences of the United States of America.*, 2019. doi: 10.1073/pnas.1900278116. URL `https://www.pnas.org/lookup/doi/10.1073/pnas.1900278116`.

J. H. Matthes, S. H. Knox, C. Sturtevant, O. Sonnentag, J. Verfaillie, and D. Baldocchi. Predicting landscape-scale CO 2 flux at a pasture and rice paddy with long-term hyperspectral canopy reflectance measurements. *Biogeosciences*, 12:4577–4594, 2015. doi: 10.5194/bg-12-4577-2015. URL `www.biogeosciences.net/12/4577/2015/`.

K. Meacham-Hensold, C. M. Montes, J. Wu, K. Guan, P. Fu, E. A. Ainsworth, T. Pederson, C. E. Moore, K. L. Brown, C. Raines, and C. J. Bernacchi. High-throughput field phenotyping using hyperspectral reflectance and partial least squares regression (PLSR) reveals genetic modifications to photosynthetic capacity. *Remote Sensing of Environment*, page 111176, may 2019. ISSN 0034-4257. doi: 10.1016/J.RSE.2019.04.029. URL `https://www.sciencedirect.com/science/article/pii/S0034425719301804`.

E. M. Middleton, K. F. Huemmrich, D. R. Landis, T. A. Black, A. G. Barr, and J. H. McCaughey. Photosynthetic efficiency of northern forest ecosystems using a modis-derived photochemical reflectance index (pri). *Remote Sensing of Environment*, 187:345–366, 2016.

R. K. Monson, A. A. Turnipseed, J. P. Sparks, P. C. Harley, L. E. Scott-Denton, K. Sparks, and T. E. Huxman. Carbon sequestration in a high-elevation, subalpine forest. *Global Change Biology*, 8(5):459–478, may 2002. ISSN 1354-1013. doi: 10.1046/j.1365-2486.2002.00480.x. URL `http://doi.wiley.com/10.1046/j.1365-2486.2002.00480.x`.

R. K. Monson, J. P. Sparks, T. N. Rosenstiel, L. E. Scott-Denton, T. E. Huxman, P. C. Harley, A. A. Turnipseed, S. P. Burns, B. Backlund, and J. Hu. Climatic influences on net ecosystem co 2 exchange during the transition from wintertime carbon source to springtime carbon sink in a high-elevation, subalpine forest. *Oecologia*, 146(1):130–147, 2005.

J. L. Monteith. Solar Radiation and Productivity in Tropical Ecosystems. *Journal of Applied Ecology*, 9(3):747–766, 1972. URL `https://www.jstor.org/stable/2401901`.

J. L. Monteith and C. J. Moss. Climate and the Efficiency of Crop Production in Britain and Discussion. *Philosophical Transactions of the Royal Society B Biological Sciences*, 281(980):277–294, 1977.

I. Moorthy, J. R. Miller, and T. L. Noland. Estimating chlorophyll concentration in conifer needles with hyperspectral data: An assessment at the needle and canopy level. *Remote Sensing of Environment*, 112(6):2824–2838, 2008.

F Pietrini, MA Iannelli, and A Massacci. Anthocyanin accumulation in the illuminated surface of maize leaves enhances protection from photo-inhibitory risks at low temperature, without further limitation to photosynthesis. *Plant, Cell & Environment*, 25(10):1251–1259, 2002.

A. Porcar-Castell, E. Tyystjärvi, J. Atherton, C. van der Tol, J. Flexas, E. E. Pfündel, J. Moreno, C. Frankenberg, and J. A. Berry. Linking chlorophyll a fluorescence to photosynthesis for remote sensing applications: mechanisms and challenges. *Journal of experimental botany*, 65(15):4065–4095, 2014.

A. Porcar-Castell, A. Mac Arthur, M. Rossini, L. Eklundh, J. Pacheco-Labrador, K. Anderson, M. Balzarolo, M. P. Martín, H. Jin, E. Tomelleri, et al. Eurospec: at the interface between remote-sensing and ecosystem co flux measurements in europe. *Biogeosciences*, 12(20):6103–6124, 2015.

M. Rautiainen, P. Lukeš, L. Homolova, A. Hovi, J. Pisek, and M. Mottus. Spectral properties of coniferous forests: A review of in situ and laboratory measurements. *Remote Sensing*, 10(2):207, 2018.

M. Reichstein, E. Falge, D. Baldocchi, D. Papale, M. Aubinet, P. Berbigier, C. Bernhofer, N. Buchmann, T. Gilmanov, A. Granier, T. Grunwald, K. Havrankova, H. Ilvesniemi, D. Janous, A. Knohl, T. Laurila, A. Lohila, D. Loustau, G. Matteucci, T. Meyers, F. Miglietta, J. Ourcival, J. Pumpanen, S. Rambal, E. Rotenberg, M. Sanz, J. Tenhunen, G. Seufert, F. Vaccari, T. Vesala, D. Yakir, and R. Valentini. On the separation of net ecosystem exchange into assimilation and ecosystem respiration: review and improved algorithm. *Global Change Biology*, 11(9):1424–1439, sep 2005. ISSN 1354-1013. doi: 10.1111/j.1365-2486.2005.001002.x. URL `http://doi.wiley.com/10.1111/j.1365-2486.2005.001002.x`.

A. D. Richardson, B. H. Braswell, D. Y. Hollinger, J. P. Jenkins, and S. V Ollinger. Near-surface remote sensing of spatial and temporal variation in canopy phenology. *Ecological Applications*, 19(6):1417–1428, 2009.

A. D. Richardson, K. Hufkens, T. Milliman, D. M. Aubrecht, M. Chen, J. M. Gray, M. R. Johnston, T. F. Keenan, S. T. Klosterman, M. Kosmala, E. K. Melaas, M. A. Friedl, and S. Frolking. Tracking vegetation phenology across diverse North American biomes using PhenoCam imagery. *Scientific Data*, 5: 180028, mar 2018. ISSN 2052-4463. doi: 10.1038/sdata.2018.28. URL http://www.nature.com/articles/sdata201828.

N. P. Robinson, B. W. Allred, W. K. Smith, M. O. Jones, A. Moreno, T. A. Erickson, D. E. Naugle, and S. W. Running. Terrestrial primary production for the conterminous United States derived from Landsat 30 m and MODIS 250 m. *Remote Sensing in Ecology and Conservation*, 4(3):264–280, sep 2018. ISSN 20563485. doi: 10.1002/rse2.74. URL http://doi.wiley.com/10.1002/rse2.74.

D. A. Rook. The influence of growing temperature on photosynthesis and respiration of Pinus radiata seedlings. *New Zealand Journal of Botany*, 7(1):43–55, mar 1969. ISSN 0028-825X. doi: 10.1080/0028825X.1969.10429101. URL http://www.tandfonline.com/doi/abs/10.1080/0028825X.1969.10429101.

J. W. Rouse Jr, R. H. Haas, J. A. Schell, and D. W. Deering. Monitoring vegetation systems in the great plains with erts. *Third ERTS Symposium, NASA SP-351.1.*, pages 309–317, 1974.

S. W. Running, R. R. Nemani, F. A. Heinsch, M. Zhao, M. Reeves, and H. Hashimoto. A Continuous Satellite-Derived Measure of Global Terrestrial Primary Production. *BioScience*, 54(6):547–560, jun 2004. ISSN 0006-3568. doi: 10.1641/0006-3568(2004)054[0547:acsmog]2.0.co;2. URL https://academic.oup.com/bioscience/article/54/6/547/294347.

U. Schreiber, U. Schliwa, and W. Bilger. Continuous recording of photochemical and non-photochemical chlorophyll fluorescence quenching with a new type of modulation fluorometer. *Photosynthesis research*, 10(1-2):51–62, 1986.

S. P. Serbin, D. N. Dillaway, E. L. Kruger, and P. A. Townsend. Leaf optical properties reflect variation in photosynthetic metabolism and its sensitivity to temperature. *Journal of Experimental Botany*, 63(1):489–502, jan 2012. ISSN 1460-2431. doi: 10.1093/jxb/err294. URL https://academic.oup.com/jxb/article-lookup/doi/10.1093/jxb/err294.

S. P. Serbin, A. Singh, B. E. McNeil, C. C. Kingdon, and P. A. Townsend. Spectroscopic determination of leaf morphological and biochemical traits for northern temperate and boreal tree species. *Ecological Applications*, 24(7):1651–1669, 2014.

S. P. Serbin, A. Singh, A. R. Desai, S. G. Dubois, A. D. Jablonski, C. C. Kingdon, E. L. Kruger, and P. A. Townsend. Remotely estimating photosynthetic capacity, and its response to temperature, in vegetation canopies using imaging spectroscopy. *Remote Sensing of Environment*, 167:78–87, 2015.

V. Silva-Perez, G. Molero, S. P. Serbin, A. G. Condon, M. P. Reynolds, R. T. Furbank, and J. R. Evans. Hyperspectral reflectance as a tool to measure biochemical and physiological traits in wheat. *Journal of Experimental Botany*, 69(3):483–496, jan

2018. ISSN 0022-0957. doi: 10.1093/jxb/erx421. URL https://academic.oup.com/jxb/article/69/3/483/4772616.

D. A. Sims and J. A. Gamon. Relationships between leaf pigment content and spectral reflectance across a wide range of species, leaf structures and developmental stages. *Remote sensing of environment*, 81(2-3):337–354, 2002.

A. Singh, S. P. Serbin, B. E. McNeil, C. C. Kingdon, and P. A. Townsend. Imaging spectroscopy algorithms for mapping canopy foliar chemical and morphological traits and their uncertainties. *Ecological Applications*, 25(8):2180–2197, 2015.

M.-L. Smith, S. V. Ollinger, M. E. Martin, J. D. Aber, R. A. Hallett, and C. L. Goodale. Direct estimation of aboveground forest productivity through hyperspectral remote sensing of canopy nitrogen. *Ecological applications*, 12(5): 1286–1302, 2002.

O. Sonnentag, K. Hufkens, C. Teshera-Sterne, A. M. Young, M. Friedl, B. H. Braswell, T. Milliman, J. O'Keefe, and A. D. Richardson. Digital repeat photography for phenological research in forest ecosystems. *Agricultural and Forest Meteorology*, 152:159–177, jan 2012. ISSN 0168-1923. doi: 10.1016/J.AGRFORMET.2011.09.009. URL https://www.sciencedirect.com/science/article/pii/S0168192311002851.

C. Stylinski, J. Gamon, and W. Oechel. Seasonal patterns of reflectance indices, carotenoid pigments and photosynthesis of evergreen chaparral species. *Oecologia*, 131(3):366–374, may 2002. ISSN 0029-8549. doi: 10.1007/s00442-002-0905-9. URL http://link.springer.com/10.1007/s00442-002-0905-9.

C. J. Tucker. Red and photographic infrared linear combinations for monitoring vegetation. *Remote Sensing of Environment*, 8(2):127–150, may 1979. ISSN 0034-4257. doi: 10.1016/0034-4257(79)90013-0. URL https://www.sciencedirect.com/science/article/pii/0034425779900130.

S. L. Ustin, D. A. Roberts, J. A. Gamon, G. P. Asner, and R. O. Green. Using imaging spectroscopy to study ecosystem processes and properties. *BioScience*, 54(6):523–534, 2004.

S. L. Ustin, A. A. Gitelson, S. Jacquemoud, M. Schaepman, G. P. Asner, J. A. Gamon, and P. Zarco-Tejada. Retrieval of foliar information about plant pigment systems from high resolution spectroscopy. *Remote Sensing of Environment*, 113: S67–S77, 2009.

C. vander Tol, J. A. Berry, P. K. E. Campbell, and U. Rascher. Models of fluorescence and photosynthesis for interpreting measurements of solar-induced chlorophyll fluorescence. *Journal of Geophysical Research: Biogeosciences*, 119(12):2312–2327, dec 2014. ISSN 21698953. doi: 10.1002/2014JG002713. URL http://doi.wiley.com/10.1002/2014JG002713.

A. S. Verhoeven, W. W. Adams, and B. Demmig-Adams. Close relationship between the state of the xanthophyll cycle pigments and photosystem II efficiency during recovery from winter stress. *Physiologia Plantarum*, 96(4):567–576, apr 1996. ISSN 0031-9317. doi: 10.1111/j.1399-3054.1996.tb00228.x. URL http://doi.wiley.com/10.1111/j.1399-3054.1996.tb00228.x.

N. Vilfan, C. Van der Tol, P. Yang, R. Wyber, Z. Malenovský, S. A. Robinson, and W. Verhoef. Extending Fluspect to simulate xanthophyll driven leaf reflectance dynamics. *Remote Sensing of Environment*, 211:345–356, jun 2018. ISSN 0034-4257. doi: 10.1016/J.RSE.2018.04.012. URL https://www.sciencedirect.com/science/article/pii/S0034425718301573.

L. Wingate, J. Ogée, E. Cremonese, G. Filippa, T. Mizunuma, M. Migliavacca, C. Moisy, M. Wilkinson, C. Moureaux, G. Wohlfahrt, A. Hammerle, L. Hörtnagl, C. Gimeno, A. Porcar-Castell, M. Galvagno, T. Nakaji, J. Morison, O. Kolle, A. Knohl, W. Kutsch, P. Kolari, E. Nikinmaa, J. Levula, B. Heinesch, M. Sprintsin, D. Yakir, T. Manise, D. Guyon, H. Ahrends, A. Plaza-Aguilar, J. H. Guan, and J. Grace. Interpreting canopy development and physiology using a European phenology camera network at flux sites. *Biogeosciences*, 12:24, 2015. doi: 10.5194/bg-12-5995-2015. URL www.biogeosciences.net/12/5995/2015/.

S. Wold, A. Ruhe, H. Wold, and W. J. Dunn, III. The collinearity problem in linear regression. the partial least squares (pls) approach to generalized inverses. *SIAM Journal on Scientific and Statistical Computing*, 5(3):735–743, 1984.

C. Y. S. Wong and J. A. Gamon. Three causes of variation in the photochemical reflectance index (PRI) in evergreen conifers. *New Phytologist*, 206(1), 2015a. ISSN 14698137. doi: 10.1111/nph.13159.

C. Y. S. Wong and J. A. Gamon. The photochemical reflectance index provides an optical indicator of spring photosynthetic activation in evergreen conifers. *New Phytologist*, 206(1):196–208, 2015b.

C. Y. S. Wong, P. D'Odorico, Y. Bhathena, M. A. Arain, and I. Ensminger. Carotenoid based vegetation indices for accurate monitoring of the phenology of photosynthesis at the leaf-scale in deciduous and evergreen trees. *Remote Sensing of Environment*, 233:111407, 2019. ISSN 0034-4257. doi: https://doi.org/10.1016/j.rse.2019.111407. URL http://www.sciencedirect.com/science/article/pii/S0034425719304262.

C. Y. S. Wong, P. D'Odorico, M. A. Arain, and I. Ensminger. Tracking the phenology of photosynthesis using carotenoid-sensitive and near-infrared reflectance vegetation indices in a temperate evergreen and mixed deciduous forest. *New Phytologist*, 2020.

W. Woodgate, L. Suarez, E. van Gorsel, L.A. Cernusak, R. Dempsey, R. Devilla, A. Held, M.J. Hill, and A.J. Norton. tri-PRI: A three band reflectance index tracking dynamic photoprotective mechanisms in a mature eucalypt forest. *Agricul-*

tural and Forest Meteorology, 272-273:187–201, jul 2019. ISSN 0168-1923. doi: 10.1016/J.AGRFORMET.2019.03.020. URL https://www.sciencedirect.com/science/article/pii/S0168192319301327?via{\%}3Dihub.

T. Wutzler, A. Lucas-Moffat, M. Migliavacca, J. Knauer, K. Sickel, L. Šigut, O. Menzer, and M. Reichstein. Basic and extensible post-processing of eddy covariance flux data with REddyProc. *Biogeosciences*, 15:5015–5030, 2018. doi: 10.5194/bg-15-5015-2018. URL https://doi.org/10.5194/bg-15-5015-2018.

X. Xiao, D. Hollinger, J. Aber, M. Goltz, E. A. Davidson, Q. Zhang, and B. Moore. Satellite-based modeling of gross primary production in an evergreen needleleaf forest. *Remote Sensing of Environment*, 89(4):519–534, 2004. ISSN 00344257. doi: 10.1016/j.rse.2003.11.008.

P. Yang and C. van der Tol. Linking canopy scattering of far-red sun-induced chlorophyll fluorescence with reflectance. *Remote sensing of environment*, 209: 456–467, 2018.

P. J. Zarco-Tejada, A. Hornero, P. S. A. Beck, T. Kattenborn, P. Kempeneers, and R. Hernández-Clemente. Chlorophyll content estimation in an open-canopy conifer forest with sentinel-2a and hyperspectral imagery in the context of forest decline. *Remote sensing of environment*, 223:320–335, 2019.

C. R. Zarter, W. W. Adams, V. Ebbert, D. J. Cuthbertson, I. Adamska, and B. Demmig-Adams. Winter down-regulation of intrinsic photosynthetic capacity coupled with up-regulation of Elip-like proteins and persistent energy dissipation in a subalpine forest. *New Phytologist*, 172(2):272–282, oct 2006. ISSN 0028-646X. doi: 10.1111/j.1469-8137.2006.01815.x. URL http://doi.wiley.com/10.1111/j.1469-8137.2006.01815.x.

M. Zhao, F. A. Heinsch, R. R. Nemani, and S. W. Running. Improvements of the MODIS terrestrial gross and net primary production global data set. *Remote Sensing of Environment*, 95(2):164–176, mar 2005. ISSN 0034-4257. doi: 10.1016/J.RSE.2004.12.011. URL https://www.sciencedirect.com/science/article/pii/S0034425705000106.

L. M. Zuromski, D. R. Bowling, P. Köhler, C. Frankenberg, M. L. Goulden, P. D. Blanken, and J. C. Lin. Solar-Induced Fluorescence Detects Interannual Variation in Gross Primary Production of Coniferous Forests in the Western United States. *Geophysical Research Letters*, 45(14):7184–7193, jul 2018. ISSN 00948276. doi: 10.1029/2018GL077906. URL http://doi.wiley.com/10.1029/2018GL077906.

Chapter 3

EVALUATING PHOTOSYNTHETIC ACTIVITY ACROSS ARCTIC-BOREAL LAND COVER TYPES USING SOLAR-INDUCED CHLOROPHYLL FLUORESCENCE

R. Cheng, T. S. Magney, E. L. Orcutt, Bowling D. R., M. S. Bret-Harte, E. S. Euskirchen, M. Jung, H. Kobayashi, P. Köhler, Z. Pierrat, A. V. Rocha, O. Sonnentag, S. Walther, D. Zona, and C. Frankenberg. "Evaluating photosynthetic activity across Arctic-Boreal land cover types using Solar-Induced chlorophyll Fluorescence" (under review). In: *Environmental Research Letters*.

3.1 Abstract

Photosynthesis of terrestrial ecosystems in the Arctic-Boreal region is a critical part of the global carbon cycle. Solar-Induced chlorophyll Fluorescence (SIF), a promising proxy for photosynthesis with physiological insight, has been used to track Gross Primary Production (GPP) at regional scales. Recent studies have constructed empirical relationships between SIF and eddy covariance-derived GPP as a first step to predicting global GPP. However, high latitudes pose two specific challenges: 1) Unique plant species and land cover types in the Arctic-Boreal region are not included in the generalized SIF-GPP relationship from lower latitudes, and 2) the complex terrain and sub-pixel land cover further complicate the interpretation of the SIF-GPP relationship. In this study, we focused on the Arctic-Boreal Vulnerability Experiment (ABoVE) domain and evaluated the empirical relationships between SIF for high latitudes from the TROPOspheric Monitoring Instrument (TROPOMI) and a state-of-the-art machine learning GPP product (FluxCom). For the first time, we report the regression slope, linear correlation coefficient, and the goodness of the fit of SIF-GPP relationships for Arctic-Boreal land cover types with extensive spatial coverage. We found several potential issues specific to the Arctic-Boreal region that should be considered: 1) unrealistically high FluxCom GPP due to the presence of snow and water at the subpixel scale; 2) changing biomass distribution and SIF-GPP relationship along elevational gradients, and 3) limited perspective and misrepresentation of heterogeneous land cover across spatial resolutions. Taken together, our results will help improve the estimation of GPP using SIF in terrestrial biosphere models and cope with model-data uncertainties in the Arctic-Boreal region.

3.2 Introduction

As a critical part of the global carbon cycle and land carbon sink for atmospheric CO_2, terrestrial photosynthesis in the Arctic-Boreal region can play a key role in mitigating global climate change (Beer et al., 2010; Mishra and Riley, 2012). Due to exceedingly high warming trends at high latitudes (Post et al., 2019; Walsh and Brettschneider, 2019), Arctic-Boreal ecosystems are undergoing more rapid changes than the rest of the world (Box et al., 2019; Canadell et al., 2021), such as in photosynthetic productivity, growing season phenology, and vegetation composition (Myers-Smith et al., 2020). As a result, the future direction and magnitude of terrestrial ecosystem change in these systems has become highly uncertain (Loisel et al., 2021; McGuire et al., 2009; Zona et al., 2022). To better evaluate climate impacts on the Arctic-Boreal region and understand vegetation-climate feedbacks, monitoring the status of Arctic-Boreal terrestrial photosynthesis is essential (Fisher et al., 2014).

Plant carbon uptake via photosynthesis at the ecosystem scale, Gross Primary Production (GPP), can only be estimated indirectly from the ground or space. On the ground, tower-based Eddy Covariance (EC) techniques directly measure net ecosystem CO_2 exchange (Baldocchi, 2003), which is then partitioned into GPP and ecosystem respiration. EC towers in the Arctic-Boreal region are unevenly and sparsely distributed in space (Figure 3.1, Table 3.1), which make it difficult to represent the spatial variability of GPP across heterogeneous Land Cover (LC) in the Arctic-Boreal region (Curasi et al., 2022; Pallandt et al., 2022). EC techniques are also prone to error in complex terrain, which plays an important role in above-ground biomass distributions in the Arctic-Boreal region (Bruun et al., 2006; Dobrowski, 2011; Riihimäki et al., 2017).

Similar to EC towers, satellite remote sensing techniques indirectly infer GPP. An advantage of satellite remote sensing techniques is a more extensive spatial coverage, enabling the comparison of GPP across heterogeneous LC (Funk et al., 2004; Roland et al., 2021) and complex Arctic-Boreal terrain (Roland et al., 2019). However, satellite remote sensing techniques also have higher uncertainties due to more assumptions made in the derivation of GPP (Ryu et al., 2019; Tramontana et al., 2015).

Remote sensing techniques often rely on canopy optical properties that can approximate Absorbed Photosynthetic Active Radiation (APAR) by vegetation. The fraction of APAR used for photosynthesis is referred to as Light Use Efficiency (LUE). So, GPP can be derived as

$$\mathrm{GPP} = \mathrm{APAR} \times \mathrm{LUE}\,. \tag{3.1}$$

Remote sensing GPP products, such as from the Moderate Resolution Imaging Spectroradiometer (MODIS) (Running et al., 2004; Zhao et al., 2005), are primarily derived from the normalized difference in the surface reflectance between red and near-infrared regions, which is a proxy for the fraction of incoming light absorbed by the canopy, or APAR. However, APAR changes alone are not representative of the seasonal cycle in boreal evergreen ecosystems well, as vegetation photosynthetic activity ceases while maintaining chlorophyll throughout the season (Bowling et al., 2018; Cheng et al., 2020; Magney et al., 2019). Thus, quantifying variations in LUE is crucial for accurately estimating Arctic-Boreal GPP.

Remote sensing of Solar-Induced chlorophyll Fluorescence (SIF) from space opens up a new possibility to infer GPP remotely. SIF is a small amount of energy emitted from leaf chlorophyll, which is driven by APAR. SIF appears to be a good indicator of the partitioning of APAR between photochemical quenching for photosynthesis and non-photochemical quenching, i.e. LUE (Magney et al., 2019; Pierrat et al., 2022), especially in challenging environments that are snowy or have low solar angles (Walther et al., 2016, 2018). Thus, satellite-based SIF is a promising tool for inferring GPP at the regional scale in the Arctic-Boreal region.

Similar to Equation 3.1, SIF can be conceptualized as:

$$\mathrm{SIF} = \mathrm{APAR} \times \Phi_F \times f_{esc}\,, \tag{3.2}$$

where Φ_F is the quantum yield of fluorescence, and f_{esc} is the escape ratio of SIF from the canopy (Guanter et al., 2014; Zeng et al., 2019). To predict GPP using SIF, recent studies have built an empirical linear model between daily mean GPP from EC towers and daily mean SIF ($\mathrm{SIF_{dc}}$) from the TROPOspheric Monitoring Instrument (TROPOMI; Köhler et al. 2018), assuming linearity between $\mathrm{SIF_{dc}}$ and GPP (Liu et al., 2022; Turner et al., 2021):

$$\mathrm{GPP} = \mathrm{k} \cdot \mathrm{SIF_{dc}}. \tag{3.3}$$

Thus, the regression slope k can be generalized in different plant functional types to account for varying photosynthetic yields, SIF yields, and canopy structures since it is a function of LUE, Φ_F, and f_{esc}:

$$\mathrm{k} \sim \frac{LUE}{\Phi_F \times f_{esc}}\,. \tag{3.4}$$

Solving and categorizing k by plant functional types has improved the ability of biosphere models to simulate GPP in temperate regions (Delaria et al., 2021; Wu et al., 2021). However, the resulting k values from Turner et al. (2021) and Liu et al. (2022) lack representativeness in the Arctic-Boreal region because they are categorized by general definitions of plant functional types at the global scale, which cannot fully explain the unique vegetation composition and LC's in the Arctic-Boreal region.

Hence, the goal of this study is to quantitatively evaluate the empirical SIF-GPP relationship (Equation 3.3) and its uncertainty in the context of the Arctic-Boreal region at the regional scale using remote sensing techniques. We chose to focus on the core region Arctic-Boreal Vulnerability Experiment (ABoVE) domain, where LC types have been defined and validated in the context of Arctic-Boreal species and canopy structures (Figure 3.1a; Wang et al. 2019). To obtain extensive spatial coverage we fit the empirical SIF-GPP relationship and solved for k using TROPOMI SIF_{dc} and a state-of-the-art machine learning gridded GPP product (FluxCom RS; Jung et al. 2020). To help biosphere modelers cope with the model-data uncertainties (Keenan et al., 2011; Xiao et al., 2014), we evaluated the goodness of empirically fitted SIF-GPP relationships with Pearson's r^2 values and reduced χ^2 given the uncertainties in both FluxCom GPP and TROPOMI SIF_{dc}.

We also address three other sources of uncertainties in the SIF-GPP relationship: 1) snow contamination in remote sensing products, 2) changing biomass distribution along elevational gradients, and 3) limited perspective and misrepresentation of heterogeneous LC across spatial resolutions. Here, we present the opportunities and limitations of remote sensing and machine learning tools for studying GPP in the Arctic-Boreal region (Section 3.5).

3.3 Data and methods

Gridded datasets and their uncertainties

FluxCom GPP

We used the ensemble median of 2018-2019 8-day GPP from the FluxCom Remote Sensing (RS) ensembles (Jung et al., 2020; Tramontana et al., 2016) with a spatial resolution of 0.08333°× 0.08333°. FluxCom RS ensembles include 18 members from 9 machine learning models and 2 GPP flux partitioning methods. Using GPP from EC towers as training data (Tramontana et al., 2016), all ensemble members predict GPP with the same predictors, including land surface temperature, land cover, the fraction of absorbed photosynthetically active radiation, and Normalized Difference Vegetation Index (NDVI) from MODIS land products. We took the standard deviation of the predicted GPP of all ensembles as the uncertainty of FluxCom GPP.

Because the FluxCom RS GPP is predicted by remote sensing products, snow contamination in MODIS products (Cihlar, 1996) can propagate into FluxCom GPP. To evaluate the impact of snow contamination on the SIF-GPP relationship, we compared the seasonal trajectory of FluxCom GPP with and without snow filtering. We used the 2018-2019 8-day MODIS L3 0.05°global snow cover product

MOD10C2 (Hall and Riggs, 2021) as a snow filter, which reports the area fraction of snow cover (dimensionless) in each grid. The snow cover data in the study area were interpolated to the same spatial and temporal resolution as the FluxCom GPP product. Here, we define FluxCom GPP as snow-free when the snow cover is less than 0.1.

Additionally, the uncertainty of FluxCom GPP can be also due to the extrapolation of trained parameters due to limited EC towers sampling. Jung et al. (2020) has developed an Extrapolation Index (EI) to address this issue by illustrating the total distance of an extrapolated point to the nearest training data in the space of all predictors. Here, we reproduced the multi-year average (2001-2018) of annual mean EI and its seasonal range in the study domain to qualitatively examine the representativeness of FluxCom GPP.

TROPOMI SIF

We gridded individual SIF soundings from TROPOMI at 740 nm between 2018 and 2019 in the study area to the same spatial and temporal resolutions as FluxCom GPP. Because satellite-based SIF is an instantaneous value indicative of the light condition at the time of measurement, the daily mean SIF, SIF_{dc}, was scaled from the instantaneous measurement using a length-of-day correction factor based on the diurnal cycle of solar radiation (Köhler et al., 2018). To account for varying numbers of soundings across grids, we took the standard error of SIF_{dc} from individual soundings falling in each grid as the uncertainty of TROPOMI SIF, which is derived as the standard deviation divided by the square root of the number of soundings.

Orthogonal distance regression

With snow-free FluxCom GPP and TROPOMI SIF_{dc} as well as their uncertainties, we fit the linear model in equation 3.3 without an intercept using the orthogonal distance regression (Boggs et al., 1992) for each grid cell, where the regression slope k, Pearson's r^2, and reduced χ^2 were computed.

Previous studies (Liu et al., 2022; Wu et al., 2022) have often used Pearson's r^2 as the only metric for explanatory power even though measurement noise can reduce Pearson's r^2, although the measurements themselves might be accurate but just less precise. Thus, we use both Pearson's r^2 and reduced χ^2 together to evaluate the linear empirical model between GPP and SIF_{dc} from the perspective of correlation (Pearson's r^2) as well as the goodness of the fit (reduced χ^2). High reduced χ^2

suggests the linear model is underfitting the data. When reduced χ^2 is lower than 1, it suggests that the linear model is overfitting the given uncertainties on FluxCom GPP and grid TROPOMI SIF_{dc}. A reduced χ^2 around 1 represents a good fit, regardless of Pearson's r^2 value.

Arctic-Boreal land cover map

In the context of Arctic-Boreal species and canopy structures, we categorized the fitted k, Pearson's r^2, and reduced χ^2 by 15 Arctic-Boreal LC types based on 2014 ABoVE Land Cover (LC) dataset from (Wang et al., 2019). The original spatial resolution of the LC dataset is 30 m × 30 m (LC30M), which we aggregated into 0.08333°× 0.08333°(LC008333D) grids to align with FluxCom GPP. The LC pixels of LC30M were counted within each LC008333D grid. The LC type with the maximal area fraction in the LC008333D grid is defined as the dominant LC type (Figure 3.1a), while the maximal area fraction is defined as the dominant LC fraction (Figure 3.1b). Heterogenous LC is associated with a lower dominant LC fraction.

Surface water is common in Arctic-Boreal ecosystems (Muster et al., 2013; Stow et al., 2004). However, NDVI obtained from mixed pixels including both vegetation and water surface is often close to that of vegetation only. Because water surfaces are very dark (Jiang et al., 2005), few of the reflected photons measured from space emanate from water surfaces. To estimate the influence of the underestimated surface water on FluxCom GPP which uses NDVI (Tramontana et al., 2016), we calculated the area fraction per LC008333D grid occupied by wetland LC types including *Fen*, *Bog*, and *Water*. Here, we neglected *Shallows/littoral* LC type as it is non-vegetation dominated and dominates less than 0.1% of all LC008333D grids.

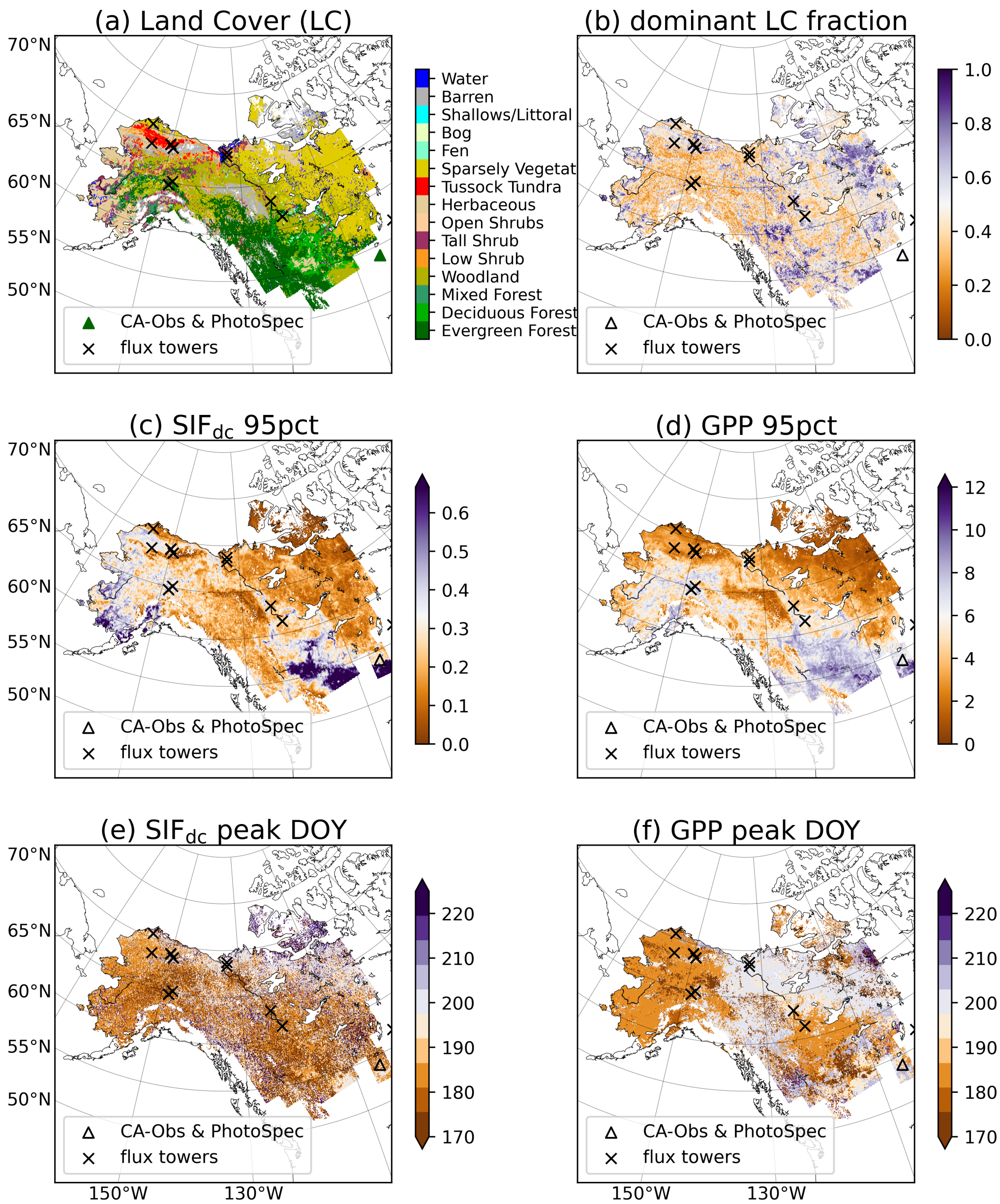

Figure 3.1: In the study area (core region of the Arctic-Boreal Vulnerability Experiment (ABoVE) domain) and the resolution of 0.08333°× 0.08333°: (a) the dominant Land Cover (LC) types Wang et al. (2019); (b) the area fraction of grid taken by the dominant LC types in panel (a); (c) the 95 percentile of SIF$_{dc}$ (mW m^{-2} sr^{-1} nm^{-1}); (d) the 95 percentile of snow-free FluxCom GPP (gC m^{-2} day^{-1}); (e) the day of year when SIF$_{dc}$ peaks; and (f) the day of year when GPP peaks. The black cross scatters show the locations of EC towers with GPP data within the ABoVE LC map. The triangle scatter denotes the location of CA-Obs which has both GPP data and tower-based SIF data. In (a) the triangle scatter is colored in dark green to show that the LC type of CA-Obs footprint is *Evergreen Forest*. In (c)-(f), the maps are extended to the area surrounding CA-Obs since data are available.

Topography

We decomposed the resulting k, Pearson's r^2, and reduced χ^2 as a function of elevation. The elevation data in the study area were obtained from the USGS Global 30 Arc-Second elevation dataset (GTOPO30; Earth Resources Observation And Science (EROS) Center 2017). We regridded the elevation data to the same spatial resolution as FluxCom GPP using Google Earth Engine (Gorelick et al., 2017).

Ground-level GPP and SIF

Due to highly heterogeneous LC (Myers-Smith et al., 2020; Wang et al., 2020) in the Arctic-Boreal region, the SIF-GPP relationships at different observational scales can vary. Satellite footprints often cover a larger area than the footprints of EC towers so the dominant LC of the two scales may not match despite the satellite footprints centering on the location of towers. To address the difference and correspondence across scales, we compared the observations from towers against satellite pixels of the same LC types.

We used half-hourly gap-filled GPP data of EC towers from Principal Investigators (PIs) and the Fluxnet2015 dataset (Papale et al. 2015; Table 3.1) in the study area and calculated the daily mean EC GPP. Because of various temporal ranges for different towers, we calculated the multi-year average of daily mean EC GPP at the 8-day interval aligned with the temporal interval of FluxCom GPP. We defined the LC types for EC towers based on the description of tower footprints from site PIs.

We evaluated the TROPOMI SIF_{dc} data against a tower-based SIF product in CA-Obs (Pierrat and Stutz, 2022; Pierrat et al., 2022), which is close to our study area but outside the LC map. A 2-D scanning telescope measures SIF at 745-758nm across a canopy representative loop that repeats every half hour, from which we calculated daily mean SIF at 8-day intervals. The International Geosphere-Biosphere Programme (IGBP) classification of CA-Obs is Evergreen Needleleaf Forests (ENF). Thus, we used it to benchmark FluxCom GPP and gridded TROPOMI SIF_{dc} in *Evergreen Forest*.

Table 3.1: EC towers with GPP data used in this study. LC30M is the LC type based on the original spatial resolution (30 m × 30 m) of Wang et al. (2019). LC008333D is the dominant LC type in the resolution of 0.08333°× 0.08333°, which is aggregated from LC30M. IGBP is the LC type reported by principal investigators based on the International Geosphere-Biosphere Programme (IGBP). ENF, OSH, WET are evergreen needle leaf forests, open shrublands, and permanent wetlands, respectively. Footprint LC is the estimated dominant LC in the EC tower footprints in the scheme of Wang et al. (2019) based on the description from PIs and previous studies.

Name	LC30M	LC008333D	IGBP	tower footprint LC	mean canopy height (m)	elevation (m)	start month	end month	reference
CA-HPC	*Fen*	*Woodland*	*ENF*	*Woodland*	3.93	80	2017.4	2017.11	Sonnentag and Marsh (2021b)
CA-Obs	-	-	*ENF*	*Evergreen Forest*	14	629	2019.7	2020.12	Black (2016); Pierrat and Stutz (2022)
CA-SMC	*Woodland*	*Water*	*ENF*	*Evergreen Forest*	6.15	150	2017.7	2017.11	Sonnentag (2021)
CA-TVC	*Herbaceous*	*Low Shrub*	*OSH*	*Low Shrub*	0.25	85	2017.5	2017.10	Sonnentag and Marsh (2021a)
DEJU	*Evergreen Forest*	*Woodland*	*ENF*	*Evergreen Forest*	10	529	2018.1	2021.9	NEON (2022)
US-An1	*Sparsely Vegetated*	*Tussock Tundra*	*OSH*	*Sparsely Vegetated*	0.6	600	2017.6	2017.8	Rocha et al. (2016b)
US-An3	*Tussock Tundra*	*Tussock Tundra*	*OSH*	*Tussock Tundra*	0.2	600	2017.6	2017.8	Rocha et al. (2016a)
US-Atq	*Low Shrub*	*Sparsely Vegetated*	*WET*	*Tussock Tundra*	0.12	15	2017.1	2017.12	Oechel et al. (2014)
US-BZB	*Woodland*	*Deciduous Forest*	*WET*	*Fen*	1	100	2017.1	2017.12	Euskirchen (2021c)
US-BZF	*Low Shrub*	*Deciduous Forest*	*WET*	*Fen*	1	95	2017.1	2017.12	Euskirchen (2021b)
US-BZS	*Woodland*	*Deciduous Forest*	*ENF*	*Evergreen Forest*	2.5	100	2017.1	2017.12	Euskirchen (2021a)
US-ICh	*Low Shrub*	*Tussock Tundra*	*OSH*	*Low Shrub*	0.1	940	2017.1	2017.12	Euskirchen et al. (2016c)
US-ICs	*Tussock Tundra*	*Tussock Tundra*	*WET*	*Fen*	0.1	920	2017.1	2017.12	Euskirchen et al. (2016b)
US-ICt	*Tussock Tundra*	*Tussock Tundra*	*OSH*	*Tussock Tundra*	0.1	930	2017.1	2017.12	Euskirchen et al. (2016a)
US-Ivo	*Herbaceous*	*Low Shrub*	*WET*	*Tussock Tundra*	0.1	568	2004.1	2007.12	Zona and Oechel (2016)
US-Prr	*Woodland*	*Woodland*	*ENF*	*Evergreen Forest*	2.9	210	2017.1	2017.10	Kobayashi et al. (2016)

3.4 Results

Seasonal trajectories of SIF and GPP

The 95th percentiles of TROPOMI SIF_{dc} and snow-free FluxCom GPP are not consistent across space (Figure 3.1c,d), suggesting that the regression slope k is not homogeneous in the Arctic-Boreal region. *Tussock Tundra* on the northern slope of the Brooks Range has a higher 95th percentile of SIF_{dc} than the surrounding area, while the 95th percentile of GPP is similar to the surrounding area. The 95th percentile of SIF_{dc} is high in the southern portion of our study area, which may be attributed to agricultural land located in southern Alberta and Saskatchewan (Guanter et al., 2014).

Categorized by LC types, the dynamic ranges of GPP and SIF_{dc} vary by LCs (Figure 3.2). The growing season maximal GPP is the lowest in LCs with lower statures, such as *Low Shrub* and *Tussock Tundra*. The growing season maximal SIF_{dc} is often lower than 0.5 mW m^{-2} sr^{-1} nm^{-1} except in *Deciduous Forest*, *Woodland*, *Tall Shrub*, and *Herbaceous*.

In *Woodland*, the linear SIF_{dc}-GPP relationship splits (Figure 3.2d) because *Woodland* is a heterogeneous LC type coexisting with other LC types by definition (Wang et al., 2019). Thus, the SIF_{dc}-GPP relationship of *Woodland* contain the features of both high- and low-statured LC types.

The linear correlation of GPP and SIF_{dc} from gridded products is comparable to tower-based measurements (Figure 3.2). However, the maximum EC GPP is lower than FluxCom GPP in *Evergreen Forest*, suggesting that FluxCom GPP may be overestimated in this LC type. EC GPP can be negative during winter, which is an artifact of the flux partitioning (Hagen et al., 2006; Wutzler et al., 2018). The daily mean SIF from the tower-based instrument in CA-Obs nicely falls in the dynamic range of TROPOMI SIF_{dc} (Figure 3.2a).

On average, the highest regression slope k among the vegetation dominated LC types occurs in *Evergreen Forest* (33.84 (gC m^{-2} day^{-1})/(mW m^{-2} sr^{-1} nm^{-1})), while the lowest k value is in *Tussock Tundra* (12.89 (gC m^{-2} day^{-1})/(mW m^{-2} sr^{-1} nm^{-1})).

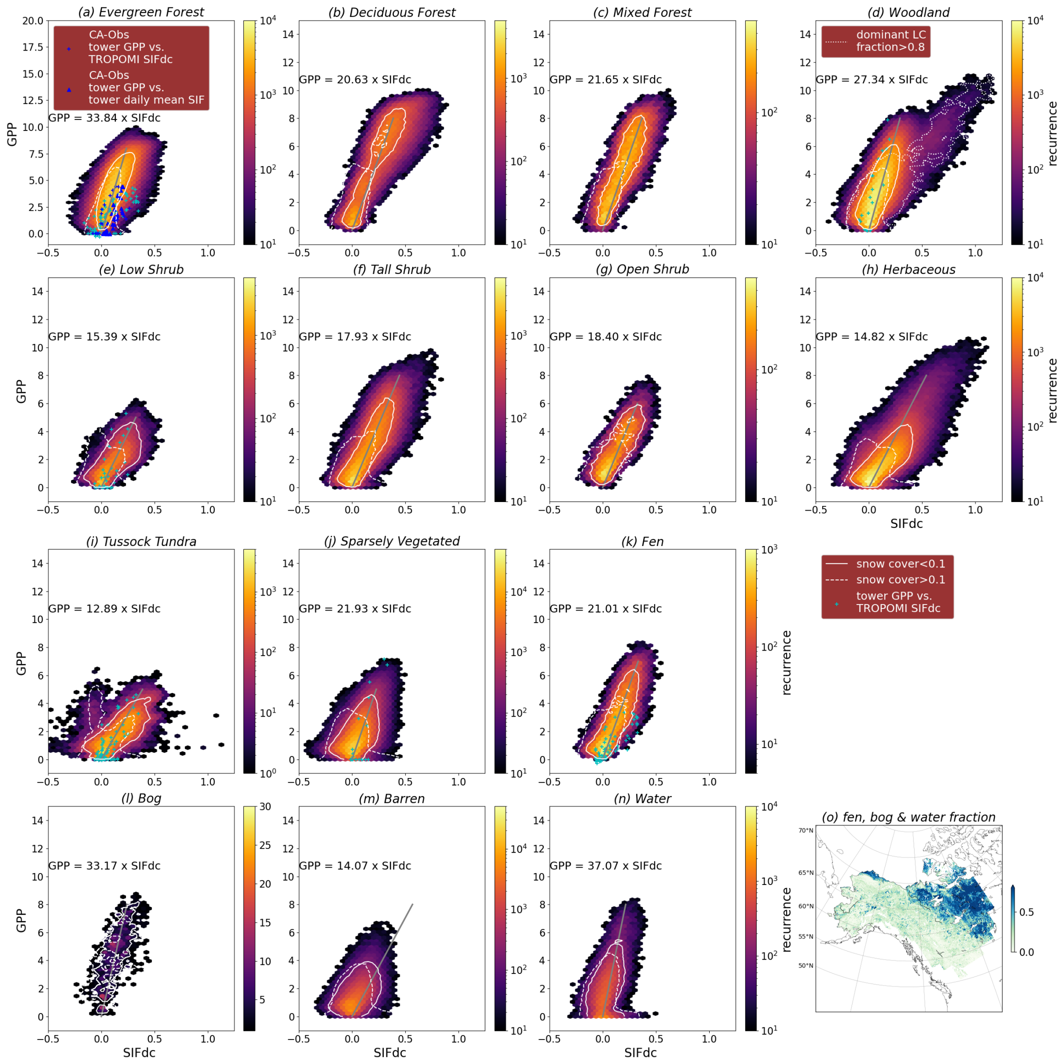

Figure 3.2: The hexbins are pixels categorized by the dominant LC types in Figure 3.1a based on all data of 2018-2019 8-day TROPOMI SIF_{dc} (mW m^{-2} sr^{-1} nm^{-1}) and FluxCom GPP (gC m^{-2} day^{-1}) in the study area. The color of hexbins represents the pixel recurrence at a given pair of SIF_{dc} and GPP bins. The white solid contours are the 95 percentile of the recurrence when the snow cover is less than 0.1 (snow-free). The white dashed contours are the 95 percentile of the recurrence when the snow cover is greater than 0.1. The dotted white contour in (d) is the 95 percentile of grids where the dominant LC (a.k.a Woodland) fraction is greater than 80%. The blue crosses are the multi-year average of 8-day TROPOMI SIF_{dc} and daily mean EC GPP from CA-Obs. The blue triangles are the multi-year average of 8-day tower-based daily mean SIF and daily mean EC GPP from CA-Obs. The cyan crosses are the multi-year average of 8-day TROPOMI SIF_{dc} and daily mean EC GPP from all other EC towers according to LC types. The gray line is the mean SIF-GPP relationship with the math expression noted in each land cover type. Panel (o) shows the area fraction occupied by *Fen*, *Bog*, and *Water*.

Spatial patterns of the SIF-GPP relationship

The spatial distribution of the resulting regression slope k (Figure 3.3a) is primarily a function of LC types (Figure 3.1a). Similar to Figure 3.2, k is higher in *Evergreen Forest*, which is in the southwest part of the study area, and lower in *Tussock Tundra* on the northern slope of the Brooks Range.

The goodness of the fit of the linear model (Equation 3.3) depends on the linearity of the seasonal trajectories of SIF_{dc} and GPP. When SIF_{dc} and GPP peak synchronously, the SIF-GPP relationship becomes more linear. Generally, SIF_{dc} and GPP peak simultaneously across our study area (Figure 3.1ef). In Western Alaska and North of the Rocky mountains SIF_{dc} and GPP peak earlier than in Northern Canada, suggesting the fit of the linear regression model of SIF_{dc} and GPP (Equation 3.3) may not be equally good across space.

Most of our study area has moderate to high Pearson's r^2 (Figure 3.3b). In the *Sparsely Vegetated* northeastern part of the study area, the annual mean EI (Figure 3.3f) is high, indicating that the FluxCom models predict GPP in this region with few training samples and thus yield higher uncertainties. The high seasonal range in EI (Figure 3.3d) suggests the extrapolation is more severe in winter than in summer.

The reduced χ^2 is much higher than 1 near glacial lakes in Northern Canada (Figure 3.3a) and *Deciduous Forest*, indicating the empirically fitted SIF-GPP relationship is underestimated and does not fully capture the seasonal trajectories in SIF_{dc} and GPP. One possible reason is that most training samples used by FluxCom models in the Arctic-Boreal are not *Deciduous Forest* (Figure 3.3f and 3.1a). Thus, the FluxCom models have to extrapolate from training samples that are less similar to the environment of the region so that the FluxCom GPP has a higher error in *Deciduous Forest*.

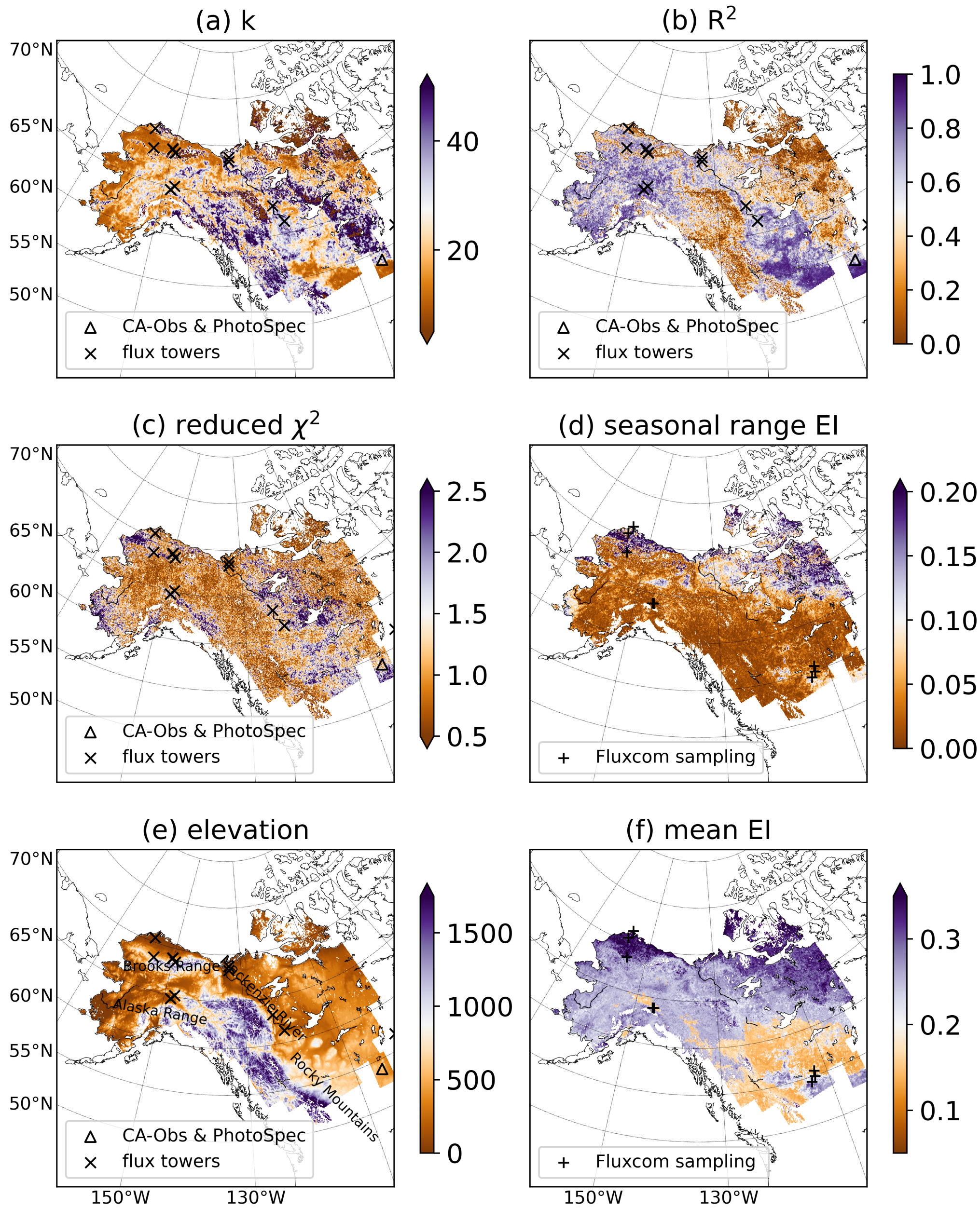

Figure 3.3: Maps of (a) resulting regression slope k, (b) Pearson's r^2, (c) reduced χ^2 from fitting snow-free FluxCom GPP and TROPOMI SIF_{dc}. Panel (e) is the elevation map of the study region. The scatters in (a-c) and (e) are the EC towers with ground-level GPP data and/or SIF measurements, which are used in Figure 3.2. Panels (d) and (f) are the multi-year average of seasonal range (winter (Januaray and Feburary) - summer (June and July)) and annual mean of Extrapolation Index (EI) from Jung et al. (2020). The scatters in (d) and (f) are the EC towers used to train FluxCom models. The maps are extended to the area surrounding CA-Obs since data are available.

Overestimated FluxCom GPP in wetlands

We found FluxCom GPP may be overestimated in wetlands. In *Fen*, FluxCom GPP is substantially higher than EC GPP (Figure 3.2 k) and other non-wetland herbaceous LC types (Figure 3.2). In *Bog* and *Water*, FluxCom GPP is also unrealistically high while SIF_{dc} is around 0. These results suggest a potential overestimation of FluxCom GPP in wetland.

This bias caused by water is more significant in the area with a high fraction of wetlands (Figure 3.2o), where the annual mean and seasonal range of EI are also high (Figure 3.3df).

Topographic impact on the SIF-GPP relationship

There is a topographic dependence of k and Pearson's r^2. k (Pearson's r^2) is higher (lower) along the Brooks Range, the Mackenzie River, the Alaska Range, and the north end of the Rocky Mountains (Figure 3.3abce). Meanwhile, the reduced χ^2 is mostly around 1, which suggests the fitted SIF-GPP relationship is reliable.

The resulting k of *Evergreen Forest* shows a strong dependence on elevation as the dominant LC fraction varies (Figure 3.4a, Funk et al. 2004; Roland et al. 2021). For example, when *Evergreen Forest* becomes more abundant, k is higher between 1000-1500 m in elevation. Above the tree line (~1500m), k drops as the fraction of grid taken by *Evergreen Forest* reduces. The highest k in *Evergreen Forest* is obtained at a 2000 m elevation which can be noisy because the reduced χ^2 is much less than 1 suggesting the linear model overfits the data.

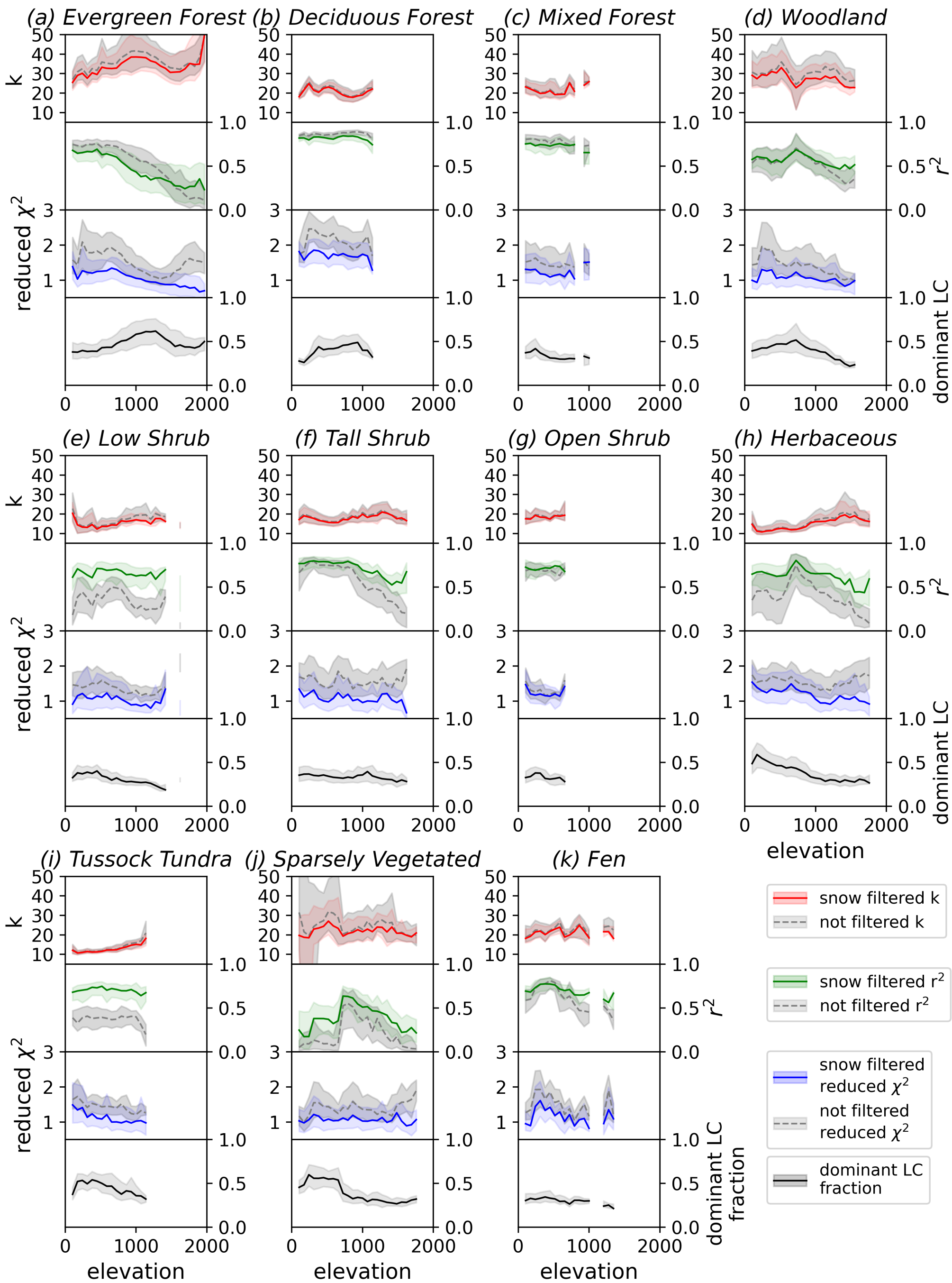

Figure 3.4: The resulting k, Pearson's r^2, reduced χ^2 and the dominant LC fraction categorized by dominant LC types as a function of surface elevation. The color lines are the results from snow free data (snow cover is less than 0.1). The gray dashed lines are the results from snow contaminated data (snow cover is greater than 0.1). The shades are the interquartile range of the results from all grid-time in each dominant LC type. *Bog* has too few grids to show the dependence on elevation. *Barren* and *Water* LC types are omitted since they are not vegetation dominated.

Snow contamination and snow impact on the SIF-GPP relationship

FluxCom GPP is occasionally unrealistically high during winters, when SIF_{dc} is around zero (Figure 3.2). We found that this is a sign of snow contamination, especially in the LC types with lower canopy heights, such as *Low shrub*, *Herbaceous*, and *Tussock Tundra* (Figure 3.2ehi). After snowy pixels were filtered, the distribution of TROPOMI SIF_{dc} and FluxCom GPP is more towards linear.

Although the change in resulting k due to snow filtering is small, snow filtering has substantially improved the goodness of fit by increasing Pearson's r^2 and/or pushing the reduced χ^2 towards 1 across all LC types and all elevations, especially in low-statured LCs, such as *Low shrub*, *Herbaceous*, and *Tussock Tundra* (Figure 3.4ehi) where the split distribution pattern due to snow contamination is observed in Figure 3.4. In forests (Figure 3.4abc), although Pearson's r^2 decreases, the reduced χ^2 has been improved by getting closer to 1.

3.5 Discussion

Opportunities for remotely evaluating photosynthetic phenology in the Arctic-Boreal region

We reported and evaluated the SIF-GPP relationship in the context of Arctic-Boreal LC types at the regional scale. The extensive spatial coverage of our study and validation from EC GPP and tower-based SIF data underscores the potential of using remote sensing and machine learning techniques in the Arctic-Boreal region if remote sensing data are carefully filtered for snow contamination.

Benefiting from the extensive spatial coverage, FluxCom GPP and TROPOMI SIF fill the gaps in LC types that are too remote to be extensively sampled by ground-based measurements (Virkkala et al., 2022) or in complex terrain where eddy-covariance techniques are challenging to apply (Baldocchi, 2003; Paw U et al., 2000). However, large uncertainties are still associated with limited training data. Our study provided both Pearson's r^2 and reduced χ^2 to help biosphere modelers use the resulting k judiciously considering the uncertainty.

The heterogeneous LC and complex terrain in the Arctic-Boreal region further complicate the interpretation of the fitted SIF-GPP relationship and resulting k values. Even though the dominant LC types are unchanged, the elevational gradient of sub-pixel LC contributes to the uncertainties in the relationship of SIF_{dc} and GPP among the pixels of the same dominant LC types.

Overall, remote sensing and machine learning techniques provided extensive spatial coverage of SIF_{dc} and GPP in our study. We found it is challenging to find a universal k or a one-model-fits-all approach to estimate GPP using SIF_{dc} in the Arctic-Boreal region, especially across multiple LC types or even within the same dominant LC types. For future studies, comprehensive sampling of the physiological traits (such as LUE, Φ_F, and f_{esc}; Equation 3.4) across LCs can help mechanistically explain the difference in k.

k values across latitudes

In low-statured LC types including *Low Shrub*, *Herbaceous*, and *Tussock Tundra*, the k values in this study are similar to the k values for grassland in Turner et al. (2021).

In high-statured LC types, our k values are largely different from the k values in other studies fortemperate regions derived from EC GPP (Liu et al., 2022; Turner et al., 2021). For example, the average k value of *Evergreen Forest* in our results is 33.84 (gC m^{-2} day^{-1})/(mW m^{-2} sr^{-1} nm^{-1}), while the k value of *Evergreen Forest* is less than 20 (gC m^{-2} day^{-1})/(mW m^{-2} sr^{-1} nm^{-1}) in the continental US (Turner et al., 2021) or globally (Liu et al., 2022).

On the other hand, the reported k is closer to Liu et al. (2020) (22.9±2.6 (gC m^{-2} day^{-1})/(mW m^{-2} sr^{-1} nm^{-1})) and Sun et al. (2018) (27.43 (gC m^{-2} day^{-1})/(mW m^{-2} sr^{-1} nm^{-1})) for boreal evergreen forests, both of which have used FluxCom GPP.

If FluxCom GPP can accurately represent the seasonal trajectory of EC GPP, the disagreement in k of the same LC types across latitudes may indicate different vegetation composition, photosynthetic productivity, fluorescence yield, sub-pixel variability across latitudes, and/or canopy openness (Crous et al., 2022; Kreyling, 2020; Prock and Körner, 1996) as suggested in Equation 3.4. However, we found that FluxCom GPP can be biased, which will be discussed next.

Limitations in FluxCom GPP

Snow contamination

Although the original FluxCom GPP product has already removed some snowy pixels by using MODIS quality flags (Jung et al., 2020), we found some snow contamination still exists (Figure 3.2). In this study, we used a more conservative snow filter (<0.1) to showcase the snow contamination in FluxCom GPP propagated from remote sensing products (Jin et al., 2017; Myers-Smith et al., 2020). More importantly, our results suggest that quantitative and standalone information on snow coverage in addition to quality flags is helpful for improving future machine learning products (Chen et al., 2018).

Snow contamination does not impact all LC types equally. Low-statured LC types are more likely to have unrealistically high FluxCom GPP before the growing season starts (Figure 3.2). Thus, the universal snow filter we used in this study may be too conservative. For future studies, rigorous validation of snow measurements at regional scales will greatly improve canopy radiative transfer simulations and optical remote sensing retrievals at the Arctic-Boreal region (Chen et al., 2018; Kobayashi and Iwabuchi, 2008; Kobayashi et al., 2007).

Underrepresented water

Contrary to attributing the high k values in wetlands to underestimated SIF Chen et al. (2021), our results suggest the unrealistically high FluxCom GPP is the reason for high k values in wetland LC types. FluxCom GPP has been overestimated because NDVI of water surface in mixed pixels with both vegetation and water surface is understated (Jiang et al., 2005, 2006). Using near-infrared reflectance of vegetation (NIRv) for FluxCom models may better account for the dark surface water reflectance than NDVI and improve the SIF-GPP relationship (Badgley et al., 2019).

This bias further compounds the uncertainty due to a lack of sampling as high EI and high wetland area fractions collocate. Taken together, these two issues can limit the application of FluxCom GPP in the Arctic-Boreal region (Figure 3.2o; Muster et al. 2013; Stow et al. 2004).

Extrapolation of training data

Because the spread in FluxCom GPP ensembles may not fully represent the disagreement between FluxCom and EC GPP when there are few EC towers as training samples for FluxCom (Pallandt et al., 2022), the resulting k values may be more reliable where FluxCom and EC GPP are similar (such as *Tussock Tundra* and *Low Shrub*; Figure 3.2ei) than the ones where the FluxCom GPP is substantially overestimated (such as *Evergreen Forest* and *Fen*; Figure 3.2ak).

Nevertheless, there is a time mismatch between FluxCom GPP and EC GPP (Table 3.1) in this study, where the inter-annual variability of GPP seasonality is ignored.

More active EC towers with continuous and high-quality GPP products are needed in future studies.

Heterogeneous sub-pixel LC

We showed that LC in the Arctic-Boreal region is highly heterogeneous at sub-pixel. The dominant vegetated LC types on average occupy less than 50% of the area in each 0.08333°× 0.08333°grid (Figure 3.1b). It is challenging to unmix the contribution of subpixel LC types at the current spatial scale. This results in a few notable limitations in our study: 1) The LC definitions of EC towers are different according to 30-m vicinity (LC30M), 0.08333°vicinity (LC008333D), and the actual footprint of towers based on PI's descriptions (tower footprint LC in table 3.1). As a result, there may be a mismatch of LC types when we benchmark the FluxCom GPP with EC GPP. 2) As discussed in Sect. 3.5, the presence of surface water contributes to the sub-pixel variations in other dominant LC types and adds to the ambiguity of our results (Myers-Smith et al., 2020). 3) The LC definition used here does not consider agricultural land cover, which is not negligible in southern Alberta and Saskatchewan (Guanter et al., 2014) and yields a different SIF-GPP relationship than the non-agriculture land cover types. And 4) given the rapid changes in the Arctic-Boreal region (Box et al., 2019; Canadell et al., 2021; Curasi et al., 2022; Hobbie et al., 2017), our LC information from 2014 (Wang et al., 2019) can be outdated, which will impact our definition of dominant LC types and the classification of results.

3.6 Conclusions

In this study, we evaluated the empirical linear relationship of SIF_{dc} and GPP across the Arctic-Boreal region from the perspectives of Pearson's r^2 and the goodness of fit. Our results show the promise of monitoring Arctic-Boreal vegetation using novel remote sensing tools after careful quality control. For the first time, our study reports the fitted regression slope k as well as the uncertainties of fitted SIF_{dc}-GPP relationship for the land cover types that are unique to the Arctic-Boreal region. The resulting k, Pearson's r^2, and reduced χ^2 together can help biosphere modelers improve the estimation of GPP in the Arctic-Boreal regions and cope with model-data uncertainties.

3.7 Acknowledgement

This research is supported by the NASA ABoVE (award 80NSSC19M0129) and OCO Science team projects (award 80NSSC18K0895). This material is also based upon work supported by the National Science Foundation Graduate Research Fellowship under Grant No. DGE-1650604 and DGE-2034835. We use a Julia gridding package from `https://github.com/cfranken/gridding`. All resulting data from the regression analysis and the climatology of EC tower data can be downloaded from https://data.caltech.edu/records/20216.

Bibliography

G. Badgley, L. D. L. Anderegg, J. A. Berry, and C. B. Field. Terrestrial gross primary production: Using NIR $_V$ to scale from site to globe. *Global Change Biology*, 25 (11):3731–3740, November 2019. ISSN 1354-1013, 1365-2486. doi: 10.1111/gcb.14729. URL `https://onlinelibrary.wiley.com/doi/10.1111/gcb.14729`.

D. D. Baldocchi. Assessing the eddy covariance technique for evaluating carbon dioxide exchange rates of ecosystems: past, present and future: CARBON BALANCE and EDDY COVARIANCE. *Global Change Biology*, 9(4):479–492, April 2003. ISSN 13541013. doi: 10.1046/j.1365-2486.2003.00629.x. URL `http://doi.wiley.com/10.1046/j.1365-2486.2003.00629.x`.

C. Beer, M. Reichstein, E. Tomelleri, P. Ciais, M. Jung, N. Carvalhais, C. Rödenbeck, M. A. Arain, D. Baldocchi, G. B. Bonan, A. Bondeau, A. Cescatti, G. Lasslop, A. Lindroth, M. Lomas, S. Luyssaert, H. Margolis, K. W. Oleson, O. Roupsard, E. Veenendaal, N. Viovy, C. Williams, F. I. Woodward, and D. Papale. Terrestrial Gross Carbon Dioxide Uptake: Global Distribution and Covariation with Climate. *Science*, page 1184984, July 2010. ISSN 0036-8075, 1095-9203. doi: 10.1126/science.1184984. URL `http://science.sciencemag.org/content/early/2010/07/05/science.1184984`.

T. A. Black. FLUXNET2015 CA-Obs Saskatchewan - Western Boreal, Mature Black Spruce, 2016. URL `https://www.osti.gov/servlets/purl/1440044/`. Type: dataset.

P. T. Boggs, J. E. Rogers, and R. B. Schnabel. User's reference guide for odrpack version 2.01: Software for weighted orthogonal distance regression. 1992.

D. R. Bowling, B. A. Logan, K. Hufkens, D. M. Aubrecht, A. D. Richardson, S. P. Burns, W. R. L. Anderegg, P. D. Blanken, and D. P. Eiriksson. Limitations to winter and spring photosynthesis of a Rocky Mountain subalpine forest. *Agricultural and Forest Meteorology*, 252:241–255, 2018. Publisher: Elsevier.

J. E. Box, W. T. Colgan, T. R. Christensen, N. M. Schmidt, M. Lund, F.-J. W. Parmentier, R. Brown, U. S. Bhatt, E. S. Euskirchen, V. E. Romanovsky, and others. Key indicators of Arctic climate change: 1971–2017. *Environmental Research Letters*, 14(4):045010, 2019. Publisher: IOP Publishing.

H. H. Bruun, J. Moen, R. Virtanen, J.-A. Grytnes, L. Oksanen, and A. Angerbjörn. Effects of altitude and topography on species richness of vascular plants, bryophytes and lichens in alpine communities. *Journal of Vegetation Science*, 17 (1):37–46, February 2006. ISSN 1100-9233, 1654-1103. doi: 10.1111/j.1654-1103.2006.tb02421.x. URL https://onlinelibrary.wiley.com/doi/10.1111/j.1654-1103.2006.tb02421.x.

J. Canadell, J. G., P. M. S. Monteiro, and M. H. Costa. Global Carbon and other Biogeochemical Cycles and Feedbacks. In *Climate Change 5 2021: The Physical Science Basis. Contribution of Working Group I to the Sixth Assessment Report of the 6 Intergovernmental Panel on Climate Change*, volume In Press. Cambridge University Press, August 2021.

A. Chen, J. Mao, D. Ricciuto, D. Lu, J. Xiao, X. Li, P. E. Thornton, and A. K. Knapp. Seasonal changes in GPP/SIF ratios and their climatic determinants across the Northern Hemisphere. *Global Change Biology*, 27(20):5186–5197, October 2021. ISSN 1354-1013, 1365-2486. doi: 10.1111/gcb.15775. URL https://onlinelibrary.wiley.com/doi/10.1111/gcb.15775.

N. Chen, W. Li, C. Gatebe, T. Tanikawa, M. Hori, R. Shimada, T. Aoki, and K. Stamnes. New neural network cloud mask algorithm based on radiative transfer simulations. *Remote Sensing of Environment*, 219:62–71, December 2018. ISSN 00344257. doi: 10.1016/j.rse.2018.09.029. URL https://linkinghub.elsevier.com/retrieve/pii/S0034425718304474.

R. Cheng, T. S. Magney, D. Dutta, D. R. Bowling, B. A. Logan, S. P. Burns, P. D. Blanken, K. Grossmann, S. Lopez, A. D. Richardson, and others. Decomposing reflectance spectra to track gross primary production in a subalpine evergreen forest. *Biogeosciences*, 17(18):4523–4544, 2020. Publisher: Copernicus GmbH.

J. Cihlar. Identification of contaminated pixels in AVHRR composite images for studies of land biosphere. *Remote Sensing of Environment*, 56(3):149–163, June 1996. ISSN 00344257. doi: 10.1016/0034-4257(95)00190-5. URL https://linkinghub.elsevier.com/retrieve/pii/0034425795001905.

K. Y. Crous, J. Uddling, and M. G. De Kauwe. Temperature responses of photosynthesis and respiration in evergreen trees from boreal to tropical latitudes. *New Phytologist*, 234(2):353–374, April 2022. ISSN 0028-646X, 1469-8137. doi: 10.1111/nph.17951. URL https://onlinelibrary.wiley.com/doi/10.1111/nph.17951.

S. R. Curasi, N. Fetcher, R. E. Hewitt, P. M. Lafleur, M. M. Loranty, M. C. Mack, J. L. May, I. H. Myers-Smith, S. M. Natali, S. F. Oberbauer, T. C. Parker, O. Sonnentag,

S. A. Vargas Zesati, S. D. Wullschleger, and A. V. Rocha. Range shifts in a foundation sedge potentially induce large Arctic ecosystem carbon losses and gains. *Environmental Research Letters*, 17(4):045024, April 2022. ISSN 1748-9326. doi: 10.1088/1748-9326/ac6005. URL https://iopscience.iop.org/article/10.1088/1748-9326/ac6005.

E. R. Delaria, B. K. Place, A. J. Turner, Q. Zhu, X. Jin, and R. C. Cohen. Development of a Solar-Induced FluorescenceCanopy Conductance Model and Its Application to Stomatal Reactive Nitrogen Deposition. *ACS Earth and Space Chemistry*, 5(12):3414–3428, December 2021. ISSN 2472-3452, 2472-3452. doi: 10.1021/acsearthspacechem.1c00260. URL https://pubs.acs.org/doi/10.1021/acsearthspacechem.1c00260.

S. Z. Dobrowski. A climatic basis for microrefugia: the influence of terrain on climate: A CLIMATIC BASIS FOR MICROREFUGIA. *Global Change Biology*, 17(2):1022–1035, February 2011. ISSN 13541013. doi: 10.1111/j.1365-2486.2010.02263.x. URL https://onlinelibrary.wiley.com/doi/10.1111/j.1365-2486.2010.02263.x.

Earth Resources Observation And Science (EROS) Center. Global 30 Arc-Second Elevation (GTOPO30), 2017. URL https://www.usgs.gov/centers/eros/science/usgs-eros-archive-digital-elevation-global-30-arc-second-elevation-gtopo30?qt-science_center_objects=0#qt-science_center_objects. Type: dataset.

E. Euskirchen. AmeriFlux AmeriFlux US-BZS Bonanza Creek Black Spruce, 2021a. URL https://www.osti.gov/servlets/purl/1756434/. Type: dataset.

E. Euskirchen. AmeriFlux AmeriFlux US-BZF Bonanza Creek Rich Fen, 2021b. URL https://www.osti.gov/servlets/purl/1756433/. Type: dataset.

E. Euskirchen. AmeriFlux AmeriFlux US-BZB Bonanza Creek Thermokarst Bog, 2021c. URL https://www.osti.gov/servlets/purl/1773401/. Type: dataset.

E. Euskirchen, G. Shaver, and S. Bret-Harte. AmeriFlux AmeriFlux US-ICt Imnavait Creek Watershed Tussock Tundra, 2016a. URL https://www.osti.gov/servlets/purl/1246131/. Type: dataset.

E. Euskirchen, G. Shaver, and S. Bret-Harte. AmeriFlux AmeriFlux US-ICs Imnavait Creek Watershed Wet Sedge Tundra, 2016b. URL https://www.osti.gov/servlets/purl/1246130/. Type: dataset.

E. Euskirchen, G. Shaver, and S. Bret-Harte. AmeriFlux AmeriFlux US-ICh Imnavait Creek Watershed Heath Tundra, 2016c. URL https://www.osti.gov/servlets/purl/1246133/. Type: dataset.

J. B. Fisher, M. Sikka, W. C. Oechel, D. N. Huntzinger, J. R. Melton, C. D. Koven, A. Ahlström, M. A. Arain, I. Baker, J. M. Chen, P. Ciais, C. Davidson, M. Dietze, B. El-Masri, D. Hayes, C. Huntingford, A. K. Jain, P. E. Levy, M. R. Lomas, B. Poulter, D. Price, A. K. Sahoo, K. Schaefer, H. Tian, E. Tomelleri, H. Verbeeck, N. Viovy, R. Wania, N. Zeng, and C. E. Miller. Carbon cycle uncertainty in the Alaskan Arctic. *Biogeosciences*, 11(15):4271–4288, August 2014. ISSN 1726-4189. doi: 10.5194/bg-11-4271-2014. URL `https://bg.copernicus.org/articles/11/4271/2014/`.

D. W. Funk, L. E. Noel, and A. H Freedman. Environmental gradients, plant distribution, and species richness in arctic salt marsh near Prudhoe Bay, Alaska. *Wetlands Ecology and Management*, 12(3):215–233, June 2004. ISSN 0923-4861. doi: 10.1023/B:WETL.0000034074.81373.65. URL `http://link.springer.com/10.1023/B:WETL.0000034074.81373.65`.

N. Gorelick, M. Hancher, M. Dixon, S. Ilyushchenko, D. Thau, and R. Moore. Google Earth Engine: Planetary-scale geospatial analysis for everyone. *Remote Sensing of Environment*, 202:18–27, December 2017. ISSN 00344257. doi: 10.1016/j.rse.2017.06.031. URL `https://linkinghub.elsevier.com/retrieve/pii/S0034425717302900`.

L. Guanter, Y Zhang, M. Jung, J. Joiner, M. Voigt, J. A. Berry, C. Frankenberg, A. R. Huete, P. Zarco-Tejada, J.-E. Lee, M. S. Moran, G. Ponce-Campos, C. Beer, G. Camps-Valls, N. Buchmann, D. Gianelle, K. Klumpp, A. Cescatti, J. Baker, and T. J. Griffis. Global and time-resolved monitoring of crop photosynthesis with chlorophyll fluorescence. *Proceedings of the National Academy of Sciences*, 111 (14), April 2014. ISSN 0027-8424, 1091-6490. doi: 10.1073/pnas.1320008111. URL `https://pnas.org/doi/full/10.1073/pnas.1320008111`.

S. C. Hagen, B. H. Braswell, E. Linder, S. Frolking, A. D. Richardson, and D. Y. Hollinger. Statistical uncertainty of eddy flux–based estimates of gross ecosystem carbon exchange at Howland Forest, Maine. *Journal of Geophysical Research*, 111(D8):D08S03, 2006. ISSN 0148-0227. doi: 10.1029/2005JD006154. URL `http://doi.wiley.com/10.1029/2005JD006154`.

D. K. Hall and G. A. Riggs. MODIS/Terra Snow Cover 8-Day L3 Global 0.05Deg CMG, Version 61, 2021. URL `https://nsidc.org/data/MOD10C2/versions/61`. Type: dataset.

J. E. Hobbie, G. R. Shaver, E. B. Rastetter, J. E. Cherry, S. J. Goetz, K. C. Guay, W. A. Gould, and G. W. Kling. Ecosystem responses to climate change at a Low Arctic and a High Arctic long-term research site. *Ambio*, 46(S1):160–173, February 2017. ISSN 0044-7447, 1654-7209. doi: 10.1007/s13280-016-0870-x. URL `http://link.springer.com/10.1007/s13280-016-0870-x`.

Z. Jiang, Y. Chen, J. Li, and W. Dou. The impact of spatial resolution on NDVI over heterogeneous surface. In *Proceedings. 2005 IEEE International Geoscience and*

Remote Sensing Symposium, 2005. IGARSS '05., volume 2, pages 1310–1313, July 2005. doi: 10.1109/IGARSS.2005.1525361. ISSN: 2153-7003.

Z. Jiang, A. R. Huete, J. Chen, Y. Chen, J. Li, G. Yan, and X. Zhang. Analysis of NDVI and scaled difference vegetation index retrievals of vegetation fraction. *Remote Sensing of Environment*, 101(3):366–378, April 2006. ISSN 0034-4257. doi: 10.1016/j.rse.2006.01.003. URL https://www.sciencedirect.com/science/article/pii/S0034425706000290.

H. Jin, A. M. Jönsson, K. Bolmgren, O. Langvall, and L. Eklundh. Disentangling remotely-sensed plant phenology and snow seasonality at northern Europe using MODIS and the plant phenology index. *Remote Sensing of Environment*, 198:203–212, September 2017. ISSN 0034-4257. doi: 10.1016/j.rse.2017.06.015. URL https://www.sciencedirect.com/science/article/pii/S0034425717302742.

M. Jung, C. Schwalm, M. Migliavacca, S. Walther, G. Camps-Valls, S. Koirala, P. Anthoni, S. Besnard, P. Bodesheim, N. Carvalhais, and others. Scaling carbon fluxes from eddy covariance sites to globe: synthesis and evaluation of the FLUXCOM approach. *Biogeosciences*, 17(5):1343–1365, 2020. Publisher: Copernicus GmbH on behalf of the European Geosciences Union.

T. F. Keenan, M. S. Carbone, M. Reichstein, and A. D. Richardson. The model–data fusion pitfall: assuming certainty in an uncertain world. *Oecologia*, 167(3):587–597, November 2011. ISSN 0029-8549, 1432-1939. doi: 10.1007/s00442-011-2106-x. URL http://link.springer.com/10.1007/s00442-011-2106-x.

H. Kobayashi and H. Iwabuchi. A coupled 1-D atmosphere and 3-D canopy radiative transfer model for canopy reflectance, light environment, and photosynthesis simulation in a heterogeneous landscape. *Remote Sensing of Environment*, 112(1):173–185, January 2008. ISSN 00344257. doi: 10.1016/j.rse.2007.04.010. URL https://linkinghub.elsevier.com/retrieve/pii/S0034425707001873.

H. Kobayashi, R. Suzuki, and S. Kobayashi. Reflectance seasonality and its relation to the canopy leaf area index in an eastern Siberian larch forest: Multi-satellite data and radiative transfer analyses. *Remote Sensing of Environment*, 106(2):238–252, January 2007. ISSN 00344257. doi: 10.1016/j.rse.2006.08.011. URL https://linkinghub.elsevier.com/retrieve/pii/S0034425706003129.

H. Kobayashi, H. Ikawa, and R. Suzuki. AmeriFlux AmeriFlux US-Prr Poker Flat Research Range Black Spruce Forest, 2016. URL https://www.osti.gov/servlets/purl/1246153/. Type: dataset.

J. Kreyling. The Ecological Importance of Winter in Temperate, Boreal, and Arctic Ecosystems in Times of Climate Change. In F. M. Cánovas, U. Lüttge,

C. Leuschner, and M.-C. Risueño, editors, *Progress in Botany Vol. 81*, pages 377–399. Springer International Publishing, Cham, 2020. ISBN 9783030363277. doi: 10.1007/124_2019_35. URL https://doi.org/10.1007/124_2019_35.

P. Köhler, C. Frankenberg, T. S. Magney, L. Guanter, J. Joiner, and J. Landgraf. Global Retrievals of Solar-Induced Chlorophyll Fluorescence With TROPOMI: First Results and Intersensor Comparison to OCO-2. *Geophysical Research Letters*, 45(19):10,456–10,463, October 2018. ISSN 0094-8276, 1944-8007. doi: 10.1029/2018GL079031. URL https://onlinelibrary.wiley.com/doi/abs/10.1029/2018GL079031.

J. Liu, P. O. Wennberg, N. C. Parazoo, Y. Yin, and C. Frankenberg. Observational Constraints on the Response of High-Latitude Northern Forests to Warming. *AGU Advances*, 1(4), December 2020. ISSN 2576-604X, 2576-604X. doi: 10.1029/2020AV000228. URL https://onlinelibrary.wiley.com/doi/10.1029/2020AV000228.

Y. Liu, J. M. Chen, L. He, Z. Zhang, R. Wang, C. Rogers, W. Fan, G. de Oliveira, and X. Xie. Non-linearity between gross primary productivity and far-red solar-induced chlorophyll fluorescence emitted from canopies of major biomes. *Remote Sensing of Environment*, 271:112896, March 2022. ISSN 00344257. doi: 10.1016/j.rse.2022.112896. URL https://linkinghub.elsevier.com/retrieve/pii/S0034425722000104.

J. Loisel, A. V. Gallego-Sala, M. J. Amesbury, G. Magnan, G. Anshari, D. W. Beilman, J. C. Benavides, J. Blewett, P. Camill, D. J. Charman, S. Chawchai, A. Hedgpeth, T. Kleinen, A. Korhola, D. Large, C. A. Mansilla, J. Müller, S. van Bellen, J. B. West, Z. Yu, J. L. Bubier, M. Garneau, T. Moore, A. B. K. Sannel, S. Page, M. Väliranta, M. Bechtold, V. Brovkin, L. E. S. Cole, J. P. Chanton, T. R. Christensen, M. A. Davies, F. De Vleeschouwer, S. A. Finkelstein, S. Frolking, M. Gałka, L. Gandois, N. Girkin, L. I. Harris, A. Heinemeyer, A. M. Hoyt, M. C. Jones, F. Joos, S. Juutinen, K. Kaiser, T. Lacourse, M. Lamentowicz, T. Larmola, J. Leifeld, A. Lohila, A. M. Milner, K. Minkkinen, P. Moss, B. D. A. Naafs, J. Nichols, J. O'Donnell, R. Payne, M. Philben, S. Piilo, A. Quillet, A. S. Ratnayake, T. P. Roland, S. Sjögersten, O. Sonnentag, G. T. Swindles, W. Swinnen, J. Talbot, C. Treat, A. C. Valach, and J. Wu. Expert assessment of future vulnerability of the global peatland carbon sink. *Nature Climate Change*, 11 (1):70–77, January 2021. ISSN 1758-6798. doi: 10.1038/s41558-020-00944-0. URL https://www.nature.com/articles/s41558-020-00944-0.

T. S. Magney, D. R. Bowling, B. A. Logan, K. Grossmann, J. Stutz, P. D. Blanken, S. P. Burns, R. Cheng, M. A. Garcia, P. Khler, and others. Mechanistic evidence for tracking the seasonality of photosynthesis with solar-induced fluorescence. *Proceedings of the National Academy of Sciences*, 116(24):11640–11645, 2019. Publisher: National Acad Sciences.

A. D. McGuire, L. G. Anderson, T. R. Christensen, S. Dallimore, L. Guo, D. J. Hayes, M. Heimann, T. D. Lorenson, R. W. Macdonald, and N. Roulet. Sensitivity of the carbon cycle in the Arctic to climate change. *Ecological Monographs*, 79 (4):523–555, November 2009. ISSN 0012-9615. doi: 10.1890/08-2025.1. URL `http://doi.wiley.com/10.1890/08-2025.1`.

U. Mishra and W. J. Riley. Alaskan soil carbon stocks: spatial variability and dependence on environmental factors. *Biogeosciences*, 9(9):3637–3645, September 2012. ISSN 1726-4189. doi: 10.5194/bg-9-3637-2012. URL `https://bg.copernicus.org/articles/9/3637/2012/`.

S. Muster, B. Heim, A. Abnizova, and J. Boike. Water Body Distributions Across Scales: A Remote Sensing Based Comparison of Three Arctic Tundra Wetlands. *Remote Sensing*, 5(4):1498–1523, March 2013. ISSN 2072-4292. doi: 10.3390/rs5041498. URL `http://www.mdpi.com/2072-4292/5/4/1498`.

I. H. Myers-Smith, J. T. Kerby, G. K. Phoenix, J. W. Bjerke, H. E. Epstein, J. J. Assmann, C. John, L. Andreu-Hayles, S. Angers-Blondin, P. S. A. Beck, L. T. Berner, U. S. Bhatt, A. D. Bjorkman, D. Blok, A. Bryn, C. T. Christiansen, J. H. C. Cornelissen, A. M. Cunliffe, S. C. Elmendorf, B. C. Forbes, S. J. Goetz, R. D. Hollister, R. de Jong, M. M. Loranty, M. Macias-Fauria, K. Maseyk, S. Normand, J. Olofsson, T. C. Parker, F.-J. W. Parmentier, E. Post, G. Schaepman-Strub, F. Stordal, P. F. Sullivan, H. J. D. Thomas, H. Tømmervik, R. Treharne, C. E. Tweedie, D. A. Walker, M. Wilmking, and S. Wipf. Complexity revealed in the greening of the Arctic. *Nature Climate Change*, 10(2):106–117, February 2020. ISSN 1758-678X, 1758-6798. doi: 10.1038/s41558-019-0688-1. URL `http://www.nature.com/articles/s41558-019-0688-1`.

NEON. Bundled data products - eddy covariance (DP4.00200.001): RELEASE-2022, January 2022. URL `https://data.neonscience.org/data-products/DP4.00200.001/RELEASE-2022`. Type: dataset.

W. C. Oechel, C. A. Laskowski, G. Burba, B. Gioli, and A. A. M. Kalhori. Annual patterns and budget of CO_2 flux in an Arctic tussock tundra ecosystem. *Journal of Geophysical Research: Biogeosciences*, 119(3):323–339, March 2014. ISSN 2169-8953, 2169-8961. doi: 10.1002/2013JG002431. URL `https://onlinelibrary.wiley.com/doi/10.1002/2013JG002431`.

M. T. A. Pallandt, J. Kumar, M. Mauritz, E. A. G. Schuur, A.-M. Virkkala, G. Celis, F. M. Hoffman, and M. Göckede. Representativeness assessment of the pan-Arctic eddy covariance site network and optimized future enhancements. *Biogeosciences*, 19(3):559–583, February 2022. ISSN 1726-4189. doi: 10.5194/bg-19-559-2022. URL `https://bg.copernicus.org/articles/19/559/2022/`.

D. Papale, T. A. Black, N. Carvalhais, A. Cescatti, J. Chen, M. Jung, G. Kiely, G. Lasslop, M. D. Mahecha, H. Margolis, L. Merbold, L. Montagnani, E. Moors, J. E. Olesen, M. Reichstein, G. Tramontana, E. Gorsel, G. Wohlfahrt, and

B. Ráduly. Effect of spatial sampling from European flux towers for estimating carbon and water fluxes with artificial neural networks. *Journal of Geophysical Research: Biogeosciences*, 120(10):1941–1957, October 2015. ISSN 2169-8953, 2169-8961. doi: 10.1002/2015JG002997. URL https://onlinelibrary.wiley.com/doi/10.1002/2015JG002997.

K. T. Paw U, D. D. Baldocchi, T. P. Meyers, and K. B. Wilson. Correction Of Eddy-Covariance Measurements Incorporating Both Advective Effects And Density Fluxes. *Boundary-Layer Meteorology*, 97(3):487–511, December 2000. ISSN 1573-1472. doi: 10.1023/A:1002786702909. URL https://doi.org/10.1023/A:1002786702909.

Z. Pierrat and J. Stutz. Tower-based solar-induced fluorescence and vegetation index data for Southern Old Black Spruce forest, January 2022. URL https://zenodo.org/record/5884643. Type: dataset.

Z. Pierrat, T. Magney, N. C. Parazoo, K. Grossmann, D. R. Bowling, U. Seibt, B. Johnson, W. Helgason, A. Barr, J. Bortnik, A. Norton, A. Maguire, C. Frankenberg, and J. Stutz. Diurnal and Seasonal Dynamics of Solar-Induced Chlorophyll Fluorescence, Vegetation Indices, and Gross Primary Productivity in the Boreal Forest. *Journal of Geophysical Research: Biogeosciences*, 127(2), February 2022. ISSN 2169-8953, 2169-8961. doi: 10.1029/2021JG006588. URL https://onlinelibrary.wiley.com/doi/10.1029/2021JG006588.

E. Post, R. B. Alley, T. R. Christensen, M. Macias-Fauria, B. C. Forbes, M. N. Gooseff, A. Iler, J. T. Kerby, K. L. Laidre, M. E. Mann, J. Olofsson, J. C. Stroeve, F. Ulmer, R. A. Virginia, and M. Wang. The polar regions in a 2°C warmer world. *Science Advances*, 5(12):eaaw9883, December 2019. ISSN 2375-2548. doi: 10.1126/sciadv.aaw9883. URL https://www.science.org/doi/10.1126/sciadv.aaw9883.

S. Prock and C. Körner. A Cross-Continental Comparison of Phenology, Leaf Dynamics and Dry Matter Allocation in Arctic and Temperate Zone Herbaceous Plants from Contrasting Altitudes. *Ecological Bulletins*, 45:93–103, 1996. URL https://www.jstor.org/stable/20113187.

H. Riihimäki, J. Heiskanen, and M. Luoto. The effect of topography on arctic-alpine aboveground biomass and NDVI patterns. *International Journal of Applied Earth Observation and Geoinformation*, 56:44–53, April 2017. ISSN 15698432. doi: 10.1016/j.jag.2016.11.005. URL https://linkinghub.elsevier.com/retrieve/pii/S0303243416301908.

A. Rocha, G. Shaver, and John Hobbie. AmeriFlux AmeriFlux US-An3 Anaktuvuk River Unburned, 2016a. URL https://www.osti.gov/servlets/purl/1246144/. Type: dataset.

A. V. Rocha, G. Shaver, and J. Hobbie. AmeriFlux AmeriFlux US-An1 Anaktuvuk River Severe Burn, 2016b. URL https://www.osti.gov/servlets/purl/1246142/. Type: dataset.

C. Roland, J. H. Schmidt, S. E. Stehn, C. J. Hampton-Miller, and E. F. Nicklen. Borealization and its discontents: drivers of regional variation in plant diversity across scales in interior Alaska. *Ecosphere*, 12(5), May 2021. ISSN 2150-8925, 2150-8925. doi: 10.1002/ecs2.3485. URL https://onlinelibrary.wiley.com/doi/10.1002/ecs2.3485.

C. A. Roland, J. H. Schmidt, S .G. Winder, S. E. Stehn, and E. F. Nicklen. Regional variation in interior Alaskan boreal forests is driven by fire disturbance, topography, and climate. *Ecological Monographs*, 89(3), August 2019. ISSN 0012-9615, 1557-7015. doi: 10.1002/ecm.1369. URL https://onlinelibrary.wiley.com/doi/10.1002/ecm.1369.

S. W. Running, R. R. Nemani, F. A. Heinsch, M. Zhao, M. Reeves, and H. Hashimoto. A continuous satellite-derived measure of global terrestrial primary production. *Bioscience*, 54(6):547–560, 2004. Publisher: American Institute of Biological Sciences.

Y. Ryu, J. A. Berry, and D. D. Baldocchi. What is global photosynthesis? History, uncertainties and opportunities. *Remote Sensing of Environment*, 223:95–114, March 2019. ISSN 00344257. doi: 10.1016/j.rse.2019.01.016. URL https://linkinghub.elsevier.com/retrieve/pii/S0034425719300161.

O. Sonnentag. AmeriFlux AmeriFlux CA-SMC Smith Creek, 2021. URL https://www.osti.gov/servlets/purl/1767830/. Type: dataset.

O. Sonnentag and P. Marsh. AmeriFlux AmeriFlux CA-TVC Trail Valley Creek, 2021a. URL https://www.osti.gov/servlets/purl/1767831/. Type: dataset.

O. Sonnentag and P. Marsh. AmeriFlux AmeriFlux CA-HPC Havikpak Creek, 2021b. URL https://www.osti.gov/servlets/purl/1773392/. Type: dataset.

D. A. Stow, A. Hope, D. McGuire, D. Verbyla, J. Gamon, F. Huemmrich, S. Houston, C. Racine, M. Sturm, K. Tape, L. Hinzman, K. Yoshikawa, C. Tweedie, B. Noyle, C. Silapaswan, D. Douglas, B. Griffith, G. Jia, H. Epstein, D. Walker, S. Daeschner, A. Petersen, L. Zhou, and R. Myneni. Remote sensing of vegetation and land-cover change in Arctic Tundra Ecosystems. *Remote Sensing of Environment*, 89(3):281–308, February 2004. ISSN 00344257. doi: 10.1016/j.rse.2003.10.018. URL https://linkinghub.elsevier.com/retrieve/pii/S0034425703002803.

Y. Sun, C. Frankenberg, M. Jung, J. Joiner, L. Guanter, P. Köhler, and T. Magney. Overview of Solar-Induced chlorophyll Fluorescence (SIF) from the Orbiting

Carbon Observatory-2: Retrieval, cross-mission comparison, and global monitoring for GPP. *Remote Sensing of Environment*, 209:808–823, May 2018. ISSN 00344257. doi: 10.1016/j.rse.2018.02.016. URL https://linkinghub.elsevier.com/retrieve/pii/S0034425718300221.

G. Tramontana, K. Ichii, G. Camps-Valls, E. Tomelleri, and D. Papale. Uncertainty analysis of gross primary production upscaling using Random Forests, remote sensing and eddy covariance data. *Remote Sensing of Environment*, 168:360–373, October 2015. ISSN 00344257. doi: 10.1016/j.rse.2015.07.015. URL https://linkinghub.elsevier.com/retrieve/pii/S0034425715300699.

G. Tramontana, M. Jung, C. R. Schwalm, K. Ichii, G. Camps-Valls, B. Ráduly, M. Reichstein, M. A. Arain, A. Cescatti, G. Kiely, L. Merbold, P. Serrano-Ortiz, S. Sickert, S. Wolf, and D. Papale. Predicting carbon dioxide and energy fluxes across global FLUXNET sites with regression algorithms. *Biogeosciences*, 13 (14):4291–4313, July 2016. ISSN 1726-4189. doi: 10.5194/bg-13-4291-2016. URL https://bg.copernicus.org/articles/13/4291/2016/.

A. J. Turner, P. Köhler, T. S. Magney, C. Frankenberg, I. Fung, and R. C. Cohen. Extreme events driving year-to-year differences in gross primary productivity across the US. *Biogeosciences*, 18(24):6579–6588, December 2021. ISSN 1726-4189. doi: 10.5194/bg-18-6579-2021. URL https://bg.copernicus.org/articles/18/6579/2021/.

A.-M. Virkkala, S. M. Natali, B. M. Rogers, J. D. Watts, K. Savage, S. J. Connon, M. Mauritz, E. A. G. Schuur, D. Peter, C. Minions, J. Nojeim, R. Commane, C. A. Emmerton, M. Goeckede, M. Helbig, D. Holl, H. Iwata, H. Kobayashi, P. Kolari, E. López-Blanco, M. E. Marushchak, M. Mastepanov, L. Merbold, F.-J. W. Parmentier, M. Peichl, T. Sachs, O. Sonnentag, M. Ueyama, C. Voigt, M. Aurela, J. Boike, G. Celis, N. Chae, T. R. Christensen, M. S. Bret-Harte, S. Dengel, H. Dolman, C. W. Edgar, B. Elberling, E. Euskirchen, A. Grelle, J. Hatakka, E. Humphreys, J. Järveoja, A. Kotani, L. Kutzbach, T. Laurila, A. Lohila, I. Mammarella, Y. Matsuura, G. Meyer, M. B. Nilsson, S. F. Oberbauer, S.-J. Park, R. Petrov, A. S. Prokushkin, C. Schulze, V. L. St. Louis, E.-S. Tuittila, J.-P. Tuovinen, W. Quinton, A. Varlagin, D. Zona, and V. Zyryanov. The ABCflux database: Arctic–boreal CO₂ flux observations and ancillary information aggregated to monthly time steps across terrestrial ecosystems. *Earth System Science Data*, 14(1):179–208, January 2022. ISSN 1866-3516. doi: 10.5194/essd-14-179-2022. URL https://essd.copernicus.org/articles/14/179/2022/.

J. E. Walsh and B. Brettschneider. Attribution of recent warming in Alaska. *Polar Science*, 21:101–109, September 2019. ISSN 18739652. doi: 10.1016/j.polar.2018.09.002. URL https://linkinghub.elsevier.com/retrieve/pii/S1873965218300872.

S. Walther, M. Voigt, T. Thum, A. Gonsamo, Y Zhang, P. Köhler, M. Jung, A. Varlagin, and Luis Guanter. Satellite chlorophyll fluorescence measurements reveal large-scale decoupling of photosynthesis and greenness dynamics in boreal evergreen forests. *Global Change Biology*, 22(9):2979–2996, September 2016. ISSN 13541013. doi: 10.1111/gcb.13200. URL `https://onlinelibrary.wiley.com/doi/10.1111/gcb.13200`.

S. Walther, L. Guanter, B. Heim, M. Jung, G. Duveiller, A. Wolanin, and T. Sachs. Assessing the dynamics of vegetation productivity in circumpolar regions with different satellite indicators of greenness and photosynthesis. *Biogeosciences*, 15 (20):6221–6256, 2018. Publisher: Copernicus GmbH on behalf of the European Geosciences Union.

J. A. Wang, D. Sulla-Menashe, C.E. Woodcock, O. Sonnentag, R.F. Keeling, and M.A. Friedl. ABoVE: Landsat-derived Annual Dominant Land Cover Across ABoVE Core Domain, 1984-2014, 2019. URL `https://daac.ornl.gov/cgi-bin/dsviewer.pl?ds_id=1691`.

J. A. Wang, D. Sulla-Menashe, C. E. Woodcock, O. Sonnentag, R. F. Keeling, and M. A. Friedl. Extensive land cover change across Arctic–Boreal Northwestern North America from disturbance and climate forcing. *Global Change Biology*, 26(2):807–822, February 2020. ISSN 1354-1013, 1365-2486. doi: 10.1111/gcb.14804. URL `https://onlinelibrary.wiley.com/doi/10.1111/gcb.14804`.

D. Wu, J. C. Lin, H. F. Duarte, V. Yadav, N. C. Parazoo, T. Oda, and E. A Kort. A model for urban biogenic CO₂ fluxes: Solar-Induced Fluorescence for Modeling Urban biogenic Fluxes (SMUrF v1). *Geoscientific Model Development*, 14(6):3633–3661, June 2021. ISSN 1991-9603. doi: 10.5194/gmd-14-3633-2021. URL `https://gmd.copernicus.org/articles/14/3633/2021/`.

G. Wu, K. Guan, C. Jiang, H. Kimm, G. Miao, C. J. Bernacchi, C. E. Moore, E. A. Ainsworth, X. Yang, J. A. Berry, C. Frankenberg, and M. Chen. Attributing differences of solar-induced chlorophyll fluorescence (SIF)-gross primary production (GPP) relationships between two C4 crops: corn and miscanthus. *Agricultural and Forest Meteorology*, 323:109046, August 2022. ISSN 01681923. doi: 10.1016/j.agrformet.2022.109046. URL `https://linkinghub.elsevier.com/retrieve/pii/S0168192322002350`.

T. Wutzler, A. Lucas-Moffat, M. Migliavacca, J. Knauer, K. Sickel, L. Šigut, O. Menzer, and M. Reichstein. Basic and extensible post-processing of eddy covariance flux data with REddyProc. *Biogeosciences*, 15(16):5015–5030, August 2018. ISSN 1726-4189. doi: 10.5194/bg-15-5015-2018. URL `https://bg.copernicus.org/articles/15/5015/2018/`.

J. Xiao, K. J. Davis, N. M. Urban, and K. Keller. Uncertainty in model parameters and regional carbon fluxes: A model-data fusion approach. *Agricultural and*

Forest Meteorology, 189-190:175–186, June 2014. ISSN 01681923. doi: 10.1016/j.agrformet.2014.01.022. URL https://linkinghub.elsevier.com/retrieve/pii/S0168192314000318.

Y. Zeng, G. Badgley, B. Dechant, Y. Ryu, M. Chen, and J. A. Berry. A practical approach for estimating the escape ratio of near-infrared solar-induced chlorophyll fluorescence. *Remote Sensing of Environment*, 232:111209, October 2019. ISSN 0034-4257. doi: 10.1016/j.rse.2019.05.028. URL https://www.sciencedirect.com/science/article/pii/S0034425719302226.

M. Zhao, F. A. Heinsch, R. R. Nemani, and S. W. Running. Improvements of the MODIS terrestrial gross and net primary production global data set. *Remote Sensing of Environment*, 95(2):164–176, March 2005. ISSN 00344257. doi: 10.1016/j.rse.2004.12.011. URL https://linkinghub.elsevier.com/retrieve/pii/S0034425705000106.

D. Zona and W. Oechel. AmeriFlux AmeriFlux US-Ivo Ivotuk, 2016. URL https://www.osti.gov/servlets/purl/1246067/. Type: dataset.

D. Zona, P. M. Lafleur, K. Hufkens, B. Bailey, B. Gioli, G. Burba, J. P. Goodrich, A. K. Liljedahl, E. S. Euskirchen, J. D. Watts, M. Farina, J. S. Kimball, M. Heimann, M. Göckede, M. Pallandt, T. R. Christensen, M. Mastepanov, E. López-Blanco, M. Jackowicz-Korczynski, A. J. Dolman, L. B. Marchesini, R. Commane, S. C. Wofsy, C. E. Miller, D. A. Lipson, J. Hashemi, K. A. Arndt, L. Kutzbach, D. Holl, J. Boike, C. Wille, T. Sachs, A. Kalhori, X. Song, X. Xu, E. R. Humphreys, C. D. Koven, O. Sonnentag, G. Meyer, G. H. Gosselin, P. Marsh, and W. C. Oechel. Earlier snowmelt may lead to late season declines in plant productivity and carbon sequestration in Arctic tundra ecosystems. *Scientific Reports*, 12(1):3986, December 2022. ISSN 2045-2322. doi: 10.1038/s41598-022-07561-1. URL https://www.nature.com/articles/s41598-022-07561-1.

Chapter 4

IMPACT OF RADIATION VARIATIONS ON TEMPORAL UPSCALING OF INSTANTANEOUS SOLAR-INDUCED CHLOROPHYLL FLUORESCENCE

R. Cheng, P. Köhler, and C. Frankenberg. "Impact of radiation variations on temporal upscaling of instantaneous solar-induced chlorophyll fluorescence" (under re-review). In: *Agricultural and Forest Meteorology*.

4.1 Abstract

Solar-Induced Chlorophyll Fluorescence (SIF) has been increasingly used as a novel proxy for vegetation productivity. Several space-borne instruments can retrieve SIF at varying overpass time, which complicates the interpretation as SIF is driven by absorbed Photosynthetically Active Radiation (PAR) at the acquisition time. To facilitate comparisons across sensors, satellite-based SIF is upscaled to daily averages with a length-of-day correction factor (DC). In conventional DC calculations, the light intensity over a day is approximated geometrically by the cosine of the Solar Zenith Angle (SZA), neglecting changes in atmospheric extinction and topographic effects. Here, we use reanalysis PAR data for DC calculations to evaluate the impact of atmospheric extinction and diffuse radiation individually. We find that the simple SZA approach is a reliable approximation for flat surfaces, where the overall atmospheric impact on DC is less than 10% as large individual effects on direct and diffuse PAR partially compensate each other. At longer time-scales, a sampling (clear sky) bias might exist due to cloud-filtering of satellite data. We find that in the Amazon the true monthly mean PAR can be 25% lower than the one for cloud-filtered days, potentially inducing seasonal SIF biases on the same order. An additional factor impacting PAR during a day is topography. For complex terrain, direct light in the DC expression requires a correction for surface slopes. For example in the San Gabriel Mountains, California, USA, the modified DC is changed by as much as 500% for strongly tilted surfaces. This modification is especially important for satellite instruments with fine spatial resolutions, where surface slopes are not averaged out and can have a substantial impact on reflectance and SIF. Overall, our refined DC-corrections and averaging strategy can help satellite SIF interpretation as well as intercomparisons over a wide range of spatio-temporal scales and overpass times.

4.2 Introduction

Photosynthesis is the dominant driver of land-atmosphere carbon exchange with poorly known climate feedbacks (Richardson et al., 2013). Solar-Induced Chlorophyll Fluorescence (SIF) has become a popular proxy for photosynthesis because it is linked to the electron transport rate in the light reactions of photosynthesis (Porcar-Castell et al., 2014). Many studies have used SIF to study photosynthesis on the global scale (Mohammed et al., 2019), including the estimation of gross primary production, canopy water deficit, and crop yield (Gentine and Alemohammad, 2018; He et al., 2020; Zuromski et al., 2018). Global scale studies in particular benefit from space-borne observations of SIF, which are relatively coarse in the spatial domain but a valuable tool for monitoring photosynthesis without requiring sub-pixel homogeneity. As more satellites measure SIF, comparisons across sensors are challenging due to varying times of measurement (t_m).

SIF inferred from satellite measurements (SIF_{t_m}) represents the radiance emitted by chlorophyll that primarily depends on the amount of Absorbed Photosynthetically Active Radiation (APAR) at t_m (Joiner et al., 2020; Magney et al., 2020; Mohammed et al., 2019), which is a product of Photosynthetically Active Radiation (PAR) reaching the canopy at t_m and the fraction of PAR absorbed by the canopy (fPAR). Because PAR varies across ground tracks (Joiner et al., 2020; Köhler et al., 2018) and with satellite orbital parameters, while the diurnal cycle of fPAR is negligible compared to the diurnal cycle of PAR (Lin et al., 2019), SIF_{t_m} is an instantaneous value associated with PAR at t_m. In order to compare SIF across different satellites with various t_m (Zhang et al., 2018), studies (Frankenberg et al., 2011; Hu et al., 2018; Köhler et al., 2018; Zhang et al., 2018) have to scale SIF_{t_m} to a daily-average SIF ($\mathrm{SIF}_{\mathrm{dc}}$) using a length-of-day correction factor (DC), which is calculated based on the diurnal cycle of PAR under the assumption that SIF scales linearly with PAR:

$$\mathrm{SIF}_{\mathrm{dc}} = \mathrm{SIF}_{t_m} \times \mathrm{DC}\,, \tag{4.1a}$$

$$\mathrm{DC} = \frac{1}{\mathrm{PAR}_{t_m}} \int_{t_m\text{-}12\mathrm{h}}^{t_m+12\mathrm{h}} \mathrm{PAR}_{\mathrm{t}}\, d\mathrm{t}\,. \tag{4.1b}$$

Conventionally, the diurnal cycle of PAR in the calculation of DC (Equation 4.1b) is approximated geometrically by the cosine of Solar Zenith Angle (SZA), denoted as μ (Frankenberg et al., 2011; Köhler et al., 2018). Thus, the derivation of the DC can be simplified to

$$\mathrm{DC}_{\mathrm{SZA}} = \frac{1}{\mu_{t_m}} \int_{t_m\text{-}12\mathrm{h}}^{t_m+12\mathrm{h}} \mu_{\mathrm{t}}\, \mathcal{H}(\mu_{\mathrm{t}})\, d\mathrm{t}\,, \tag{4.2}$$

where $\mathcal{H}$ is the Heaviside step function, i.e. zero for SZAs greater than 90° (nighttime).

This straightforward approach generates $\mathrm{SIF}_{\mathrm{dc}}$ via $\mathrm{DC}_{\mathrm{SZA}}$ without the need to know true PAR as μ_t can simply be computed using ephemeris calculators, which provide the solar geometry at a given location and time based on orbital parameters of the Earth in the solar system. The approximation is thus a simple yet possibly inaccurate proxy for PAR at the top of canopy, as the approach neglects atmospheric effects, e.g. changing cloud, as well as topography (Frankenberg et al., 2011). As there is no detailed quantitative evaluation of the impact of atmospheric absorption and scattering as well as topography on the DC calculation, the potential errors in SIF averages are still hard to assess.

To characterize potential errors in conventional daily-average SIF calculations as well as in temporal (e.g. monthly) averages, we have to consider the following effects, illustrated using simple examples: I) Diurnal atmospheric effects: diurnal cycles in atmospheric conditions (e.g. convective systems building up during a day) can cause biases when using a simple geometric approach and these will depend on the time of measurement; II) Day-to-day atmospheric effects: cloud filtering of satellite data can cause a clear-sky bias in longer-term SIF averages, as the measurements passing the quality filters are more likely obtained during cloud free days; III) Topography effects: topography can create highly asymmetric diurnal PAR cycles, as we have to consider the geometry of a tilted surface with respect to the sun.

Our study aims to quantify these impacts individually so that SIF measurements across sensors and temporal-spatial scales can be better compared and interpreted. In section 4.3, we develop correction models (summarized in Table 4.1) for DC. Using global PAR datasets, solar angle information, detailed topography, and actual SIF soundings, as outlined in Section 4.4, we evaluate the DC calculations in Section 4.5. At the global scale, we highlight areas where temporal upscaling SIF is prone to biases by atmospheric effects and use regional examples to quantify the individual bias in areas with strong seasonal variations in cloud cover (e.g. the Amazon) and complex terrain (e.g. the San Gabriel Mountains).

4.3 Methods

Atmospheric effects

Upscaling $\mathbf{SIF}_{t_m}$ to $\mathbf{SIF}_{\mathbf{dc}}$

Downwelling PAR at the surface can be divided into two components: direct PAR ($\mathrm{PAR}_{\mathrm{direct}}$) and diffuse PAR ($\mathrm{PAR}_{\mathrm{diffuse}}$). $\mathrm{PAR}_{\mathrm{direct}}$ is the transmitted part of the incoming collimated solar beam reaching the surface after being diminished by atmospheric extinction by trace gases, aerosols, and clouds along the light path. Despite its reduced amplitude, $\mathrm{PAR}_{\mathrm{direct}}$ preserves the direction of the incoming PAR, which is represented by the SZA. Because PAR at the top of atmosphere is directly proportional to μ, the difference between the diurnal cycles of $\mathrm{PAR_{direct}}$ and μ results from atmospheric extinction along the light path. Hence, we can evaluate this impact on $\mathrm{SIF_{dc}}$ by comparing $\mathrm{DC_{SZA}}$ with $\mathrm{DC_{direct}}$, which is calculated with actual $\mathrm{PAR_{direct}}$:

$$\mathrm{DC_{direct}} = \frac{1}{\mathrm{PAR}_{\mathrm{direct},t_m}} \times \int_{t_m\text{-12h}}^{t_m\text{+12h}} \mathrm{PAR_{direct,t}}\, d\mathrm{t}. \tag{4.3}$$

$\mathrm{PAR_{diffuse}}$ is constituted by scattered PAR that ultimately reaches the surface. $\mathrm{PAR_{diffuse}}$ can also be the major energy source for photosynthesis when $\mathrm{PAR_{direct}}$ is strongly reduced through atmospheric scattering, e.g. at high latitudes or in areas with frequent cloud cover. Thus, in order to accurately account for changes in total PAR, a comprehensive DC correction factor needs both $\mathrm{PAR_{direct}}$ and $\mathrm{PAR_{diffuse}}$:

$$\begin{aligned}\mathrm{DC_{total}} = {} & \frac{1}{\left(\mathrm{PAR}_{\mathrm{direct},t_m} + \mathrm{PAR}_{\mathrm{diffuse},t_m}\right)} \\ & \times \int_{t_m\text{-12h}}^{t_m\text{+12h}} \left(\mathrm{PAR_{direct,t}} + \mathrm{PAR_{diffuse,t}}\right) d\mathrm{t}.\end{aligned} \tag{4.4}$$

Thus, the difference between $\mathrm{DC_{total}}$ and $\mathrm{DC_{direct}}$ is due to the impact of diffuse light. It is worth noting that plants can use diffuse light more efficiently than direct light (Gu et al., 1999, 2019; Lu et al., 2020), as it is distributed more evenly across all leaves. Here, we neglect this and focus on variations in total PAR, i.e. assume that both $\mathrm{PAR_{direct}}$ and $\mathrm{PAR_{diffuse}}$ have a similar impact on SIF.

To isolate the impact of clouds, we can make use of the fact that meteorological reanalysis data are provided for both all-sky conditions (including all atmospheric effects as modeled) as well as clear sky conditions (providing radiation fields as if no clouds had been present). This allows us to separate the atmospheric effects on $\mathrm{SIF_{dc}}$ for cloud free conditions in Sect. 4.5 and all-sky (i.e. most realistic) conditions in Sect. 4.5. With the help of these globally modeled PAR datasets, we can highlight regions where atmospheric effects are important to consider in $\mathrm{SIF_{dc}}$ with and without clouds.

Upscaling $\mathbf{SIF_{dc}}$ to monthly mean SIF ($\overline{SIF}$)

In addition to scaling biases from the instantaneous SIF signal to a diurnal average, sampling biases can occur when aggregating individual daily averages in time, for instance to monthly scales. Unlike vegetation indices, SIF is not only representing a slowly varying canopy structure but is also driven by highly variable incoming PAR, which is strongly impacted by clouds. As cloudiness is also as a selection criteria for satellite data quality filtering, this can cause potential sampling biases.

Often, monthly-mean SIF ($\overline{\mathrm{SIF}}$) is calculated as the cloud filtered arithmetic mean of $\mathrm{SIF}_{\mathrm{dc}}$ within the temporal averaging window (Badgley et al., 2017; Sun et al., 2018). However, cloud filters preferentially keep samples with low cloud cover, i.e. higher PAR conditions, potentially resulting in a clear sky bias (Badgley et al., 2017; Sun et al., 2018) which can vary seasonally.

Thus, seasonal variations in the number of cloud filtered samples (n) relative to total number of samples (N) can be used as a metric for the potential clear sky bias. In Sect. 4.5, we use statistics from the TROPOspheric Monitoring Instrument (TROPOMI) as well as reanalysis data to investigate when and where globally the clear sky bias is likely to occur.

To quantify the actual clear sky bias, Hu et al. (2021) suggested weighing $\mathrm{SIF}_{\mathrm{dc}}$ by daily mean PAR. Here, we upscale $\mathrm{SIF}_{\mathrm{dc}}$ to $\overline{\mathrm{SIF}}$ using the daily mean all-sky PAR ($\overline{\mathrm{PAR}}_{\mathrm{day}}$) just from measurement days and from all days in a month. Then, the actual clear sky bias is the difference between PAR-weighted $\overline{\mathrm{SIF}}$ and the arithmetic $\overline{\mathrm{SIF}}$, which is defined as

$$\text{PAR-weighted}\,\overline{\mathrm{SIF}} = \frac{1}{N}\sum_{\mathrm{day}=1}^{N}\overline{\mathrm{PAR}}_{\mathrm{day}} \times \frac{1}{n}\sum_{\mathrm{day}=1}^{n}\left(\mathrm{SIF}_{t_m} \times \mathrm{DC}_{\mathrm{total}}\right)_{\mathrm{day}} / \overline{\mathrm{PAR}}_{\mathrm{day}}, \tag{4.5a}$$

$$\text{arithmetic}\,\overline{\mathrm{SIF}} = \frac{1}{n}\sum_{\mathrm{day}=1}^{n}\left(\mathrm{SIF}_{t_m} \times \mathrm{DC}_{\mathrm{total}}\right)_{\mathrm{day}}. \tag{4.5b}$$

In Sect. 4.5, we quantitatively demonstrate the clear sky bias using the Amazon Forests as an example, which exhibits a strong seasonal cycle in cloudiness as well as heavily debated responses of photosynthesis in the dry season (Doughty et al., 2021; Morton et al., 2014; Saleska et al., 2007, 2016; Samanta et al., 2010).

Topographic impact on upscaling SIF_{t_m} to $\mathrm{SIF}_{\mathrm{dc}}$

Adjusting PAR according to topography

Previously, we only discussed atmospheric effects that can bias the scaling from instantaneous to daily average SIF. However, the slope and orientation of the surface can dramatically change the diurnal cycle of received radiation, for example in east or west facing slopes, which can have peak diurnal PAR shifted towards the morning and evening, respectively.

In complex terrain, the diurnal cycle of direct PAR received by a surface is not determined by the SZA but by the angle between the incident direct light and the surface normal (Solar Incidence Angle - SIA, Figure 4.1a). For example, terrain oriented towards the sun (SIA < SZA) receives substantially more direct light per projected unit area. As a result, complex terrain results in spatially heterogeneous total PAR as well as the ratio of $\mathrm{PAR_{diffuse}}$ and $\mathrm{PAR_{direct}}$. This can even lead to spatial variations in hydro-climate conditions that vegetation acclimates to (Bilir et al., 2021; Kutiel, 1992; van der Tol et al., 2007). Therefore, neglecting the topographic impact on PAR can bias $\mathrm{SIF_{dc}}$ as observed from space. Here, we aim to quantify this bias for $\mathrm{SIF_{dc}}$ and validate our correction scheme using reflectances —which are impacted by the same bias— and classical vegetation indices, for which directional effects mostly cancel out.

To evaluate this impact, we add topographic information to the expression of $\mathrm{DC_{total}}$ (Equation 4.4) on a flat surface.

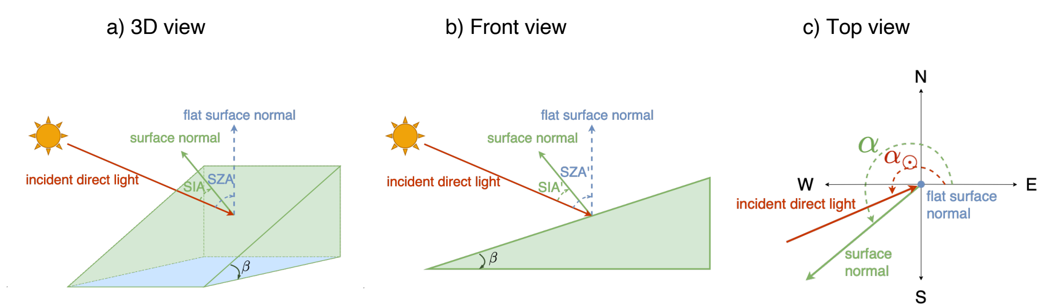

Figure 4.1: The Solar Incidence Angle (SIA) and Solar Zenith Angle (SZA) are not equivalent on a tilted slope as demonstrated in a) a 3D view, b) a front view, and c) a top view. SIA is the angle between the incident direct light and the tilted surface normal. SZA is the angle between the incident direct light and flat surface normal. SIA' and SZA' are the projection of SIA and SZA on the front view, respectively. $\alpha_\odot$, β, and α are solar azimuth angle, surface inclination, and surface azimuth, respectively.

We first correct $\mathrm{PAR_{direct}}$ given the surface inclination angle (β) and azimuth angle (α) using a simple photometric function (Klein, 1977; Teillet et al., 1982):

$$\mathrm{PAR_{direct,DEM,t}} = \mathrm{PAR_{direct,t}} \frac{\cos(\mathrm{SIA})}{\mu_{\mathrm{t}}} \mathcal{H}(\cos(\mathrm{SIA}_t)). \tag{4.6}$$

Given the geometry in Figure 4.1, the SIA can be derived as

$$\mathrm{SIA} = \sin(\mathrm{SZA})\sin(\beta)\cos(\alpha_{\odot}-\alpha)+\mu\cos(\beta) \text{ (Duffie and Beckman, 2013)}\,, \tag{4.7}$$

where $\alpha_{\odot}$ is solar azimuth angle.

We preserve the expression for $\mathrm{PAR_{diffuse}}$ assuming isotropic diffuse PAR, which is less dependent on surface orientation. Here, we only include self-shading (i.e. if the SIA is larger than 90°, no direct radiation reaches the surface) but ignore shading by mountain ranges in the vicinity. Thus, the total PAR projected on a tilted surface is:

$$\mathrm{PAR_{total,DEM,t}} = \mathrm{PAR_{direct,t}}\frac{\cos(\mathrm{SIA})}{\mu_\mathrm{t}}\mathcal{H}(\cos(\mathrm{SIA}_{t_m})) + \mathrm{PAR}_{\mathrm{diffuse},t_m}. \tag{4.8}$$

Validating the topographic adjustment on PAR

To validate this simple topographic adjustment on PAR in Equation 4.8, we make use of the fact that measured reflectances experience the same bias if they are not topographically corrected. However, reflectance ratios are not as affected as the bias cancels out in the ratio. Comparing novel indices that might be susceptible to the topography bias against those that are more robust with respect to slope variations thus provide an indirect validation of our correction approach.

We first apply the adjusted PAR to reflectance (R):

$$\mathrm{R_{DEM}} = \mathrm{R} \times \frac{\mathrm{PAR}_{\mathrm{direct},t_m} + \mathrm{PAR}_{\mathrm{diffuse},t_m}}{\mathrm{PAR}_{\mathrm{direct,DEM},t_m} + \mathrm{PAR}_{\mathrm{diffuse},t_m}}, \tag{4.9}$$

where $\mathrm{R_{DEM}}$ is the topographically corrected R (if the surface slope was neglected during retrievals).

To intuitively interpret the topographic adjustment on PAR, we compare the Vegetation Indices (VIs) built with $\mathrm{R_{DEM}}$ against R in Sect. 4.5. We choose VIs that are proxies for the greenness of canopy, which varies across slopes (Bilir et al., 2021; Kutiel, 1992; van der Tol et al., 2007), such as the Normalized Difference Vegetation Index (NDVI; Silleos et al. 2006), kernel-based NDVI (Camps-Valls et al. 2021), and $\mathrm{NIR_v}$(Badgley et al., 2017):

$$\mathrm{NDVI} = \frac{R_\mathrm{nir} - R_\mathrm{red}}{R_\mathrm{nir} + R_\mathrm{red}}, \tag{4.10a}$$

$$\mathrm{kNDVI} = \tanh(\mathrm{NDVI}^2), \tag{4.10b}$$

$$\mathrm{NIR_v} = \mathrm{NDVI} \times R_\mathrm{nir}. \tag{4.10c}$$

For band-ratio VIs like NDVI and kNDVI, the corrections should be negligible as measured reflected radiance in the red and NIR spectral bands are affected similarly by surface slope changes, because atmospheric scattering is similar in both bands. It is a valid assumption as both bands are spectrally nearby and only mildly impacted (less than 5%; Figure 4.8) by Rayleigh scattering (Bates, 1984).

However, for more complex VIs such as the NIR_v or the Enhanced Vegetation Index (Xiao et al., 2003), the effect of surface slopes does not cancel out. For NIR_v, the effect is directly proportional to the bias in the derived R_{NIR}, which is why we focus on the simple NIR_v correction here, as it provides an analogue to our assumptions for the SIF correction, hence also an indirect validation.

Topographic adjustment on upscaling SIF_{t_m} to SIF_{dc}

The only difference between our topographic correction on R and DC is that the R correction considers PAR at t_m only, while the DC correction requires the full diurnal cycle of PAR. This is because reflectance-based VIs are related to intrinsic properties of the canopy, such as the potential photosynthesis (Badgley et al., 2017; Camps-Valls et al., 2021; Silleos et al., 2006; Xiao et al., 2003).

We derive a Digital Elevation Model (DEM) based length-of-day correction DC_{DEM} as:

$$\begin{aligned} DC_{DEM} = & \frac{1}{\left(PAR_{direct,DEM,t_m} + PAR_{diffuse,t_m}\right)} \\ & \times \int_{t_m\text{-}12h}^{t_m+12h} \left(PAR_{direct,\ DEM,t} + PAR_{diffuse,t}\right) dt. \end{aligned} \tag{4.11}$$

To focus on the topographic impact, we only use clear-sky PAR to explicitly express DC_{DEM}. The difference between DC_{DEM} and DC_{total} reflects the topographic impact on SIF_{dc}

In Sect. 4.5, we use the San Gabriel Mountains in California as an example to evaluate the topographic impact on SIF_{dc} aggregated across various sensor footprints. The strong radiation contrast between north and south facing slopes in the San Gabriel Mountains make this region an ideal study site.

Table 4.1: Summary of all DC models used in this study. A glossary of all variables used in this study is in Sect. 4.8.

DC models	atmospheric effects		topography	equation	results
	direct PAR	diffuse PAR			
DC_{SZA}	✗	✗	✗	4.2	
DC_{direct}	✓	✗	✗	4.3	Sect. 4.5
DC_{total}	✓	✓	✗	4.4	Sect. 4.5
DC_{DEM}	✓	✓	✓	4.11	Sect. 4.5

4.4 Data

Global PAR data

Because there is lack of global-scale ground observation of PAR, we utilize global reanalysis radiation data from the ECMWF ReAnalysis (ERA5), which assimilate various available observations. ERA5 data have been validated independently and enable us to perform a much more thorough analysis than any other dataset (Babar et al., 2019; Urraca et al., 2018; Yang and Bright, 2020). We calculate PAR as a fixed fraction (0.46) of the direct and diffuse surface downwelling shortwave radiation (Howell et al., 1983; Zhang et al., 2020) obtained from ERA5 hourly data in 2020 at $0.5° \times 0.5°$ spatial resolution (Albergel et al., 2018). ERA5 simulates downwelling shortwave radiation at the surface both with clouds (all-sky conditions) and without clouds (clear-sky conditions). In both cases, the ERA5 simulation uses the exact same atmospheric conditions, such as temperature, humidity, ozone, trace gases, and aerosols (Muñoz-Sabater et al., 2021). Therefore, we can differentiate the atmospheric impact under clear-sky and all-sky conditions. The ERA5 variables are listed in 4.8.

For the integrals in the DC expressions (Equations 4.3, 4.4, and 4.11), we interpolate hourly PAR data to 10-min time steps using cubic splines, focusing on land pixels only.

Solar angles

Given t_m, longitude, and latitude of a surface point, Solar Zenith Angle (SZA) and Solar Azimuth Angle ($\alpha_{\odot}$) are calculated using the PyEphem astronomy tool (`https://github.com/brandon-rhodes/pyephem`), which provides the exact Sun-Earth geometry at a given time using orbital characteristics.

We obtain surface elevation (in meters; Figure 4.6a) from the NASA Shuttle Radar Topography Mission (SRTM) version 3 with 30-m spatial resolution (NASA JPL, 2013). The inclination angle (β) and azimuth angle (α) of surface pixels (Figure 4.6b and c) are calculated from the surface elevation using the hill shading algorithm (Horn, 1981) implemented in RichDEM (Barnes, 2016). With SZA, $\alpha_{\odot}$, β, and α, we then calculate SIA using Equation 4.7.

SIF data

We use the TROPOMI SIF data described in Köhler et al. (2018) for our analysis because TROPOMI provides a fine spatial and temporal resolution (Köhler et al., 2018) and a much higher sampling frequency compared to all current satellites that are capable of retrieving SIF. The wide swaths with viewing angles of up to 60° allow for a near-daily global coverage. In this study, we use two levels of processed TROPOMI SIF products: 1) instantaneous SIF from individual soundings; and 2) gridded SIF with a temporal resolution of 16 days and a spatial resolution of 0.0833° × 0.0833°, which is aggregated from individual SIF measurements in 2020. We grid all unfiltered TROPOMI soundings as well as the filtered data with cloud fractions smaller than 0.8, which also includes additional retrieval quality filter criteria and is the suggested standard filter for public use of SIF data (Köhler et al., 2018). We then compute the number of averaged soundings per grid cell in both cloud-filtered (n) and unfiltered (N) cases, the latter of which represents the total number of potential TROPOMI soundings. We then evaluate the measurement yield in each grid, defined as the fraction of measurements that passed the cloud filter (the ratio of n to N), as a function of space and time.

Reflectance data

We use R from LandSat Collection 2 Level 2 data (30-m spatial resolution) on July 3, 2020. The mean LandSat t_m in the San Gabriel Mountains is 10:31 am Local Solar Time (LST) when SZA and $\alpha_{\odot}$ are 22.5° and 335.4°, respectively. The azimuth angle is measured in degrees counter-clockwise from East. Then, the grids of R and surface elevation products are matched and transformed to degrees using the Geospatial Data Abstraction Library (GDAL; `https://gdal.org`), while the 30-m spatial resolution is preserved.

4.5 Results

Here, we discuss the impact of atmospheric variations on DC, both for scaling from instantaneous SIF to daily averages as well as aggregating daily SIF averages to longer-term temporal averages. The impact of topography is discussed separately.

Atmospheric effects

Atmospheric effects on DC under clear-sky conditions

For clear-sky conditions, we first examine the validity of the simple approximation used in DC_{SZA}, where the diurnal cycle of PAR is approximated geometrically by μ. Figure 4.2a shows that the zonal-mean daily integral of $\mu\mathcal{H}(\mu)$ is a smooth function of time and latitude, and the spatiotemporal pattern is consistent with the daily integral of PAR_{direct} computed from ERA5 in Figure 4.2b. The consistency confirms that DC_{SZA} mainly accounts for the diurnal cycle in PAR_{direct}, as expected from a geometric scaling using μ. $PAR_{diffuse}$ is much smaller than PAR_{direct} (Figure 4.2c) in most cases (especially for valid solar angles) and thus has no large impact for clear-sky conditions.

DC_{total} derived from the sum of PAR_{direct} and $PAR_{diffuse}$ (Equation 4.4) is smaller than DC_{SZA} but only by less than 10% assuming a t_m at noon local time (Figure 4.2g). More importantly, the atmospheric impact on DC_{total}/DC_{SZA} (left column in Figure 4.2) is homogeneous across latitudes and seasons, underlining that the simple geometric correction is not creating spatially varying biases. For DC_{direct}/DC_{SZA} (center column in Figure 4.2), the patterns and amplitudes are similar to DC_{total}/DC_{SZA} but have somewhat more absolute variations and spatio-temporal variations. This can only be explained by atmospheric aerosols in ERA5, which can reduce direct and increase diffuse radiation, thus leading to partial compensation in total PAR. Adding $PAR_{diffuse}$ to DC_{direct} has an opposite but smaller impact (Figure 4.2i) since $PAR_{diffuse}$ is larger for longer light paths, which partially cancels out the error from ignoring atmospheric extinction in the SZA approximation of PAR_{direct}. It should be mentioned that although the impact of $PAR_{diffuse}$ can be more extreme at high latitudes during winter, SIF soundings are typically filtered out due to limited light intensity when the SZA at t_m is greater than 80°(regions north or south of the black lines in Figure 4.2d-i).

The magnitude of biases in DC_{SZA}, compared against DC_{total}, depends on t_m as well. The ratio of DC_{total} to DC_{SZA} is less than 5% (Figure 4.2d and j) when t_m is 10 am or 2 pm Local Solar Time (LST). As 10 am and 2 pm are both about two hours away from local solar noon, local PAR is almost identical at these times under clear-sky conditions. Hence, Figures 4.2d-f and Figures 4.2j-l are symmetric. Overall, the errors in the simple DC_{SZA} approach when compared to using ERA5 PAR data (DC_{total}) in clear sky conditions are surprisingly small ($<$ 10%) and can likely be ignored.

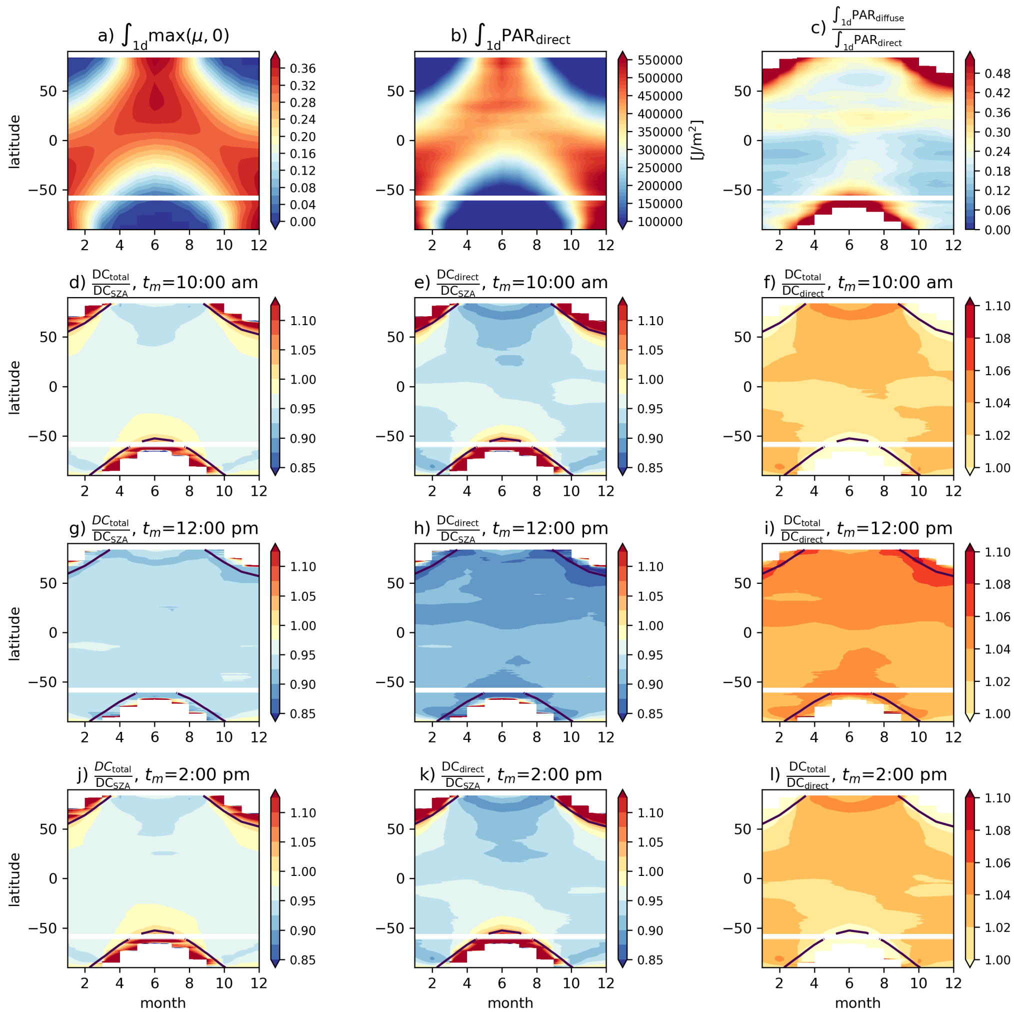

Figure 4.2: The zonal-mean impact of atmospheric extinction and $\mathrm{PAR_{diffuse}}$ on DC calculation under clear-sky conditions. DCs are calculated using clear-sky PAR. Zonal means are calculated from land pixels only. Panels a and b show the daily integral of μ and $\mathrm{PAR_{direct}}$ during daytime. Panel c is the daily integral of $\mathrm{PAR_{diffuse}}$ relative to $\mathrm{PAR_{direct}}$. The ratio of $\mathrm{DC_{total}}$ to $\mathrm{DC_{SZA}}$ (panels d, g, and j) underscores the total impact of atmospheric extinction and $\mathrm{PAR_{diffuse}}$. The ratio of $\mathrm{DC_{direct}}$ to $\mathrm{DC_{SZA}}$ (panels e, h, and k) isolates the impact of atmospheric extinction. The ratio of $\mathrm{DC_{total}}$ to $\mathrm{DC_{direct}}$ (panels f, i, l) isolates the impact of $\mathrm{PAR_{diffuse}}$. Panels d-f assume the overpass time is 10 am Local Solar Time (LST). Panels g-i assume the overpass time is at local noon. Panels j-l assume the overpass time is 2 pm LST. The black lines are the contour of SZA = 80° at t_m. SZA is greater than 80 ° north (south) of the contour in Northern (Southern) Hemisphere.

Atmospheric effects on DC under all-sky conditions

To show the impact of clouds on DC, we repeat the calculations of $\mathrm{DC_{total}}$ and $\mathrm{DC_{direct}}$ as shown before with all-sky conditions. As expected, in all-sky conditions $\mathrm{PAR_{direct}}$

is lower (Figure 4.3b) while $PAR_{diffuse}$ is higher compared to clear-sky conditions. In regions with frequent cloud cover, such as the inter-tropical convergence zone (Figure 4.3c), $PAR_{diffuse}$ can often contribute equally to total PAR. Specifically at high latitudes, $PAR_{diffuse}$ is larger than PAR_{direct} due to longer atmospheric light paths. In contrast, $PAR_{diffuse}$ in the subtropics is smaller because of large-scale atmospheric subsidence, resulting in both a dry climate and less frequent cloud cover.

There is only a little increase in the overall magnitude of DC_{total}/DC_{SZA} under all sky conditions (Figures 4.3d, g, and j) compared to the the clear sky case (Figures 4.2d, g, and j), even in regions with frequent cloud cover. At first, this is surprising as we expected a much stronger bias in DC_{SZA} under cloudy conditions. If we consider direct light only, the DC_{total}/DC_{SZA} variations are in fact much larger, with strong latitudinal and temporal changes (Figures 4.3e, h and k). In regions with the highest discrepancies in DC_{total}/DC_{SZA} , much stronger $PAR_{diffuse}$ due to cloud scattering in all-sky condition contributes more to DC_{total}. As can be seen in Figure 4.3f, i and l, the impact of diffuse light can increase the ratio of DC_{total}/DC_{direct} by up to 30% and counteract the variations in DC_{direct}/DC_{SZA}. Hence, the aggregated atmospheric impact (DC_{total}/DC_{SZA}) is more homogeneous across latitudes and time.

Under all-sky conditions, the atmospheric impact on DC is often larger when t_m is 2 pm (Figure 4.3j-l), because convective systems often forms clouds in the afternoons when the surface is heated. Thus, unlike in the clear-sky case, Figure 4.3d-f and j-i are asymmetric, which can represent an important aspect for comparing satellites with different overpass times.

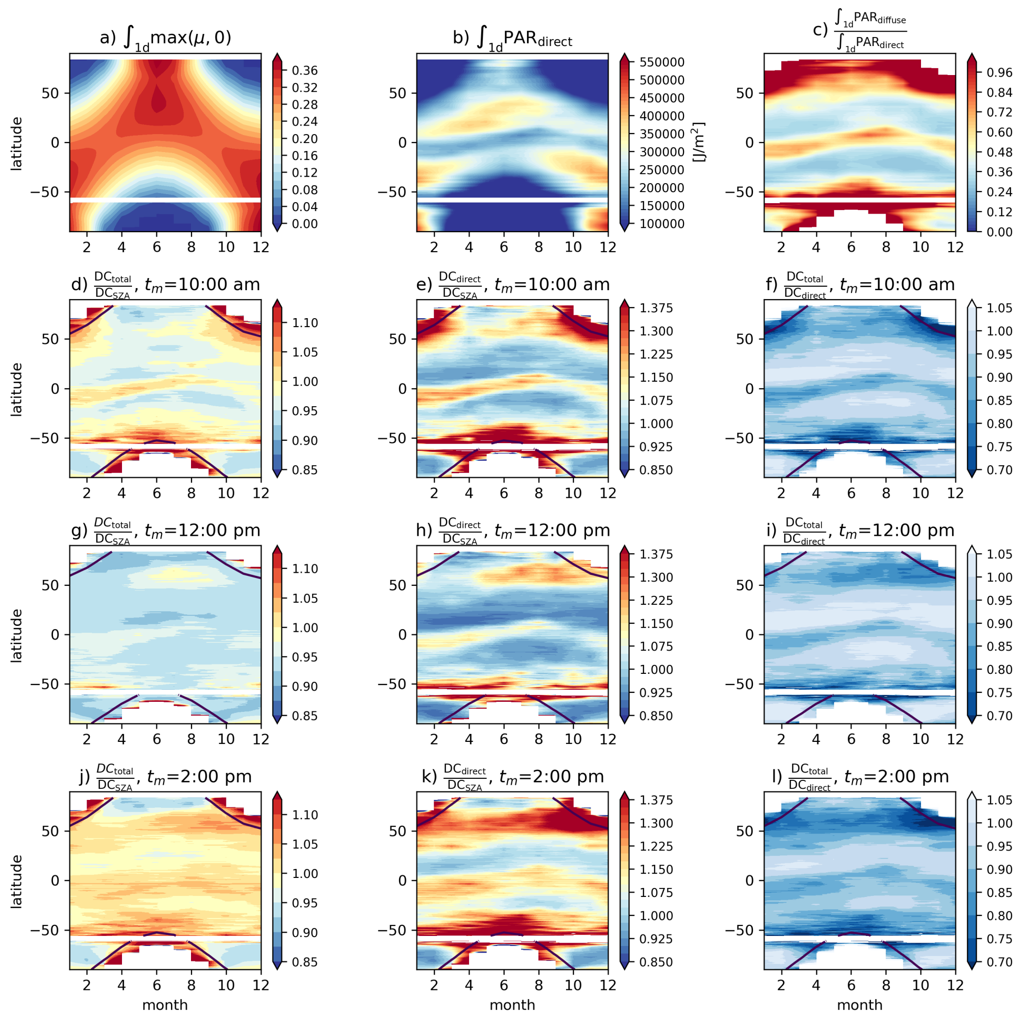

Figure 4.3: The zonal-mean impact of atmospheric extinction and $\mathrm{PAR}_{\mathrm{diffuse}}$ on DC calculation under all-sky conditions. DCs are calculated using all-sky PAR. Zonal means are calculated from land pixels only. Panels a and b show the daily integral of μ and $\mathrm{PAR}_{\mathrm{direct}}$ during daytime. Panel c is the daily integral of $\mathrm{PAR}_{\mathrm{diffuse}}$ relative to $\mathrm{PAR}_{\mathrm{direct}}$. The ratio of $\mathrm{DC}_{\mathrm{total}}$ to $\mathrm{DC}_{\mathrm{SZA}}$ (panels d, g, and j) underscores the total impact of atmospheric extinction and $\mathrm{PAR}_{\mathrm{diffuse}}$. The ratio of $\mathrm{DC}_{\mathrm{direct}}$ to $\mathrm{DC}_{\mathrm{SZA}}$ (panels e, h, and k) isolates the impact of atmospheric extinction. The ratio of $\mathrm{DC}_{\mathrm{total}}$ to $\mathrm{DC}_{\mathrm{direct}}$ (panels f, i, and l) isolates the impact of $\mathrm{PAR}_{\mathrm{diffuse}}$. Panels d-f assume the overpass time is 10 am LST. Panels g-i assume the overpass time is at local noon. Panels j-l assume the overpass time is 2 pm LST. The black lines are the contour of SZA = 80° at t_m. SZA is greater than 80° north (south) of the contour in Northern (Southern) Hemisphere.

Overall, this section highlights counteracting effects of scattering for correcting biases in $\mathrm{DC}_{\mathrm{SZA}}$. In clear-sky conditions, atmospheric extinction dominates the impact on $\mathrm{DC}_{\mathrm{total}}$. In all-sky conditions, $\mathrm{PAR}_{\mathrm{diffuse}}$ becomes more important, specifically in regions with frequent cloud cover. The simple DC_{SZA} approach is a surprisingly good proxy for DC_{total} in both cases, as overall changes in direct and diffuse PAR negatively co-vary, reducing the bias to less than 10% at coarse spatial and temporal scales.

Effects of cloud filtering on ($\overline{SIF}$) and clear sky biases

When using real satellite data for SIF, we have to take into account that a clear sky sampling bias might exist, which can vary seasonally. Based on reanalysis data, we can evaluate the potential impact and identify regions in which seasonal biases can be most prominent.

Spatial patterns of potential clear sky biases

At the global scale, the measurement yield (n/N) varies spatially and seasonally. The highest seasonal dynamic range in measurement yields occurs in regions with strong seasonal cycles of cloudiness, such as regions with monsoon climate including the Amazon, South of the Sahel, India, and North Australia (stippled area in Figure 4.4, indicating > 40% seasonal variations in data yield). These regions with large seasonal variation in SIF measurement yields are potentially subject to seasonally varying clear sky biases.

For high latitudes and non-vegetated areas, such as over ice and desert, the SIF measurement yield is the lowest (Figure 4.4) due to high SZAs during the shoulder seasons and polar nights (Figure 4.13). However, the sampling rate during summer months is much better (Figure 4.14) thanks to overlapping ground tracks (incomplete daily coverage occurs between +/- 7deg). These changes in measurement yield at high latitudes are mostly driven by the SZA cutoff and radiance thresholds, and hence are less prone to clear-sky biases.

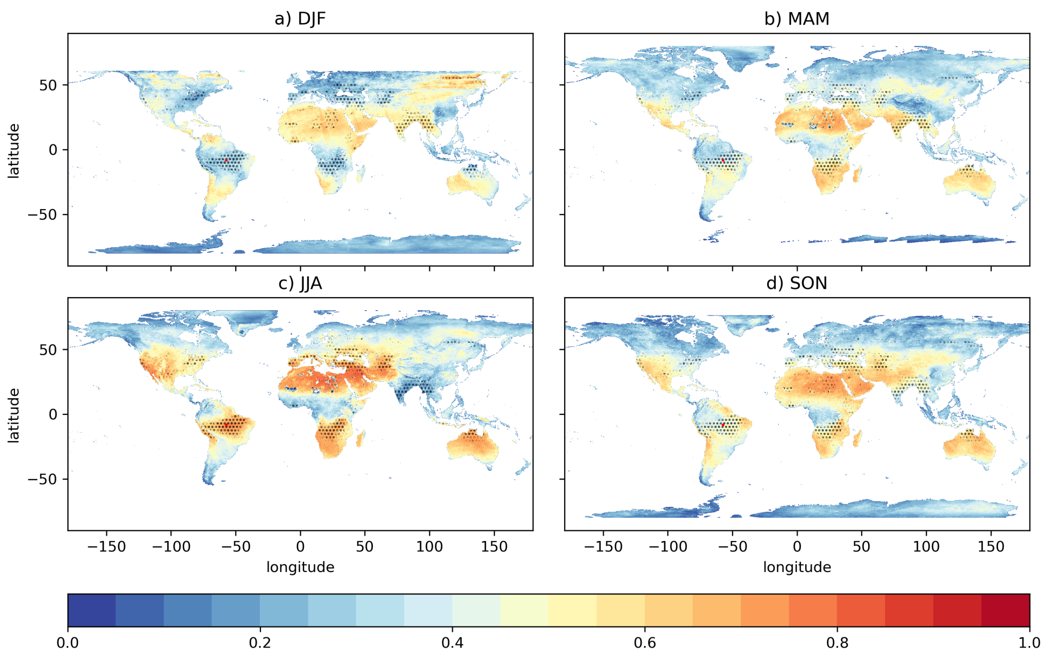

Figure 4.4: The seasonal mean measurement yield of SIF soundings, defined as the fraction of measurements that passed the cloud filter (cloud fraction < 0.8), in a) December, January, and February; b) March, April, and May; c) June, July, and August; and d) September, October, and November. The stippled areas are where the absolute difference between a) and c) is larger than 40%. The red star in the Amazon is the location with regional maximum absolute difference between a) and c).

Quantitative clear sky bias in SIF seasonality

How large can the clear sky bias actually be over different seasons? Here, we demonstrate the impact of clouds on the SIF seasonality using the Amazon as an example. We use individual TROPOMI measurements falling into a 0.25° ×0.25° box around the location of the red star in Figure 4.5a, a region with highly varying data yields (2.75° N, 55.5° W) from March, 2018 to October 2020. The measurement yield can decrease by up to 60% (Figure 4.4 and Figure 4.5b) during the wet season (shaded periods in Figure 4.5a) as fewer soundings pass the cloud filter. PAR-weighted $\overline{\mathrm{SIF}}$ is about 25% smaller than the arithmetic mean (Figure 4.5c), indicating that $\overline{\mathrm{SIF}}$ may be overestimated during periods of frequent cloud cover. Compared to biases in DC, the clear sky bias of $> 10\%$ can thus be substantial. The overestimation is more significant when fewer filtered soundings are available.

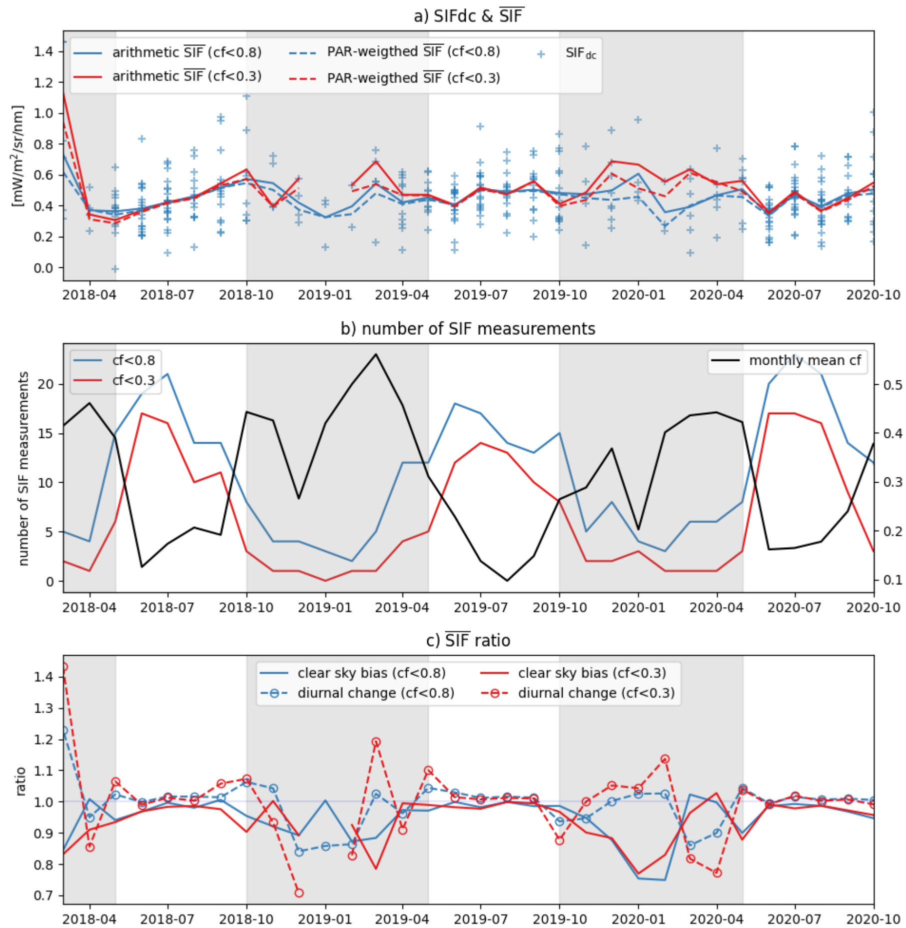

Figure 4.5: Impact of clear sky biases on the seasonality of SIF. In panel a, the scatters are the SIF_{dc} of individual soundings, and the lines are arithmetic (solid) and PAR-weighted (dashed) monthly mean SIF ($\overline{\mathrm{SIF}}$) filtered by the Cloud Fraction (cf) of 0.8 (blue) and 0.3 (red). Panel b demonstrates the number of SIF measurements filtered by the two cf values, while the black curve is the monthly mean cf. The solid lines in panel c compare the ratio of PAR-weighted $\overline{\mathrm{SIF}}$ to arithmetic $\overline{\mathrm{SIF}}$ by the two cloud filters. Panel c also compares the impacts of the clear sky bias (solid lines) and diurnal changes in cloudiness discussed in Sect. 4.5.3 (dashed lines with circles). The impact of clear sky bias is defined as the ratio of PAR-weighted $\overline{\mathrm{SIF}}$ to arithmetic $\overline{\mathrm{SIF}}$, where $\mathrm{DC}_{\mathrm{total}}$ is calculated from all-sky PAR for both $\overline{\mathrm{SIF}}$. The impact of diurnal changes in cloudiness is evaluated as the ratio of arithmetic $\overline{\mathrm{SIF}}$ with $\mathrm{DC}_{\mathrm{total}}$ calculated by all-sky PAR to clear-sky PAR. The shaded periods are wet seasons with high cf from October to May.

We compared the arithmetic $\overline{\mathrm{SIF}}$ calculated from $\mathrm{DC}_{\mathrm{total}}$ in the Amazon using all-sky PAR (as in Figure 4.3) against clear-sky PAR (as in Figure 4.2), which highlights the impact of the diurnal cycle in cloudiness. Although the amplitude of the diurnal cycle biases can be comparable to the clear sky bias, the DC can either be over or underestimated, unlike the consistent overestimation due to the clear sky bias (Figure 4.5c). A stricter cloud filter often has a larger impact on SIF_{dc}, suggesting that using a relaxed cloud filter can avoid some of the clear sky bias caused by the diurnal changes in PAR.

Doughty et al. (2021) reported the seasonal dynamic range of the arithmetic $\overline{SIF}$ is only about ± 20% of the annual average in Amazon rain forests. An overestimation of SIF by 25% in wet seasons due to the clear sky bias can cause large biases when interpreting this small season dynamic of $\overline{SIF}$. Therefore, the impact of cloudiness on both DC and upscaling SIF to long-term averages should be considered.

Topographic effects

Topographic corrections on PAR

The San Gabriel Mountains, California, USA (34°N– 34.6 °N, 118.4 °W – 117.4°W) are located north of the Los Angeles basin and are oriented east-west over 500 km, and their elevation ranges from 0 to more than 2500 m (Figure 4.6). The mountains have higher vegetation coverage, inferred from NDVI, kNDVI, and NIR_v, than the north or south of the mountains where deserts and cities are located. In general, the south facing slopes are more barren than north facing slopes (Figure 4.7a) because strong radiation increases skin temperature and potential evapotranspiration, which stresses plants in this dry climate.

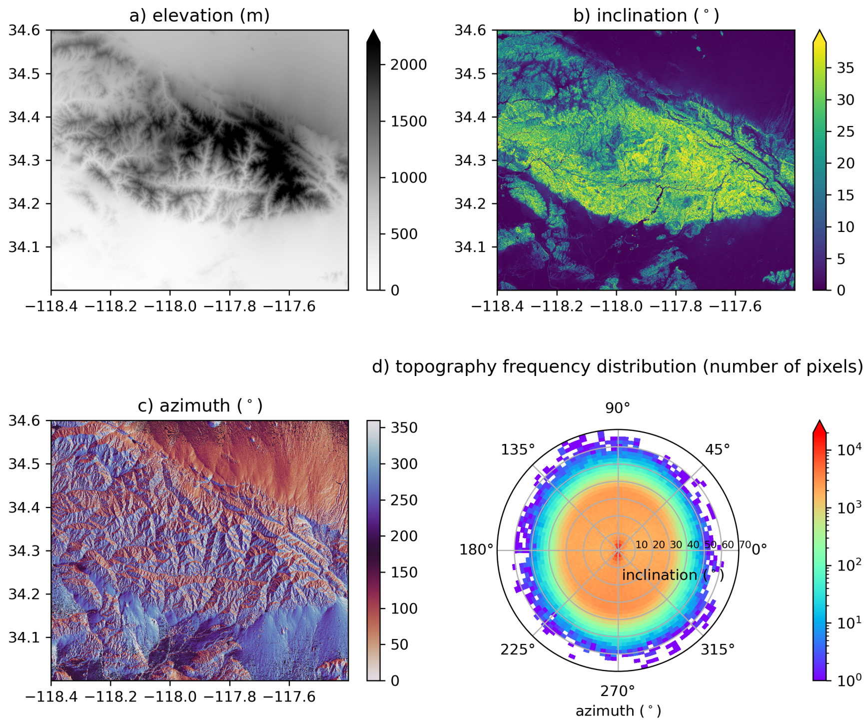

Figure 4.6: Surface elevation (a), inclination (b), and azimuth (c) in the San Gabriel Mountains (CA, USA). Panel d shows the frequency distribution of inclination and azimuth from 30-m pixels binned by 2° intervals. Azimuth is measured in degrees counter-clockwise from East.

Our topographic correction has no impact on NDVI and kNDVI, because the correction factor cancels out for both indices. However, the correction changes the NIR_v (Figure 4.7i and 4.8f), which scales with the derived R_{NIR} correction. As the San Gabriel Mountains are very rugged with surfaces facing towards all azimuth directions (Figure 4.6d), there are no large-scale features on the map changing dramatically in NIR_v before and after the topographic correction (Figure 4.7c and f). However, the NIR_v values of west(east)-facing slopes are higher(lower) after the correction (Figure 4.7i).

Figure 4.7d-e and g-h show that our topographic correction improves the correlation coefficients (r^2) between NIR_v and NDVI (kNDVI) by 11% (12%) in LandSat pixels where the absolute changes in NIR_v is larger than 0.02. For pixels with smaller changes in NIR_v (between 0.01 and 0.02), the improvements in r^2 are smaller (about 4%). Meanwhile, the root mean squared errors (rmse) are also improved.

The correlations of NIR_v with NDVI and kNDVI become nonlinear at high values, which may be attributed to the saturation of NDVI and kNDVI.

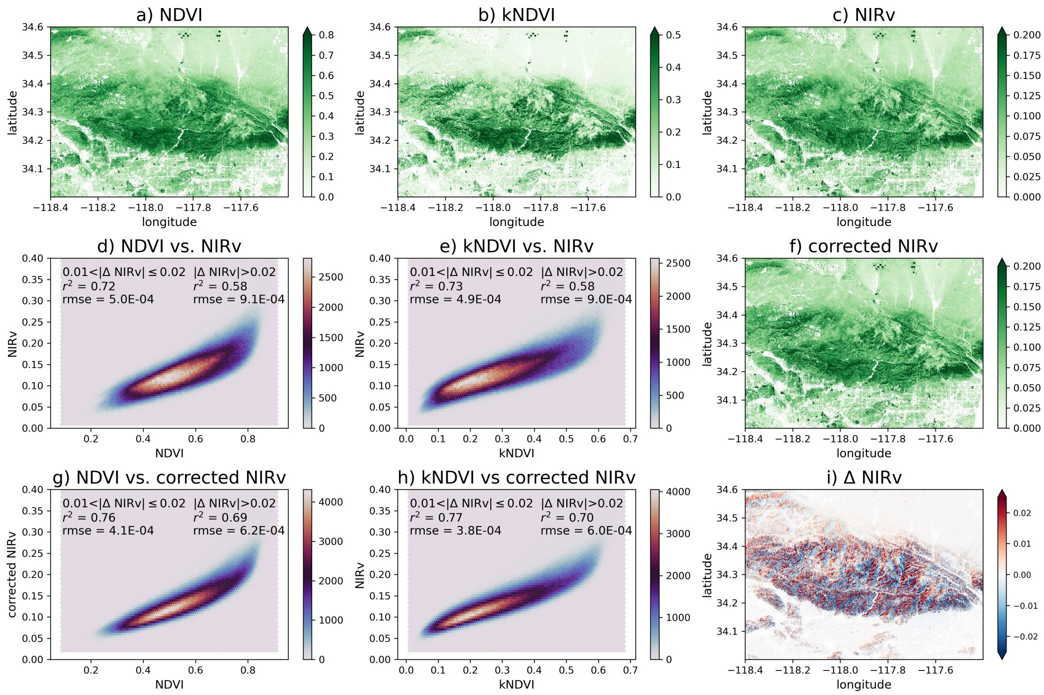

Figure 4.7: Impact of topographic correction on surface reflectance using the San Gabriel Mountains (CA, USA) as example, with a LandSat satellite overpass local time t_m of 10:31 am on July 3, 2020. SZA and $\alpha_{\odot}$ are 22.5° and 335.4°, respectively. Azimuth is measured in degrees counter-clockwise from East. Panels a and b show LandSat based NDVI and kNDVI. Panels c and f are LandSat based NIR_v before and after topographic correction. Panel i is the difference between panels c and f. Panels d and e are the frequency distribution of NIR_v before topographic correction plotted against NDVI and kNDVI. Panels g and h are the frequency distribution of NIR_v after topographic correction plotted against NDVI and kNDVI. In panels d, e, g, and h, the correlation coefficients (r^2) and root mean squared error (rmse) are grouped by absolute difference in NIR_v before and after the topographic correction.

In general, NDVI and kNDVI are higher on northwest facing slopes (Figure 4.8a-b), showing a clear preference for vegetation in a dry environment such as Los Angeles. Because the Sun is due East ($\alpha_{\odot}$ is 335.1°) at the time of the LandSat overpass, east facing slopes have a smaller SIA (Figure 4.8d) and receive more direct PAR. Therefore, raw NIR_v is higher on east facing slopes (Figure 4.8c). Our topographic correction decreases NIR_v on southeast facing (sun facing in the morning) slopes and increases NIR_v on the northwest facing (sun shaded in the morning) slopes (Figure 4.8e).

Using NIR$_v$ without topographic corrections could result in a wrong interpretation as to which surface slopes are more vegetated, as shown in the stark differences between panels a and c in Figure 4.8. While the NIR$_v$ has shown a better correspondence with gross primary production (Badgley et al., 2017), one has to keep this potential bias in mind, as the NIR$_v$ looses one key advantage of the NDVI, namely that many error sources cancel out in simple ratio approaches (Frankenberg et al., 2021).

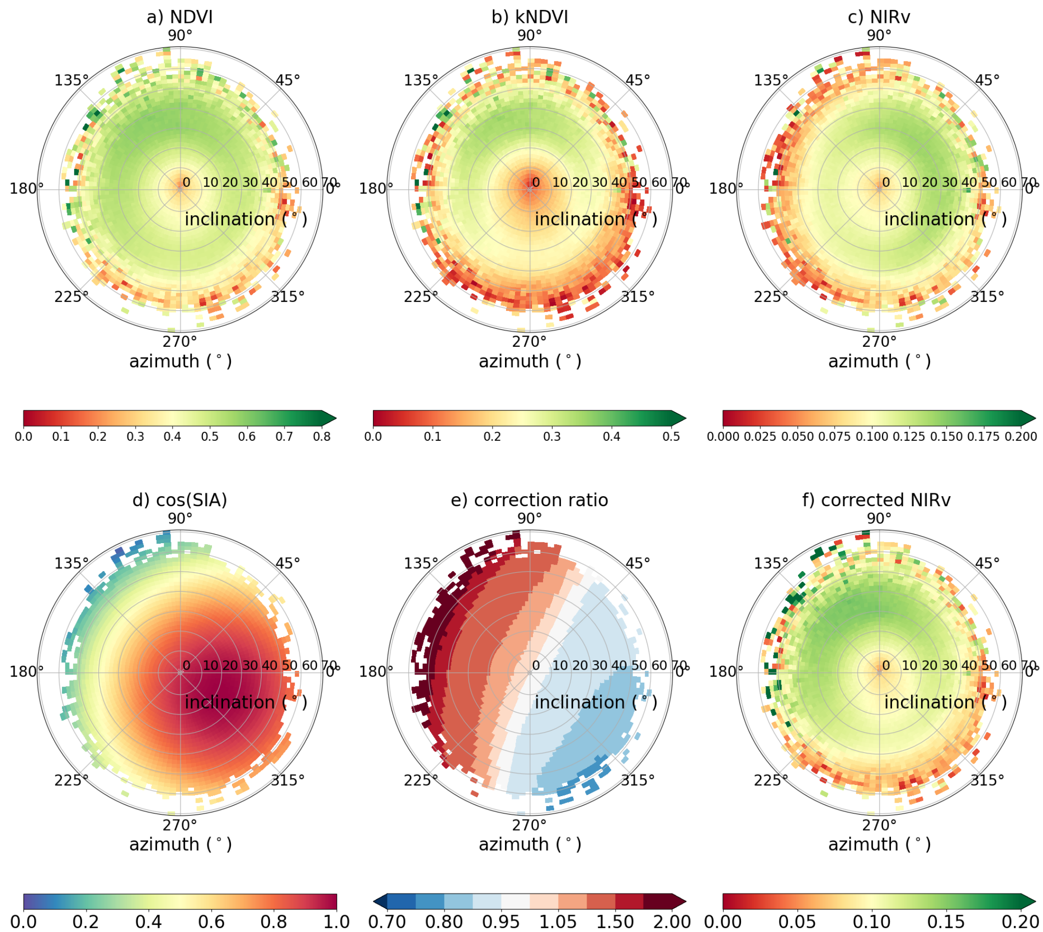

Figure 4.8: Impact of topographic correction on surface reflectance in polar maps using the San Gabriel Mountains (CA, USA) as example, with a LandSat satellite overpass local time t_m of 10:31 am on July 3, 2020. SZA and $\alpha_\odot$ are 22.5° and 335.4°, respectively. Azimuth is measured in degrees counter-clockwise from East. Panels a-c and f are the same as Figure 4.7a-c and f but in polar coordinates. Surface inclination is on the diameter axis, and surface azimuth is on the angular axis. The cosine of SIA is shown in panel d. Panel e is the ratio of panel f to panel c.

After the topographic correction, all three VIs are higher on northwest facing slopes (Figure 4.8a,b, and f), providing a consistent representation of vegetation distribution as a function of surface orientation. Our topographic correction is also comparable to a rigorous semi-empirical modified cosine correction (Soenen et al., 2005; Teillet et al., 1982)(Sect. sect:SCSC) proving that our general approach to correct $\mathrm{PAR_{direct}}$ (Equation 4.6) can properly account for the various illumination conditions due to topography. Therefore, we can apply the topographic adjustment to the $\mathrm{DC_{DEM}}$ calculation.

Topographic effects on DC

When calculating $\mathrm{DC_{DEM}}$, we consider the different t_m and spatial resolutions from TROPOMI and the upcoming Fluorescence EXplorer (FLEX) mission. TROPOMI overpasses the San Gabriel Mountains at 1:29 pm LST on July 3, 2020, when SZA and $\alpha_\odot$ are 22.6° and 204.6°, respectively. FLEX has a prospective t_m at 10:00 am LST (Drusch et al., 2017), when the SZA and $\alpha_\odot$ are 27.9° and 343.7°. The spatial resolution of TROPOMI is 5 km × 3.5 km at nadir (up to 14 km at the edges of the swath) (Köhler et al., 2018). The prospective spatial resolution of FLEX is 300 × 300 m^2. We first calculate $\mathrm{DC_{dem}}$ at the 30-m DEM resolution and then aggregate $\mathrm{DC_{DEM}}$ to the spatial resolutions of TROPOMI and FLEX using LandSat NDVI as weights.

$\mathrm{DEM_{total}}$ is homogeneous in the San Gabriel Mountains because Equation 4.4 omits the surface inclination and azimuth. However, $\mathrm{DC_{DEM}}$ calculated with Equation 4.11 is a function of inclination and azimuth angles as well as t_m. The theoretical ratio of $\mathrm{DC_{DEM}}$ to $\mathrm{DC_{total}}$ is demonstrated in Figure 4.9b and e. The overall magnitude of the theoretical $\mathrm{DC_{DEM}}$ can be as large as 500% of $\mathrm{DC_{total}}$ (Figure 4.9b and e) at the 30-m DEM resolution. These extremely large corrections can happen when the SIA approaches or exceeds 90°, at which only a very low amount of direct PAR reaches the respective surface.

The pattern and amplitude of $\mathrm{DC_{DEM}}$ also depend on t_m. When TROPOMI overpasses the San Gabriel Mountains, the northeast facing (sun-shaded) slopes have higher $\mathrm{DC_{DEM}}$ than the southwest facing (sun-facing in the afternoon) slopes (Figure 4.9b and c). Other sensors may overpass the same region at different t_m resulting in different patterns and magnitudes in $\mathrm{DC_{DEM}}$. For example, when FLEX overpasses 10:00 am LST, the northwest facing (sun-shaded in the morning) slopes have higher $\mathrm{DC_{DEM}}$ than the southeast facing (sun-facing) slopes (Figure 4.9e and f).

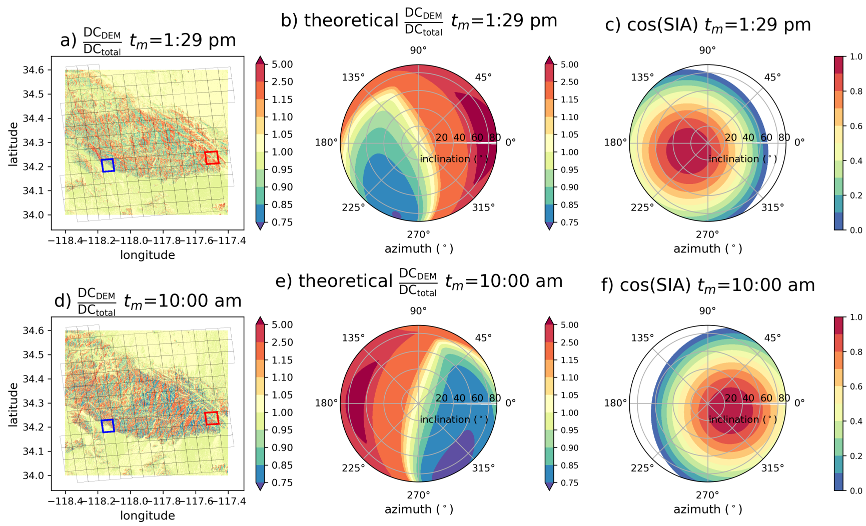

Figure 4.9: Topographic corrections on DC with various t_m in San Gabriel Mountains. Panels a-c are the ratio of DC_{DEM} to DC_{total}, the ratio of theoretical DC_{DEM} to DC_{total}, and cosine of SIA at t_m of TROPOMI at 1:29 pm LST on July 3, 2020, when SZA and $\alpha_{\odot}$ are 22.6° and 204.6°, respectively. Azimuth is measured in degrees counter-clockwise from East. Panel d-f are the same as a-c but at the prospective overpass of FLEX at 10:00 am LST, when SZA and $\alpha_{\odot}$ are 27.9° and 343.7°. Panels b, c, e, and f are in polar coordinates, if the surface inclination is from 0 – 90 °, and the surface azimuth is from 0-360 °. The surface inclination is on the diameter axis, and surface azimuth is on the angular axis. The grids in panels a and d are TROPOMI footprints, where the footprints with maximum and minimum NDVI-weighted $\frac{DC_{DEM}}{DC_{total}}$ are plotted in red and blue, respectively.

For SIF observed from satellites, the topographic impact on DC is aggregated among the sub-pixels within satellite footprints. In the San Gabriel Mountains, the topographic dependence of illumination and vegetation distribution covary at the sub-pixel scale. Regions with a larger ratio of DC_{DEM} to DEM_{total} also have higher NDVI at both overpass time (Figure 4.10h and 4.11h). According to Figure 4.8, these sub-pixels with high NDVI values mostly face north, as expected in a semi-arid climate. Therefore, to account for the varying vegetation coverage across sub-pixel slopes in the aggregated DC_{DEM} over TROPOMI and FLEX footprints, we average the sub-pixel variations of DC_{DEM} in each footprint by weighting them by NDVI (Deng et al., 2007; Turner et al., 2020).

Our results show that although the full dynamic range of DC_{DEM} at 30-m sub-pixel resolution is 75–500% of DC_{total} (Figure 4.9a-b and d-e), the TROPOMI footprint with the maximum NDVI-weighted mean DC_{DEM} in the scene (red outline) is only

9% larger than DC_{total} (Figure 4.10a). On the other extreme, the TROPOMI footprint with the minimum NDVI-weighted mean DC_{DEM} (blue outline) is only 1% larger than DC_{total} (Figure 4.11a). The bias dynamic range is thus on the order of about 10% for TROPOMI. The upcoming FLEX mission has a much finer footprint (300 $\times$ 300 m^2, Coppo et al. 2017). Thus, for increasingly smaller footprints, such as for FLEX (grids in Figure 4.10c-d and 4.11c-d), a topographic slope correction will become more important.

In summary, if one wants to study vegetation dynamics in mountains, corrections on both SIF and surface reflectance play a crucial role, as otherwise even the greenness variations as a function of surface slope and orientation can be severely misinterpreted. While individual effects of highly tilted surfaces can be substantial, they might be reduced at coarser spatial scales, where mean slopes are smaller. For very rugged terrain like the San Gabriel Mountains, the sub-pixel variations are mostly smoothed out within the comparatively coarse TROPOMI footprint (grids in Figure 4.9). Other mountain ranges might have more spatially extended slopes, which could even be important for coarser-scale sensors such as TROPOMI. Overall, biases in the length-of-day correction due to surface slopes are of similar magnitude as the overall atmospheric effects but will become increasingly crucial for high surface slopes and for smaller footprints sizes.

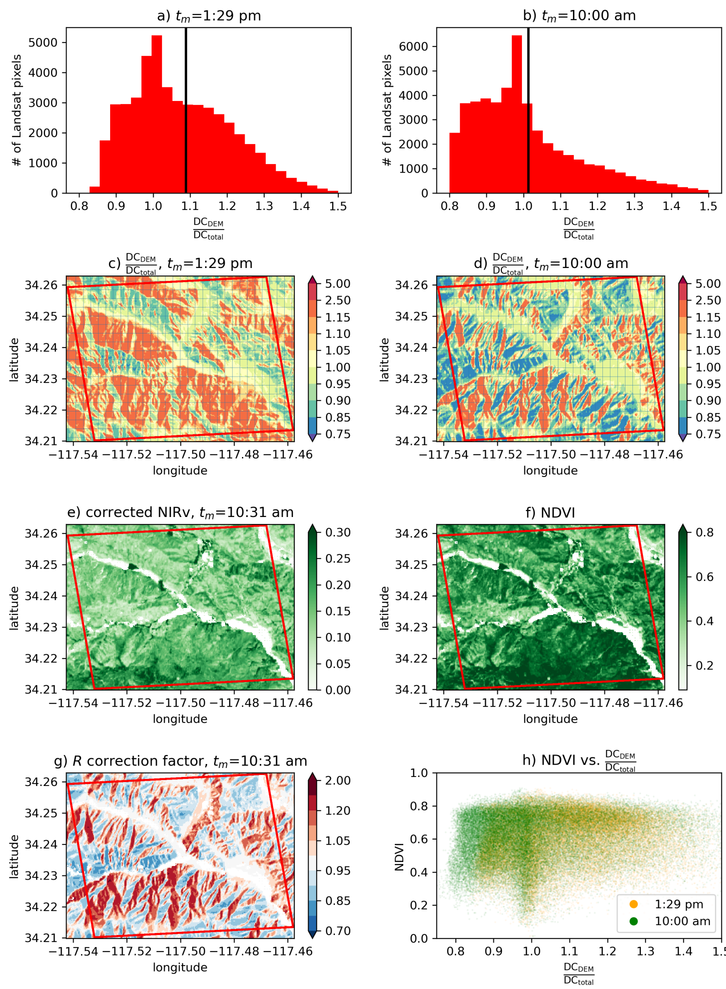

Figure 4.10: In the TROPOMI footprint with maximum NDVI-weighted mean $\frac{\mathrm{DC_{DEM}}}{\mathrm{DC_{total}}}$ (the red outlined footprint in Figure 4.9), $\frac{\mathrm{DC_{DEM}}}{\mathrm{DC_{total}}}$ of all sub-pixels is presented in a histogram (panel a) and a zoomed-in map (panel c) when t_m is at TROPOMI overpass (1:29 pm LST on July 3, 2020). Panels b and d are the same as panels a and c but at prospective FLEX overpass (10:00 am LST on July 3, 2020). The black lines in panels a and b indicate the ratio of NDVI-weighted mean $\mathrm{DC_{DEM}}$ to $\mathrm{DC_{total}}$ in this TROPOMI footprint. The red frame in all maps depicts actual TROPOMI footprint. The grids in c) and d) are the prospective FLEX footprints.

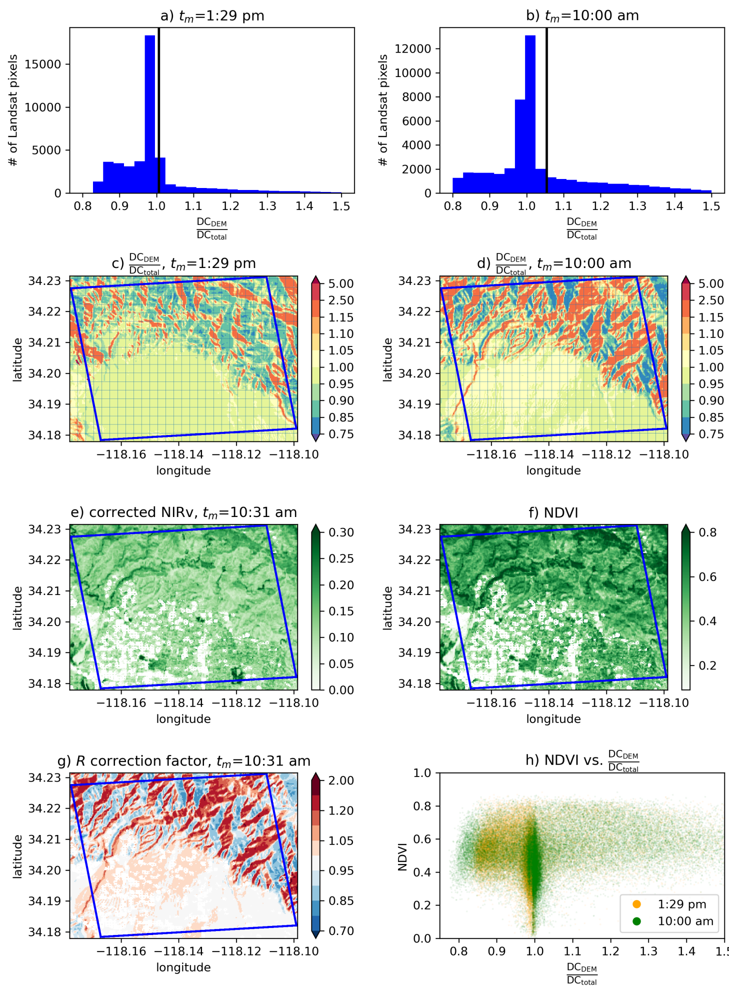

Figure 4.11: In the TROPOMI footprint with minimum NDVI-weighted mean $\frac{DC_{DEM}}{DC_{total}}$ (the blue outlined footprint in Figure 4.9), $\frac{DC_{DEM}}{DC_{total}}$ of all sub-pixels is presented in a histogram (panel a) and a zoomed-in map (panel c) when t_m is at TROPOMI overpass (1:29 pm LST on July 3, 2020). Panels b and d are the same as panels a and c but at prospective FLEX overpass (10:00 am LST on July 3, 2020). The black lines in panels a and b indicate the ratio of NDVI-weighted mean DC_{DEM} to DC_{total} in this TROPOMI footprint. The blue frame in all maps depicts actual TROPOMI footprint. The grids in c) and d) are the prospective FLEX footprints.

4.6 Discussion

Significance of atmosphere on DC

In this study, we use reanalysis PAR data to evaluate the impact of neglected atmospheric extinction in the conventional calculation of DC for SIF. We find that the overall bias in the simple geometric approach that is widely used in SIF studies is surprisingly small, both for cloudy and cloud free conditions. In most case, the bias is smaller than 10% at coarse spatial and temporal scales. The main reason for the small bias is a compensating effect of a reduction in direct light and enhancement of diffuse light when clouds and aerosols are present. To be more accurate, our proposed DC corrections can use actual PAR data from meteorological reanalysis data but in most cases, the simple DC_{SZA} should suffice and our results support the previously unvalidated simple approach to scale instantaneous SIF to daily averages.

Significance of clear sky bias in temporal averages

When SIF_{dc} is upscaled in time, e.g. to monthly averages, changes in daily PAR within the averaging window should be taken into account, especially in regions with low measurement yields due to frequent cloud cover. This way, the upscaled monthly SIF is not biased by SIF measurements from clear days only. We find that seasonal clear-sky biases can be on the order of 25% larger than most of the biases in the simple DC correction. While our approach uses just reanalysis data, one might also apply actual PAR measurements at field sites for the correction, if available. However, only reanalysis data can provide corrections for the clear sky bias at global scales.

Significance of topography on DC

Topography can be an important factor to consider for interpreting satellite measured SIF as well as NIRv in complex terrain because their magnitudes depend on the radiation projected on tilted surfaces. The significance of topographic corrections on SIF and NIRv depends on the relative scale of surface roughness and satellite footprints. For example, the impact of very rugged terrain in San Gabriel Mountains is mostly smoothed out within kilometer-wide TROPOMI footprints, while the topography can be significant in the footprints of upcoming FLEX mission which has 300-wide footprints.

The topographic impact on DC also compounds with the dependence of vegetation distribution on topography. Thus, the heterogeneous vegetation distribution should be considered when aggregating varying sub-pixel DC due to topography. In the meantime, topographically corrected SIF and VIs in fine spatial resolutions can benefit vegetation studies across environmental gradients related to topography, which are restricted by conventional observation tools, such as Eddy Covariance techniques.

Uncertainties in explicitly expressed DC models

The current calculation for DC_{total} and DC_{DEM} may inherit errors from the reanalysis data. For example, we assume PAR is a constant fraction of shortwave radiation at the surface since the current ERA5 version does not provide accurate PAR data. The absolute value of this constant is less important here since it is canceled out when calculating DCs. However, this assumption may not hold since the atmospheric scattering along the light path is wavelength dependent (Bates, 1984). Blue light is more sensitive to Rayleigh scattering than longer wavelengths. Under different cloud cover and light path lengths, the spectral shape of incident PAR at the surface can be different from the spectral shape at the top of atmosphere, which would require a scene dependent scaling factor between short-wave totals and PAR. To further improve the accuracy of DCs, accurately calculated PAR data should be used when it is published in future ERA5 versions. In the future, analyzing the uncertainty caused by reanalysis data and validating the result with in-situ PAR data might be needed.

In addition, future corrections might treat direct and diffuse light separately and take into account that GPP can saturate at high PAR levels while SIF is only mildly reduced. A simple non-linear scaling function for PAR in all our correction schemes could takes some of these effects into account but is omitted here as we wanted to focus on potential biases under the most benign assumptions.

4.7 Conclusion

Instantaneous SIF measurements require correction factors to scale these measurements to daily averages, which can then be aggregated within longer time scales. We focus on three factors impacting daily average SIF and its temporal averages spanning multiple days: atmospheric scattering, clear-sky biases, and topography. Overall, we find that the simple and frequently used DC_{SZA} approach is a convenient yet surprisingly accurate tool for calculating DC on a flat surface, which yields less than 10% biases compared to using exact PAR. In extreme cases, such as a high SZA at t_m and cloudy days, using DC_{SZA} is less accurate for SIF_{dc} and its seasonality since the biases can reach up to 20%.

When aggregating measurements in time, we find that clear-sky biases can arise. For regions experiencing significant seasonal changes in cloudiness, PAR-weighted monthly mean SIF benefits the interpretation of SIF_{dc} seasonality. This can even compound the interpretation of seasonal SIF dynamics that have a low seasonal dynamic range in SIF but large variations in cloudiness. This holds for the Amazon basin in regions with distinct dry and wet seasons, for which SIF in periods with frequent cloudiness can be overestimated by about 25%, which is significant given the overall seasonal dynamic range in SIF is only ±20%.

For complex terrains, we find that an additional correction for surface slopes and orientation is required. Our topographically corrected expression for DC is not negligible, specifically for satellites with small footprints, which can observe highly tilted surfaces within their footprints. In our examples, the biases in DC due to topography can be up to 500% and also impact reflectance measurements, especially the novel NIR_v index.

As more space-borne SIF measurements become available, our length-of-day correction and monthly averaging methods are useful for homogenizing and comparing SIF measurements across a variety of overpass and spatiotemporal scales. In complex terrain, including the topography to the calculation of DC is especially critical for satellites with finer footprints but can also be relevant for coarser spatial scales, e.g. if regions of the size of the satellite footprint are sloped.

4.8 Appendix

Appendix A. Cosine Correction on VIs

We correct the surface reflectance with a semi-empirical method. For vegetated pixels (NDVI>0.3), we use the Sun-Canopy-Sensor (SCS+C) topographic correction (Soenen et al., 2005). For less-vegetated pixels (NDVI≤0.3), we use the slope-aspect correction (Teillet et al., 1982). The C factor in both corrections were calculated from regressing the surface reflectance and cos(SZA) in less-vegetated pixels. Thus, the C factor is wavelength-dependent. This explains the small changes in NDVI and kNDVI after the correction in Figure 4.12. Overall, the corrected NIR_v using our method (Figure 4.8e-f) is very similar to using the semi-empirical correction method for R (Figure 4.12j-k).

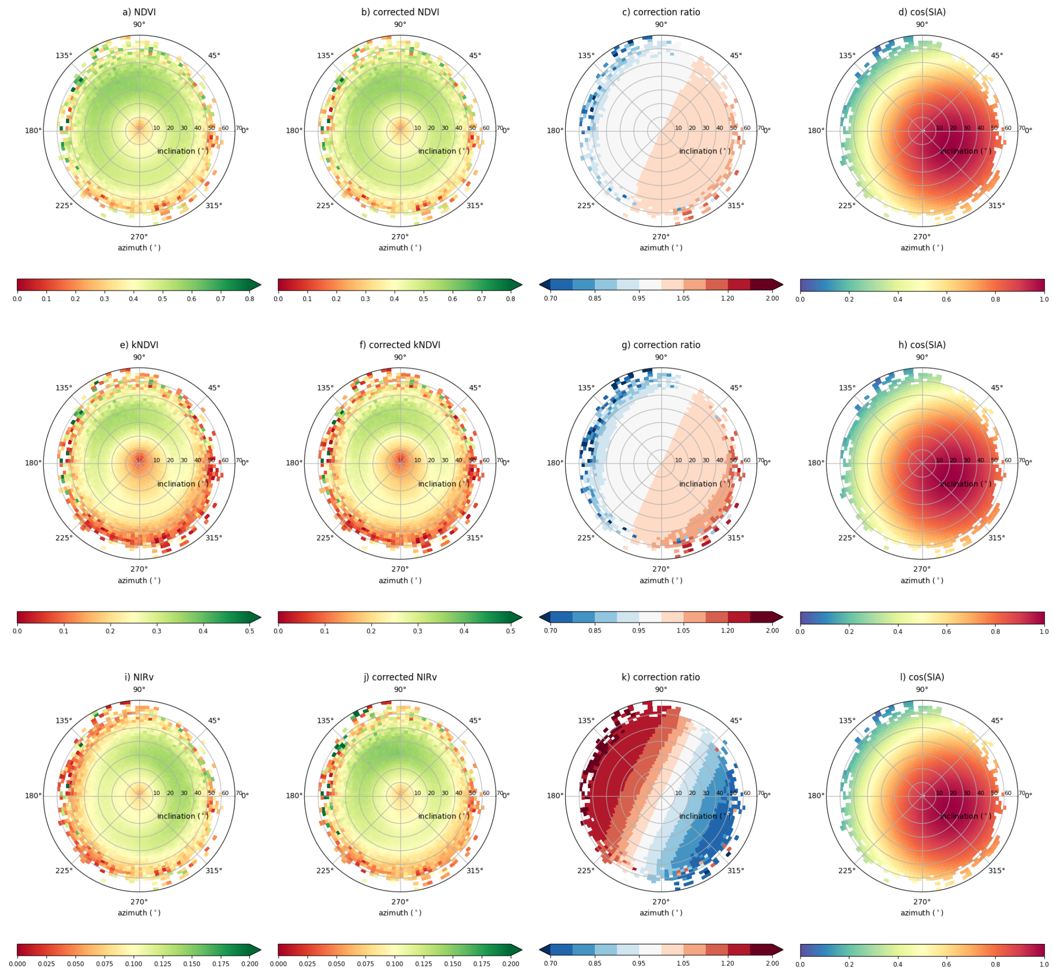

Figure 4.12: a) original NDVI; b) topography corrected NDVI; c) topography corrected NDVI/original NDVI; d) cos(SZA) at LandSat overpass time (10:31 am on July 3, 2020); e) original kNDVI; f) topography corrected kNDVI; g) topography corrected kNDVI/oiginal kNDVI; h) same as d); i) original NIR_v; j) topography corrected NIR_v; and k) topography corrected NIR_v/original NIR_v; and l) same as d). In these polar maps, surface slope is on the diameter axis, and surface aspect is on the angle axis.

Appendix B. Details of calculating PAR_{direct} and $PAR_{diffuse}$ using ERA5 reanalysis data

variables used in this study		ERA5 variable names
clear-sky	PAR_{direct}	0.46×Clear-sky direct solar radiation at surface
	$PAR_{diffuse}$	0.46×(Surface solar radiation downward, clear sky - Clear-sky direct solar radiation at surface)
all-sky	PAR_{direct}	0.46×Total sky direct solar radiation at surface
	$PAR_{diffuse}$	0.46× (Surface solar radiation downwards - Total sky direct solar radiation at surface)

Appendix C. Maximum Number of Soundings

We use the same gridded SIF product as Sect 4.5, which is aggregated from individual SIF measurements in 2020 and has a temporal resolution of 16 days and a spatial resolution of 0.0833° × 0.0833°. The number of averaged soundings per grid cell is n in cloud-filtered and N in unfiltered cases, the latter of which represents the total number of potential TROPOMI soundings.

The maximum numbers of soundings are higher at high latitudes (Figure 4.14) because of overlapping ground tracks. However, due to larger SZA (Figure 4.13), the measurement yield is smaller at high latitudes (Figure 4.4).

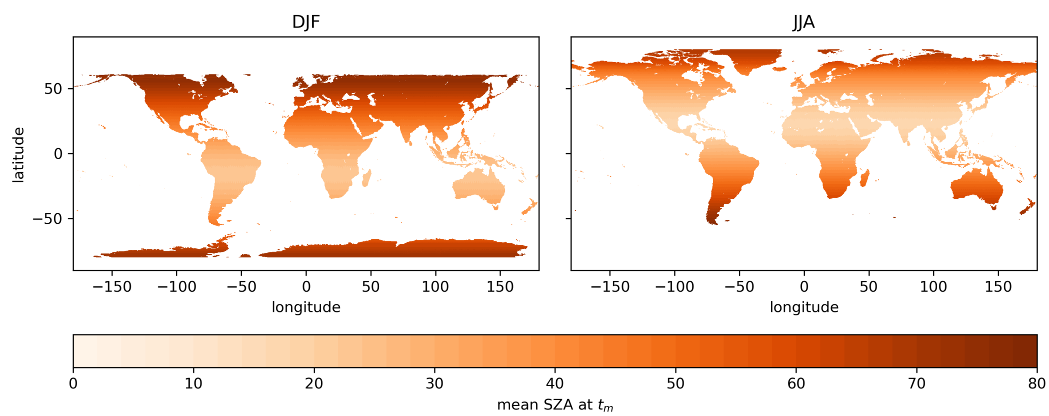

Figure 4.13: The mean SZA at t_m per 16 days averaged over December, January, and February (left panel) and June, July, and August (right panel)

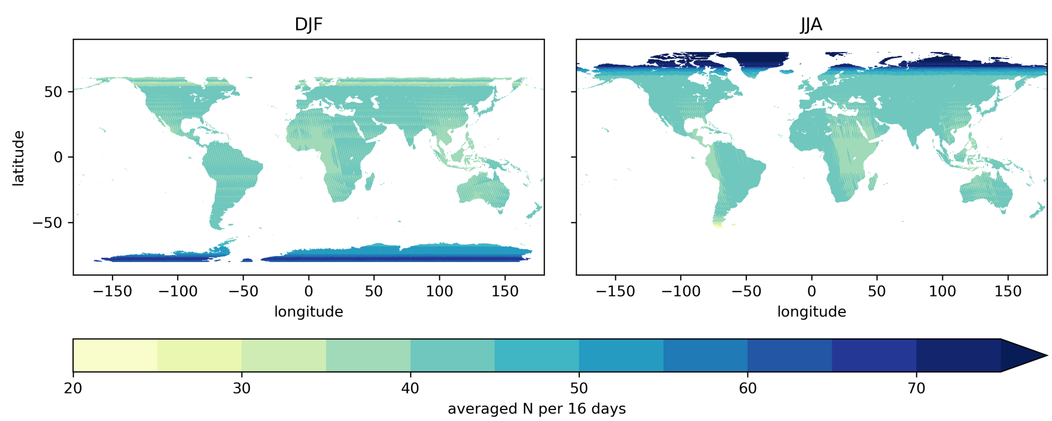

Figure 4.14: The total numbers of unfiltered soundings (N) per 16 days averaged over December, January, and February (left panel) and June, July, and August (right panel)

Appendix D. List of variables

acronym	term
t	time
t_m	time of measurement
SZA	solar zenith angle
$\alpha_\odot$	solar azimuth angle
μ	cosine of SZA
β	surface inclination angle
α	surface azimuth angle
SIA	solar incidence angle
SIF_{t_m}	instantaneous SIF at t_m
$\mathrm{SIF}_{\mathrm{dc}}$	daily-average SIF
PAR	photosynthetic active radiation
$\mathrm{PAR}_{\mathrm{direct}}$	direct PAR
$\mathrm{PAR}_{\mathrm{diffuse}}$	diffuse PAR
DC	length-of-day correction factor
$\mathrm{DC}_{\mathrm{SZA}}$	conventional DC using cosine SZA
$\mathrm{DC}_{\mathrm{direct}}$	DC using $\mathrm{PAR}_{\mathrm{direct}}$ only
$\mathrm{DC}_{\mathrm{total}}$	DC using both $\mathrm{PAR}_{\mathrm{direct}}$ and $\mathrm{PAR}_{\mathrm{diffuse}}$
$\mathrm{PAR}_{\mathrm{direct,\ DEM}}$	direct PAR corrected by surface topography
$\mathrm{DC}_{\mathrm{DEM}}$	DC considering surface topography
R	reflectance
$\mathrm{R}_{\mathrm{DEM}}$	topographically corrected R
n	number of cloud filtered samples
N	number of total amount of samples (before cloud filtering)
$\overline{\mathrm{PAR}}_{\mathrm{day}}$	daily mean PAR
$\overline{\mathrm{PAR}}_{\mathrm{month}}$	monthly mean PAR
$\overline{\mathrm{SIF}}$	monthly mean SIF

4.9 Acknowledgement

This research is supported by the NASA CMS (award 80NSSC20K0010) and OCO Science team projects (award 80NSSC18K0895). We use a Julia gridding package from `https://github.com/cfranken/gridding`.

Bibliography

C. Albergel, E. Dutra, S. Munier, J.-C. Calvet, J. Munoz-Sabater, P. de Rosnay, and G. Balsamo. ERA-5 and ERA-Interim driven ISBA land surface model simulations: which one performs better? *Hydrology and Earth System Sciences*, 22(6):3515–3532, June 2018. ISSN 1607-7938. doi: 10.5194/hess-22-3515-2018. URL https://hess.copernicus.org/articles/22/3515/2018/.

B. Babar, R. Graversen, and T. Boström. Solar radiation estimation at high latitudes: Assessment of the CMSAF databases, ASR and ERA5. *Solar Energy*, 182:397–411, April 2019. ISSN 0038092X. doi: 10.1016/j.solener.2019.02.058. URL https://linkinghub.elsevier.com/retrieve/pii/S0038092X19301847.

G. Badgley, C. B. Field, and J. A. Berry. Canopy near-infrared reflectance and terrestrial photosynthesis. *Science Advances*, 3(3):e1602244, 2017. Publisher: American Association for the Advancement of Science.

R. Barnes. r-barnes/richdem, 2016. URL https://github.com/r-barnes/richdem. original-date: 2013-01-06T15:33:34Z.

D. R. Bates. Rayleigh scattering by air. *Planetary and Space Science*, 32(6):785–790, June 1984. ISSN 00320633. doi: 10.1016/0032-0633(84)90102-8. URL https://linkinghub.elsevier.com/retrieve/pii/0032063384901028.

T. E. Bilir, I. Fung, and T. E. Dawson. Slope-Aspect Induced Climate Differences Influence How Water Is Exchanged Between the Land and Atmosphere. *Journal of Geophysical Research: Biogeosciences*, 126(5), May 2021. ISSN 2169-8953, 2169-8961. doi: 10.1029/2020JG006027. URL https://onlinelibrary.wiley.com/doi/10.1029/2020JG006027.

G. Camps-Valls, M. Campos-Taberner, A. Moreno-Martinez, S. Walther, G. Duveiller, A. Cescatti, M. D. Mahecha, J. Muñoz-Marí, F. J. García-Haro, L. Guanter, M. Jung, J. A. Gamon, M. Reichstein, and S. W. Running. A unified vegetation index for quantifying the terrestrial biosphere. *Science Advances*, 7(9):eabc7447, February 2021. ISSN 2375-2548. doi: 10.1126/sciadv.abc7447. URL https://advances.sciencemag.org/lookup/doi/10.1126/sciadv.abc7447.

P. Coppo, A. Taiti, L. Pettinato, M. Francois, M. Taccola, and M. Drusch. Fluorescence Imaging Spectrometer (FLORIS) for ESA FLEX Mission. *Remote Sensing*, 9(7):649, June 2017. ISSN 2072-4292. doi: 10.3390/rs9070649. URL http://www.mdpi.com/2072-4292/9/7/649.

Y. Deng, X. Chen, E. Chuvieco, T. Warner, and J. P. Wilson. Multi-scale linkages between topographic attributes and vegetation indices in a mountainous landscape. *Remote Sensing of Environment*, 111(1):122–134, November 2007. ISSN 00344257. doi: 10.1016/j.rse.2007.03.016. URL https://linkinghub.elsevier.com/retrieve/pii/S0034425707001393.

R. Doughty, X. Xiao, Y. Qin, X. Wu, Y. Zhang, and B. Moore. Small anomalies in dry-season greenness and chlorophyll fluorescence for Amazon moist tropical forests during El Niño and La Niña. *Remote Sensing of Environment*, 253:112196, February 2021. ISSN 00344257. doi: 10.1016/j.rse.2020.112196. URL https://linkinghub.elsevier.com/retrieve/pii/S0034425720305691.

M. Drusch, J. Moreno, U. Del Bello, R. Franco, Y. Goulas, A. Huth, S. Kraft, E. M. Middleton, F. Miglietta, G. Mohammed, L. Nedbal, U. Rascher, D. Schüttemeyer, and W. Verhoef. The FLuorescence EXplorer Mission Concept—ESA's Earth Explorer 8. *IEEE Transactions on Geoscience and Remote Sensing*, 55(3):1273–1284, March 2017. ISSN 1558-0644. doi: 10.1109/TGRS.2016.2621820.

J. A. Duffie and W. A. Beckman. *Solar engineering of thermal processes / John A. Duffie, William A. Beckman*. John Wiley, Hoboken, 4th ed edition, 2013. ISBN 978-0-470-87366-3.

C. Frankenberg, J. B. Fisher, J. Worden, G. Badgley, S. S. Saatchi, J.-E. Lee, G. C. Toon, A. Butz, M. Jung, A. Kuze, and T. Yokota. New global observations of the terrestrial carbon cycle from GOSAT: Patterns of plant fluorescence with gross primary productivity: CHLOROPHYLL FLUORESCENCE FROM SPACE. *Geophysical Research Letters*, 38(17):n/a–n/a, September 2011. ISSN 00948276. doi: 10.1029/2011GL048738. URL http://doi.wiley.com/10.1029/2011GL048738.

C. Frankenberg, Y. Yin, B. Byrne, L. He, and P. Gentine. Comment on "Recent global decline of CO $_2$ fertilization effects on vegetation photosynthesis". *Science*, 373(6562):eabg2947, September 2021. ISSN 0036-8075, 1095-9203. doi: 10.1126/science.abg2947. URL https://www.science.org/doi/10.1126/science.abg2947.

P. Gentine and S. H. Alemohammad. Reconstructed Solar-Induced Fluorescence: A Machine Learning Vegetation Product Based on MODIS Surface Reflectance to Reproduce GOME-2 Solar-Induced Fluorescence. *Geophysical Research Letters*, 45(7):3136–3146, April 2018. ISSN 0094-8276, 1944-8007. doi: 10.1002/2017GL076294. URL https://onlinelibrary.wiley.com/doi/abs/10.1002/2017GL076294.

L. Gu, J. D. Fuentes, H. H Shugart, R. M. Staebler, and T. A. Black. Responses of net ecosystem exchanges of carbon dioxide to changes in cloudiness: Results from two North American deciduous forests. *Journal of Geophysical Research: Atmospheres*, 104(D24):31421–31434, December 1999. ISSN 01480227. doi: 10.1029/1999JD901068. URL http://doi.wiley.com/10.1029/1999JD901068.

L. Gu, J. Han, J. D. Wood, C. Y-Y. Chang, and Y. Sun. Sun-induced Chl fluorescence and its importance for biophysical modeling of photosynthesis based on light reactions. *New Phytologist*, 223(3):1179–1191, August 2019. ISSN 0028-646X, 1469-8137. doi: 10.1111/nph.15796. URL https://onlinelibrary.wiley.com/doi/10.1111/nph.15796.

L. He, T. Magney, D. Dutta, Y. Yin, P. Köhler, K. Grossmann, J. Stutz, C. Dold, J. Hatfield, K. Guan, B. Peng, and C. Frankenberg. From the Ground to Space: Using Solar-Induced Chlorophyll Fluorescence to Estimate Crop Productivity. *Geophysical Research Letters*, 47(7), April 2020. ISSN 0094-8276, 1944-8007. doi: 10.1029/2020GL087474. URL https://onlinelibrary.wiley.com/doi/10.1029/2020GL087474.

B. K. P. Horn. Hill shading and the reflectance map. *Proceedings of the IEEE*, 69(1):14–47, 1981. ISSN 0018-9219. doi: 10.1109/PROC.1981.11918. URL http://ieeexplore.ieee.org/document/1456186/.

T. A. Howell, D. W. Meek, and J. L. Hatfield. Relationship of photosynthetically active radiation to shortwave radiation in the San Joaquin Valley. *Agricultural Meteorology*, 28(2):157–175, February 1983. ISSN 00021571. doi: 10.1016/0002-1571(83)90005-5. URL https://linkinghub.elsevier.com/retrieve/pii/0002157183900055.

J. Hu, L. Liu, J. Guo, S. Du, and X. Liu. Upscaling Solar-Induced Chlorophyll Fluorescence from an Instantaneous to Daily Scale Gives an Improved Estimation of the Gross Primary Productivity. *Remote Sensing*, 10(10):1663, October 2018. ISSN 2072-4292. doi: 10.3390/rs10101663. URL http://www.mdpi.com/2072-4292/10/10/1663.

J. Hu, L. Liu, H. Yu, L. Guan, and Xinjie Liu. Upscaling GOME-2 SIF from clear-sky instantaneous observations to all-sky sums leading to an improved SIF–GPP correlation. *Agricultural and Forest Meteorology*, 306:108439, August 2021. ISSN 01681923. doi: 10.1016/j.agrformet.2021.108439. URL https://linkinghub.elsevier.com/retrieve/pii/S0168192321001222.

J. Joiner, Y. Yoshida, P. Köehler, P. Campbell, C. Frankenberg, C. van der Tol, P. Yang, N. Parazoo, L. Guanter, and Y. Sun. Systematic Orbital Geometry-Dependent Variations in Satellite Solar-Induced Fluorescence (SIF) Retrievals. *Remote Sensing*, 12(15):2346, July 2020. ISSN 2072-4292. doi: 10.3390/rs12152346. URL https://www.mdpi.com/2072-4292/12/15/2346.

S. A. Klein. Calculation of monthly average insolation on tilted surfaces. *Solar Energy*, 19(4):325–329, 1977. ISSN 0038092X. doi: 10.1016/0038-092X(77)90001-9. URL https://linkinghub.elsevier.com/retrieve/pii/0038092X77900019.

P. Kutiel. Slope Aspect Effect on Soil and Vegetation in a Mediterranean Ecosystem. *Israel Journal of Botany*, 41(4-6):243–250, January 1992. ISSN 0021-213X. doi: 10.1080/0021213X.1992.10677231. URL https://www.tandfonline.com/doi/abs/10.1080/0021213X.1992.10677231.

P. Köhler, C. Frankenberg, T. S. Magney, L. Guanter, J. Joiner, and J. Landgraf. Global Retrievals of Solar-Induced Chlorophyll Fluorescence With TROPOMI: First Results and Intersensor Comparison to OCO-2. *Geophysical Research*

Letters, 45(19):10,456–10,463, October 2018. ISSN 0094-8276, 1944-8007. doi: 10.1029/2018GL079031. URL `https://onlinelibrary.wiley.com/doi/abs/10.1029/2018GL079031`.

C. Lin, P. Gentine, C. Frankenberg, S. Zhou, D. Kennedy, and X. Li. Evaluation and mechanism exploration of the diurnal hysteresis of ecosystem fluxes. *Agricultural and Forest Meteorology*, 278:107642, November 2019. ISSN 01681923. doi: 10.1016/j.agrformet.2019.107642. URL `https://linkinghub.elsevier.com/retrieve/pii/S0168192319302503`.

X. Lu, Z. Liu, F. Zhao, and J. Tang. Comparison of total emitted solar-induced chlorophyll fluorescence (SIF) and top-of-canopy (TOC) SIF in estimating photosynthesis. *Remote Sensing of Environment*, 251:112083, December 2020. ISSN 00344257. doi: 10.1016/j.rse.2020.112083. URL `https://linkinghub.elsevier.com/retrieve/pii/S0034425720304569`.

T. S. Magney, M. L. Barnes, and X. Yang. On the covariation of chlorophyll fluorescence and photosynthesis across scales. *Geophysical Research Letters*, 47 (23):e2020GL091098, 2020. Publisher: Wiley Online Library.

G. H. Mohammed, R. Colombo, E. M. Middleton, U. Rascher, C. van der Tol, L. Nedbal, Y. Goulas, O. Pérez-Priego, A. Damm, M. Meroni, J. Joiner, S. Cogliati, W. Verhoef, Z. Malenovský, J.-P. Gastellu-Etchegorry, J. R. Miller, L. Guanter, J. Moreno, I. Moya, J. A. Berry, C. Frankenberg, and P. J. Zarco-Tejada. Remote sensing of solar-induced chlorophyll fluorescence (SIF) in vegetation: 50 years of progress. *Remote Sensing of Environment*, 231:111177, September 2019. ISSN 00344257. doi: 10.1016/j.rse.2019.04.030. URL `https://linkinghub.elsevier.com/retrieve/pii/S0034425719301816`.

D. C. Morton, J. Nagol, C. C. Carabajal, J. Rosette, M. Palace, B. D. Cook, E. F. Vermote, D. J. Harding, and P. R. J. North. Amazon forests maintain consistent canopy structure and greenness during the dry season. *Nature*, 506(7487):221–224, February 2014. ISSN 0028-0836, 1476-4687. doi: 10.1038/nature13006. URL `http://www.nature.com/articles/nature13006`.

J. Muñoz-Sabater, E. Dutra, A. Agustí-Panareda, C. Albergel, G. Arduini, G. Balsamo, S. Boussetta, M. Choulga, S. Harrigan, H. Hersbach, B. Martens, D. G. Miralles, M. Piles, N. J. Rodríguez-Fernández, E. Zsoter, C. Buontempo, and J.-N. Thépaut. ERA5-Land: a state-of-the-art global reanalysis dataset for land applications. *Earth System Science Data*, 13(9):4349–4383, September 2021. ISSN 1866-3516. doi: 10.5194/essd-13-4349-2021. URL `https://essd.copernicus.org/articles/13/4349/2021/`.

NASA JPL. NASA Shuttle Radar Topography Mission Global 1 arc second, 2013. URL `https://lpdaac.usgs.gov/products/srtmgl1v003/`. type: dataset.

A. Porcar-Castell, E. Tyystjärvi, J. Atherton, C. van der Tol, J. Flexas, E. E. Pfündel, J. Moreno, C. Frankenberg, and J. A. Berry. Linking chlorophyll a fluorescence to photosynthesis for remote sensing applications: mechanisms and challenges. *Journal of Experimental Botany*, 65(15):4065–4095, August 2014. ISSN 0022-0957. doi: 10.1093/jxb/eru191. URL `https://doi.org/10.1093/jxb/eru191`.

A. D. Richardson, T. F. Keenan, M. Migliavacca, Y. Ryu, O. Sonnentag, and M. Toomey. Climate change, phenology, and phenological control of vegetation feedbacks to the climate system. *Agricultural and Forest Meteorology*, 169: 156–173, 2013. Publisher: Elsevier.

S. R. Saleska, K. Didan, A. R. Huete, and H. R. da Rocha. Amazon Forests Green-Up During 2005 Drought. *Science*, 318(5850):612–612, October 2007. ISSN 0036-8075, 1095-9203. doi: 10.1126/science.1146663. URL `https://www.science.org/doi/10.1126/science.1146663`.

S. R. Saleska, J. Wu, K. Guan, A. C. Araujo, A. Huete, A. D. Nobre, and N. Restrepo-Coupe. Dry-season greening of Amazon forests. *Nature*, 531(7594):E4–E5, March 2016. ISSN 1476-4687. doi: 10.1038/nature16457. URL `https://www.nature.com/articles/nature16457`.

A. Samanta, S. Ganguly, H. Hashimoto, S. Devadiga, E. Vermote, Y. Knyazikhin, R. R. Nemani, and R. B. Myneni. Amazon forests did not green-up during the 2005 drought: AMAZON DROUGHT SENSITIVITY. *Geophysical Research Letters*, 37(5):n/a–n/a, March 2010. ISSN 00948276. doi: 10.1029/2009GL042154. URL `http://doi.wiley.com/10.1029/2009GL042154`.

N. G. Silleos, T. K. Alexandridis, I. Z. Gitas, and K. Perakis. Vegetation Indices: Advances Made in Biomass Estimation and Vegetation Monitoring in the Last 30 Years. *Geocarto International*, 21(4):21–28, December 2006. ISSN 1010-6049, 1752-0762. doi: 10.1080/10106040608542399. URL `http://www.tandfonline.com/doi/abs/10.1080/10106040608542399`.

S. A. Soenen, D. R. Peddle, and C. A. Coburn. SCS+C: a modified Sun-canopy-sensor topographic correction in forested terrain. *IEEE Transactions on Geoscience and Remote Sensing*, 43(9):2148–2159, September 2005. ISSN 0196-2892. doi: 10.1109/TGRS.2005.852480. URL `http://ieeexplore.ieee.org/document/1499030/`.

Y. Sun, C. Frankenberg, M. Jung, J. Joiner, L. Guanter, P. Köhler, and T. Magney. Overview of Solar-Induced chlorophyll Fluorescence (SIF) from the Orbiting Carbon Observatory-2: Retrieval, cross-mission comparison, and global monitoring for GPP. *Remote Sensing of Environment*, 209:808–823, May 2018. ISSN 00344257. doi: 10.1016/j.rse.2018.02.016. URL `https://linkinghub.elsevier.com/retrieve/pii/S0034425718300221`.

P. M. Teillet, B. Guindon, and D. G. Goodenough. On the Slope-Aspect Correction of Multispectral Scanner Data. *Canadian Journal of Remote Sensing*, 8(2):84–106, December 1982. ISSN 0703-8992, 1712-7971. doi: 10.1080/07038992.1982.10855028. URL http://www.tandfonline.com/doi/abs/10.1080/07038992.1982.10855028.

A. J. Turner, P. Köhler, T. S. Magney, C. Frankenberg, I. Fung, and R. C. Cohen. A double peak in the seasonality of California's photosynthesis as observed from space. *Biogeosciences*, 17(2):405–422, 2020. Publisher: Copernicus GmbH.

R. Urraca, T. Huld, A. Gracia-Amillo, F. J. Martinez-de Pison, F. Kaspar, and A. Sanz-Garcia. Evaluation of global horizontal irradiance estimates from ERA5 and COSMO-REA6 reanalyses using ground and satellite-based data. *Solar Energy*, 164:339–354, April 2018. ISSN 0038092X. doi: 10.1016/j.solener.2018.02.059. URL https://linkinghub.elsevier.com/retrieve/pii/S0038092X18301920.

C. van der Tol, A. J. Dolman, M. J. Waterloo, and K. Raspor. Topography induced spatial variations in diurnal cycles of assimilation and latent heat of Mediterranean forest. *Biogeosciences*, 4(1):137–154, February 2007. ISSN 1726-4170. doi: 10.5194/bg-4-137-2007. URL https://bg.copernicus.org/articles/4/137/2007/.

X. Xiao, B. Braswell, Q. Zhang, S. Boles, S. Frolking, and B. Moore. Sensitivity of vegetation indices to atmospheric aerosols: continental-scale observations in Northern Asia. *Remote Sensing of Environment*, 84(3):385–392, March 2003. ISSN 00344257. doi: 10.1016/S0034-4257(02)00129-3. URL https://linkinghub.elsevier.com/retrieve/pii/S0034425702001293.

D. Yang and J. M. Bright. Worldwide validation of 8 satellite-derived and reanalysis solar radiation products: A preliminary evaluation and overall metrics for hourly data over 27 years. *Solar Energy*, 210:3–19, November 2020. ISSN 0038092X. doi: 10.1016/j.solener.2020.04.016. URL https://linkinghub.elsevier.com/retrieve/pii/S0038092X20303893.

Y. Zhang, X. Xiao, Y. Zhang, S. Wolf, S. Zhou, J. Joiner, L. Guanter, M. Verma, Y. Sun, X. Yang, E. Paul-Limoges, C. M. Gough, G. Wohlfahrt, B. Gioli, C. van der Tol, N. Yann, M. Lund, and A. de Grandcourt. On the relationship between sub-daily instantaneous and daily total gross primary production: Implications for interpreting satellite-based SIF retrievals. *Remote Sensing of Environment*, 205:276–289, February 2018. ISSN 00344257. doi: 10.1016/j.rse.2017.12.009. URL https://linkinghub.elsevier.com/retrieve/pii/S0034425717305801.

Z. Zhang, Y. Zhang, Y. Zhang, and J. M. Chen. Correcting Clear-Sky Bias in Gross Primary Production Modeling From Satellite Solar-Induced Chlorophyll Fluorescence Data. *Journal of Geophysical Research: Biogeosciences*, 125(9), 2020. doi: 10.1029/2020JG005822.

L. M. Zuromski, D. R. Bowling, P. Köhler, C. Frankenberg, M. L. Goulden, P. D. Blanken, and J. C. Lin. Solar-Induced Fluorescence Detects Interannual Variation in Gross Primary Production of Coniferous Forests in the Western United States. *Geophysical Research Letters*, 45(14):7184–7193, July 2018. ISSN 0094-8276, 1944-8007. doi: 10.1029/2018GL077906. URL `https://onlinelibrary.wiley.com/doi/abs/10.1029/2018GL077906`.

Chapter 5

CONCLUSIONS

This thesis presents novel methods to improve the estimation of terrestrial ecosystem photosynthesis (Gross Primary Production, GPP) at high latitudes. It focuses on two remote sensing techniques, hyperspectral reflectance and Solar-Induced chlorophyll Fluorescence (SIF), which provide physiological insights into the seasonality of GPP.

In Chapter 2, we mechanistically explained the seasonal co-variation of GPP and the spectrally resolved visible-near infrared reflectance signal. We found the canopy reflectance around 531 nm is critical for inferring the seasonal variations in light use efficiency due to changes in photoprotective pigments. While indices like chlorophyll/carotenoid index and photochemical reflectance index are performing sufficiently as our methods at the canopy scale, the application of the full spectrum might be more robust for space-based measurements. Our work provides future studies and satellite missions a convenient reference using hyperspectral reflectance to achieve accurate monitoring of GPP in evergreen forests. Although our current study is limited to a subalpine evergreen forest and canopy-scale measurements, the results of this study have been referenced in studies at high latitudes and/or using other observational platforms (Maguire et al., 2021; Seyednasrollah et al., 2021; Woodgate et al., 2020; Zeng et al., 2022).

In Chapter 3, we evaluated the accuracy and uncertainty of predicting GPP using SIF across the Arctic-Boreal region. For the first time, our study reports the fitted regression slope k as well as the uncertainties of SIF-GPP relationship for the land cover types that are unique to the Arctic-Boreal region. Meanwhile, We found several potential issues specific to the Arctic-Boreal region that should be considered: 1) unrealistically high FluxCom GPP due to the presence of snow and water at the subpixel scale, 2) changing biomass distribution and SIF-GPP relationship along elevational gradients, and 3) limited perspective and misrepresentation of heterogeneous land cover across spatial resolutions. Taken together, our results will help improve the estimation of GPP using SIF in terrestrial biosphere models and cope with model-data uncertainties in the Arctic-Boreal region.

SIF_{dc} is scaled from instantaneous SIF measurements, which requires a length-of-day correction factor (DC). In Chapter 4, we highlighted two factors impacting DC and SIF_{dc}: clear-sky biases and topography. The clear-sky biases are significant for regions with large seasonal changes in cloudiness. This can even compound the interpretation of seasonal SIF dynamics. In the Amazon basin, for which SIF in periods with frequent cloudiness can be overestimated by about 25%, which is significant given the overall seasonal dynamic range in SIF is only ±20%. For complex terrains, topographic corrections on DC are required, specifically for satellites observing highly tilted surfaces within their footprints. In San Gabriel Mountains, CA, the biases in DC due to topography can be up to 500%. As more space-borne SIF measurements become available, our length-of-day correction and monthly averaging methods are useful for homogenizing and comparing SIF measurements across a variety of overpass and spatiotemporal scales.

Taken together, the results of this thesis can improve the prediction of GPP at high latitudes using remote sensing techniques. The methodology of this thesis can be expanded to the global scale, which will further help constrain the uncertainty in the global carbon budget and future climate projections.

Bibliography

A. J. Maguire, J. U. H. Eitel, T. S. Magney, C. Frankenberg, P. Köhler, E. L. Orcutt, N. C. Parazoo, R. Pavlick, and Z. A. Pierrat. Spatial covariation between solar-induced fluorescence and vegetation indices from Arctic-Boreal landscapes. *Environmental Research Letters*, 16(9):095002, August 2021. ISSN 1748-9326. doi: 10.1088/1748-9326/ac188a. URL `https://doi.org/10.1088/1748-9326/ac188a`.

B. Seyednasrollah, D. R. Bowling, R. Cheng, B. A. Logan, T. S. Magney, C. Frankenberg, J. C. Yang, A. M. Young, K. Hufkens, M. A. Arain, T. A. Black, P. D. Blanken, R. Bracho, R. Jassal, D. Y. Hollinger, B. E. Law, Z. Nesic, and A. D. Richardson. Seasonal variation in the canopy color of temperate evergreen conifer forests. *New Phytologist*, 229(5):2586–2600, March 2021. ISSN 0028-646X, 1469-8137. doi: 10.1111/nph.17046. URL `https://onlinelibrary.wiley.com/doi/10.1111/nph.17046`.

W. Woodgate, E. van Gorsel, D. Hughes, L. Suarez, J. Jimenez-Berni, and A. Held. THEMS: an automated thermal and hyperspectral proximal sensing system for canopy reflectance, radiance and temperature. *Plant Methods*, 16(1):105, July 2020. ISSN 1746-4811. doi: 10.1186/s13007-020-00646-w. URL `https://doi.org/10.1186/s13007-020-00646-w`.

Y. Zeng, D. Hao, A. Huete, B. Dechant, J. Berry, J. M. Chen, J. Joiner, C. Frankenberg, B. Bond-Lamberty, Y. Ryu, J. Xiao, G. R. Asrar, and M. Chen. Optical vegetation indices for monitoring terrestrial ecosystems globally. *Nature Reviews Earth & Environment*, 3(7):477–493, July 2022. ISSN 2662-138X. doi: 10.1038/s43017-022-00298-5. URL https://www.nature.com/articles/s43017-022-00298-5.